Calibration of the ZEUS 6 m tagger

Diplomarbeit
am Institut für Experimentalphysik
der Universität Hamburg

vorgelegt von
Matthias Schröder
27. April 2008

Gutachter der Diplomarbeit:
Prof. Robert Klanner
Prof. Caren Hagner

Abstract

In the last period of the HERA running, data were taken with the ZEUS detector to measure directly the longitudinal structure function of the proton and to determine the total photoproduction cross section. The identification of electrons from photoproduction events, in which an electron interacts with a proton and is scattered at very small angles, is essential for both the measurements. The electrons were detected using a small electromagnetic calorimeter, the 6 m tagger, which was located near the beam pipe at ≈ 6 m from the ep interaction point. A method for the calibration and the reconstruction of electromagnetic showers in the 6 m tagger was developed and the energy acceptance range and the resolution of the 6 m tagger were measured. Furthermore, the photon acceptance and the energy resolution of a different electromagnetic calorimeter used for the luminosity measurement at ZEUS were analyzed using the 6 m tagger.

Kurzfassung

Während der letzten Betriebszeit von HERA wurden Daten mit dem ZEUS Detektor genommen, um die longitudinale Strukturfunktion des Protons direkt zu messen sowie den totalen Wirkungsquerschnitt für Photoproduktion zu bestimmen. Die Identifikation von Elektronen aus Photoproduktionsereignissen, in denen ein Elektron mit einem Proton wechselwirkt und unter sehr kleinen Winkeln gestreut wird, ist wesentlich für beide Messungen. Die Elektronen wurden mit Hilfe eines kleinen, elektromagnetischen Kalorimeters, des 6 m tagger, nachgewiesen, das in etwa 6 m Entfernung vom ep Wechselwirkungspunkt nahe des Strahlrohrs installiert war. Eine Methode zur Kalibration und Rekonstruktion elektromagnetischer Schauer im 6 m tagger wurde entwickelt und der Energieakzeptanzbereich sowie die Auflösung des 6 m tagger wurden gemessen. Ferner wurden mit Hilfe des 6 m tagger die Photonakzeptanz und die Auflösung eines weiteren elektromagnetischen Kalorimeters bestimmt, welches zur Messung der Luminosität bei ZEUS verwendet wurde.

Contents

1 Introduction

The Hadron-Elektron-Ring-Anlage *HERA* was a lepton-proton collider at the Deutsche Elektronen Synchrotron *DESY* in Hamburg, operating from October 19, 1991, to June 30, 2007. The machine was operated with a nominal energy of the electrons[1] of 27.5 GeV and of the protons of 920 GeV leading to a center of mass energy of $\approx$ 318 GeV. HERA underwent a major luminosity upgrade during a shut-down which began in 2000 [1, 2]. Some relevant design parameters of the upgraded machine are listed in Table 1.1.

Particle	e / p
Nominal energy (GeV)	27.5 / 920
Center of mass energy (GeV)	318
Maximum current (mA)	58 / 140
Number of bunches (pilot)	114 (15) / 174 (6)
Rate of bunch crossings (MHz)	10.4
Horizontal bunch size (mm)	0.120 / 0.120
Vertical bunch size (mm)	0.030 / 0.030
Longitudinal bunch size (mm)	7 / 140
Specific luminosity ($\mathrm{cm^{-2}\,s^{-1}\,mA^{-2}}$)	$1.8 \cdot 10^{30}$
Peak luminosity ($\mathrm{cm^{-2}\,s^{-1}}$)	$7.5 \cdot 10^{31}$

Table 1.1: Some HERA parameters after the luminosity upgrade [1].

Four experiments were installed at the four interaction points of the HERA ring. The HERA-B experiment used fixed-target proton collisions to study CP-violation (until 2000) and the HERMES experiment used the HERA electron beam to investigate the spin structure of the nucleon. The electron-proton collisions were studied at the two experiments H1 and ZEUS. The emphasis of the physics program of these latter experiments is the investigation of the structure of the proton [3]. This is performed by analyzing the *deep inelastic scattering* (*DIS*) reactions in which the electron interacts with a proton constituent via the exchange of a boson. At HERA, the dominant contribution to the DIS cross section comes from the exchange of a virtual photon ($Q^2 \gtrsim 1\ \mathrm{GeV^2/c^2}$), $ep \to e'X$. The structure of the proton becomes

[1] In the following the notation "electron" will be used for both electrons and positrons unless stated otherwise.

manifest in the deviation of the cross section of the DIS reaction from that of a scattering of two point-like particles and is parameterized via several *structure functions*. The structure function dominant in DIS at HERA is F_2, which describes the part of the DIS cross section arising from the exchange of a transversally polarized photon. The other structure functions F_3 and F_L parameterize the part of the DIS cross section related to the exchange of a Z^0-boson and caused by the exchange of a longitudinally polarized photon, respectively. They contribute less to the DIS cross section in most parts of the available kinematic regions at HERA.

F_L is of particular interest, as it is directly correlated with the gluon density in the proton in lowest order QCD [4]. A precise knowledge of the gluon distribution is an essential part in the understanding of the proton structure. It is also of great importance for the analysis of the proton-proton collisions at the Large Hadron Collider (*LHC*) since the gluon-gluon fusion will be the dominant contribution to the cross section.

In the last months of its physics program, HERA was operated at different center of mass energies in order to allow a direct measurement of F_L [4]. The proton energy was decreased to about 460 GeV from March 26 to June 1, 2007, referred to as low energy run (*LER*) period, and to 575 GeV from June 1 to June 30, 2007, referred to as medium energy run (*MER*) period. The time span before March 26, 2007, during which HERA was run with a proton energy of 920 GeV, is referred to as high energy run (*HER*) period.

The main uncertainty on the measurement of F_L is expected to come from the estimation of the contamination by *photoproduction* events. The photoproduction regime is defined as the interaction of an almost real photon ($Q^2 \approx 0$ GeV^2/c^2) with a proton [5]. At ZEUS this background is evaluated using the *6 m tagger*, a small calorimeter which was also part of the system used to measure the luminosity [4, 6].

Furthermore, the 6 m tagger is used to determine the total photoproduction cross section, $\sigma_{texttot}$, at photon-proton center of mass energies from 200 to 300 GeV [7, 8].

This thesis describes the investigation of two different methods for an improvement of the calibration of the 6 m tagger. It is structured as follows: Chapter 2 provides an overview of calorimetry in high energy physics, namely a description of the interaction of high energetic particles with matter and basic principles of calorimeters. In Chapter 3 the system for the luminosity measurement at ZEUS is introduced and in this context the Bethe-Heitler process is briefly reviewed. The design and the technique of the energy reconstruction of the 6 m tagger are described in detail in Chapter 4; moreover the need for an improvement of the existing calibration is motivated and the chosen strategy is outlined. In Chapter 5 the selection of Bethe-Heitler events in presented. The investigated methods for an improvement of the calibration of the 6 m tagger are explained in Chapter 6. Finally, studies using the newly calibrated 6 m tagger are presented in Chapter 7, among others the development of criteria for the evaluation of the quality of the events reconstructed in the 6 m tagger, and an analysis of the acceptance of the photon spectrometer.

2 Calorimetry in high energy physics

Calorimeters are detectors used primarily to measure the energy but also the position of a particle or a particle jet. They are essentially blocks of matter in which an incoming particle, owing to its interaction with the material, deposits energy that is then transformed into a measurable signal. Their design is usually such that a particle releases all its energy in them in order to allow a reliable energy measurement.

In calorimeters used in high energy physics, the incoming particle generates a cascade of particles with successively decreasing energy. The charged particles of the cascade produce light or free charges in the detector material which are used to measure the energy of the incident particle. Calorimeters can generally be divided into electromagnetic and hadronic calorimeters. The first are used to measure the energy of electrons and photons and the latter to measure hadrons.

There are two basic designs, sampling and homogeneous calorimeters. Sampling calorimeters consist of separated layers of a passive high density absorber material (e.g. lead, tungsten, or uranium) and an active material generating the signal (e.g. a scintillator, an ionizing gas, or a semiconductor). Homogeneous calorimeters in contrast are made of one material both absorbing the particles and generating the signal (e.g. lead glass or BGO) [9].

In the following, electromagnetic cascades and scintillators are discussed; then some general properties of calorimeters are presented. The focus is on electromagnetic scintillation sampling calorimeters as the 6 m tagger is such a detector.

2.1 Electromagnetic cascades

The different processes contributing to the energy loss of electrons and photons in matter are shown in Fig. 2.1 (here exemplarily for lead). At energies larger than ≈ 10 MeV, electrons lose energy predominantly by radiating a photon (Bethe-Heitler process) and photons by e^+e^- pair production. Below that energy, the main effects are ionization and excitation for electrons as well as Compton scattering and photoelectric effect for photons.

A high-energy electron or photon in matter induces an electromagnetic cascade (*shower*) by consecutively generating new particles with lower energies via Bethe-Heitler-processes (*bremsstrahlung*) and pair production. The shower development terminates when the energy of the electrons eventually falls below a *critical energy*, E_c, and they start to release energy mainly by ionization and excitation.

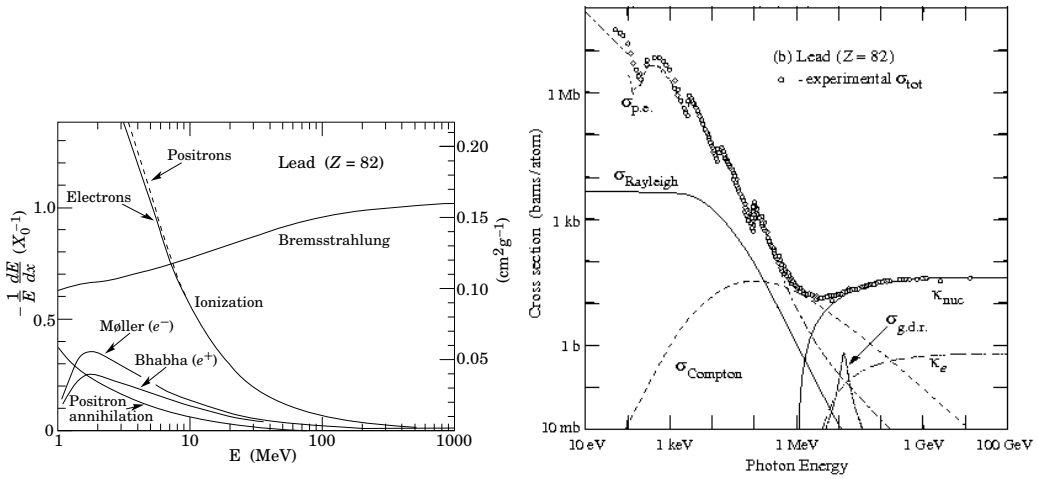

(a) (b)

Figure 2.1: Different processes contributing to the energy loss of electrons and photons in matter. (a) Fractional energy loss per radiation length of electrons in lead. (b) Total cross section for the different processes of photons in lead [9].

The properties of an electromagnetic shower depend on the energy E_0 of the initial particle and on the material the particle traverses. The material dependencies are described by the critical energy E_c, the *radiation length*, X_0, and the *Molière radius*, R_M [10].

The critical energy can be approximated by

$$E_c = \frac{800 \text{ MeV}}{Z + 1.2},$$

where Z is the atomic number of the material.

X_0 is the mean distance in material over which the energy of a high-energy electron falls to $1/e$ of its original value. Likewise X_0 is $\frac{7}{9}$ of the mean free path of a high-energy photon. X_0 can be approximated as

$$X_0 = \frac{716.4 A \,\mathrm{g\,cm^{-2}}}{Z(Z+1)\ln(287/\sqrt{Z})},$$

with A being the atomic mass. The radiation length is also an appropriate scale variable for the average longitudinal profile of the energy deposition in an electromagnetic shower. The profile can be described by

$$\frac{dE}{dt} = E_0 b \frac{(bt)^{a-1} e^{-bt}}{\Gamma(a)} \tag{2.1}$$

where the distance t is expressed in units of radiation length, $t = \frac{x}{X_0}$. The maximum occurs at

$$t_{\max} = \frac{a-1}{b} = \ln\left(\frac{E_0}{E_c}\right) + c$$

where the parameter c is -0.5 for electrons and $+0.5$ for photons. The parameter b was empirically found to be ≈ 0.5. Therefore, the length of the shower scales logarithmically with the energy of the incident particle. Figure 2.2 shows the corresponding profile for a shower development in tungsten, the absorber material the 6 m tagger was made of.

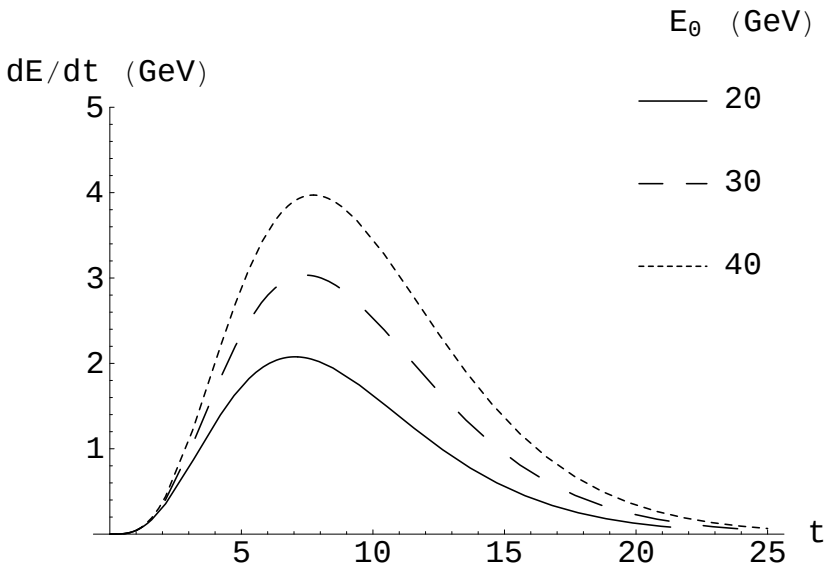

Figure 2.2: Simulation of the mean longitudinal profile of an electron-induced shower in tungsten, according to Eq. (2.1). The plot shows the differential energy deposition as a function of the distance in radiation lengths for different initial electron energies E_0.

The transverse dimensions of electromagnetic showers are in general smaller than their longitudinal size. The transverse size is approximately logarithmically dependent on E_0. It scales with the Molière radius

$$R_M = X_0 \frac{21 \text{ MeV}}{E_c},$$

and about 90% of the energy is contained in a cylinder of radius $1R_M$ [9].

2.2 Scintillating fibers

Charged particles traversing matter excite the surrounding molecules. In scintillating materials these molecules release parts ($\approx 3\%$) of their excitation energy as photons.

Scintillating fibers (*SCIFI*) are made of a base of scintillating material. Typical light yields are about 1 photon per 100 eV of deposited energy. The base is often doped with fluorescent molecules which shorten the decay time of the scintillating process as well as absorb the emitted photons and re-emit them at longer wavelengths where the base is more transparent. They are therefore called *wavelength shifter*. The scintillating and wavelength shifting base is surrounded by a skin with a smaller index of refraction to guide the photons along the fiber by total internal reflection.

Scintillating fibers are thus used both to generate a signal of photons and guide them out of the detector to photomultipliers where they can be converted into an electric signal.

A characteristic quantity of the fiber is the *attenuation length*, i.e. the length after which the signal is reduced to $1/e$ of its original value. The attenuation length depends on the wavelength of the light, the nature and concentration of the fluor but also on external parameters such as irradiation. Radiation damages create *color centers* which absorb photons and reduce the attenuation length. [9]

2.3 Energy resolution of electromagnetic calorimeters

The principle of the energy measurement with an electromagnetic calorimeter is the assumption that the energy released in the active part of the detector – for example the energy of the photons emitted by a scintillating fiber – is proportional to the original energy of the incident particle. The energy resolution, $\frac{\sigma_E}{E}$, is usually parameterized as

$$\frac{\sigma_E}{E} = \frac{a}{\sqrt{E}} \oplus b \oplus \frac{c}{E},$$

where $\oplus$ indicates the sum in quadrature and E is given in GeV [9]. It consists of a *stochastic term*, a *constant term*, and a *noise term*.

The stochastic term represents statistical fluctuations in the shower development such as the track length of the individual particles in the cascade as well as photoelectron statistics for optical readout with photomultipliers. In sampling calorimeters a is approximately proportional to $\sqrt{t/f}$ where t is the thickness of the absorber layers in radiation lengths and f the sampling fraction defined as [10]

$$f = \frac{E_{\text{act}}}{E_{\text{act}} + E_{\text{abs}}}.$$

Here, E_{act} and E_{abs} are the energies deposited in the active and absorber part of the

calorimeter, respectively. a is typically at the order of 10% in sampling calorimeters and gives the dominant contribution to the energy resolution.

The constant term b is dominated by effects of detector non-uniformities and calibration uncertainties as well as radiation damages to the active medium. In well calibrated calorimeters the term is at or below the percent level [9].

The noise term is due to the electronic noise of the readout chain; it can be reduced by increasing the sampling fraction [10].

3 The luminosity measurement system of the ZEUS experiment

The ZEUS experiment was a multipurpose detector designed to measure the products of the electron-proton collisions at HERA. It surrounded the interaction region with different detector systems to determine relevant quantities of the reactions, like for instance the exact position of the vertex or the energy and momentum of the produced particles. The central ZEUS detector had a size of $10 \times 10 \times 12\,\mathrm{m}^3$ and a mass of about 3600 t [11].

The rate, R, of a process of a certain type at a collider is proportional to the cross section σ of that process,

$$R = \mathcal{L}\sigma.$$

The constant of proportionality is the *luminosity*, $\mathcal{L}$, which summarizes the parameters of the experimental setup. It is given by

$$\mathcal{L} = f\frac{n_1 n_2}{4\pi\sigma_x\sigma_y},$$

where n_1 and n_2 denote the number of particles in the two colliding bunches, f the frequency of their collisions, and σ_x and σ_y the width of their Gaussian transverse profile, assuming equal bunches in each collision [9].

The luminosity is a key quantity to measure cross sections in collider experiments. The ZEUS experiment employed the precisely calculable Bethe-Heitler process, $ep \to ep\gamma$, to determine the luminosity. A system of detectors ($LUMI$) was set up to measure the rate of Bethe-Heitler events and hence allowing the calculation of $\mathcal{L}$ [6].

In the following, the luminosity measurement is discussed in more detail. First, the Bethe-Heitler process is briefly reviewed, then the LUMI system is described.

3.1 The Bethe-Heitler cross section

Charged particles moving in external electric fields can emit real photons. The conservation of energy and momentum is ensured by the additional interaction with the external field (Bethe-Heitler process) [12, 13]. Electrons can therefore radiate photons in the bunch crossings at ZEUS due to the electric field of the colliding protons, as illustrated in Fig. 3.1.

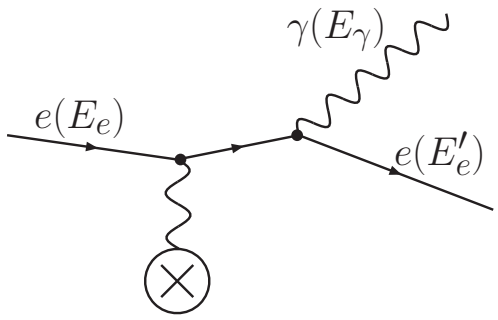

Figure 3.1: Feynman diagram of a lowest-order QED Bethe-Heitler process at HERA.

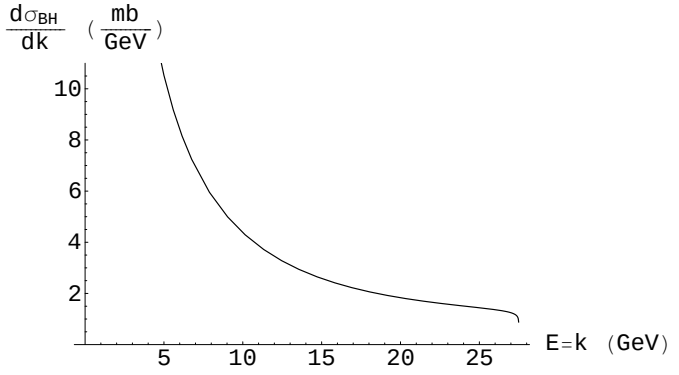

Figure 3.2: The Bethe-Heitler cross section differentially in the photon energy k calculated from Eq. 3.1 with the values given in Tab. 3.1.

The cross section of the Bethe-Heitler process, $ep \to ep\gamma$, differentially in the photon energy k, is given for highly energetic electrons (energies much larger than m_e) by [14]

$$\frac{\mathrm{d}\sigma_{\mathrm{BH}}}{\mathrm{d}k} = 4\alpha r^2 \frac{E_f}{kE_i}\left(\frac{E_i}{E_f} + \frac{E_f}{E_i} - \frac{2}{3}\right)\left(\ln\frac{4E_pE_iE_f}{m_pm_ek} - \frac{1}{2}\right), \tag{3.1}$$

where the variables are defined in Table 3.1. Figure 3.2 shows the corresponding cross section. To estimate the rate of Bethe-Heitler processes, Eq. (3.1) is integrated over a reasonable interval of photon energies, e.g. from $k = 0.1$ to 27.5 GeV, and multiplied by the nominal luminosity. The resulting rate is of the order of 20 MHz (comp. Table A.2 in Appendix A) i.e. more than one event is expected per bunch crossing.

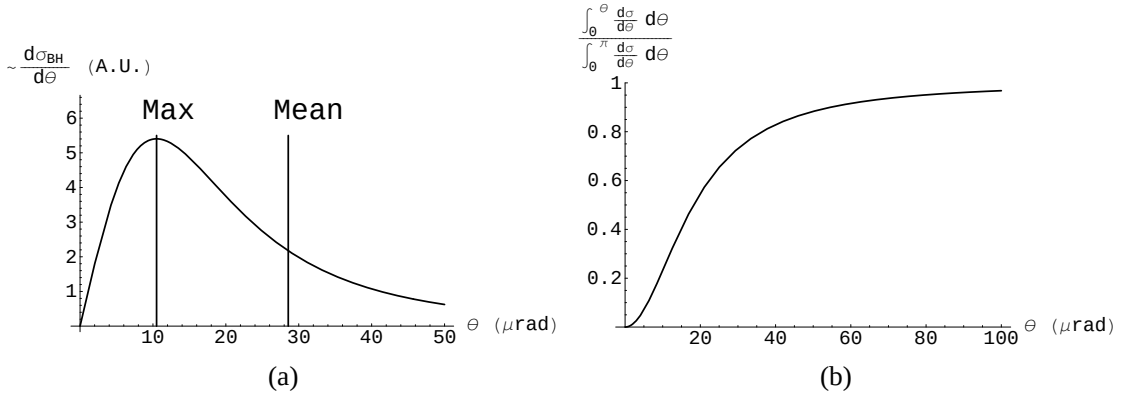

Figure 3.3: (a) The Bethe-Heitler cross section from Eq. 3.2 differentially in the angle θ of the photon calculated with the values given in Tab. 3.1. The vertical lines indicate the maximum and the mean value $\int_0^\pi \theta \frac{\mathrm{d}\sigma_{\mathrm{BH}}}{\mathrm{d}\theta}\mathrm{d}\theta / \int_0^\pi \frac{\mathrm{d}\sigma_{\mathrm{BH}}}{\mathrm{d}\theta}\mathrm{d}\theta$. (b) The integrated angular distribution as a function of θ, i.e. the fraction of the number of photons radiated with an angle lower than θ.

Symbol	Definition	Value
α	Fine structure constant	$7.297352568(24) \cdot 10^{-3}$
r	Classical electron radius	$2.817940325(28) \cdot 10^{-15}\,\mathrm{m}$
m_p	Proton mass	$938.272029(80)\ \mathrm{MeV}/c^2$
m_e	Electron mass	$0.510998918(44)\ \mathrm{MeV}/c^2$
E_p	Proton energy	920 GeV
E_i	Initial electron energy	27.5 GeV
E_f	Final electron energy	$E_i - k$
k	Photon energy	—
θ	Angle between the direction of the photon and the initial electron	—

Table 3.1: Summary of the variables used for the calculation of the Bethe-Heitler cross section. Values are taken from [9].

The angular distribution of the emitted photon [14],

$$\frac{\mathrm{d}\sigma_{\mathrm{BH}}}{\mathrm{d}\theta} \propto \frac{\theta}{\left(\left(\frac{m_e}{E_i}\right)^2 + \theta^2\right)^2}, \tag{3.2}$$

is shown in Fig. 3.3 (a). It features a maximum at about $10\,\mu$rad and a mean value $\int_0^\pi \theta \frac{\mathrm{d}\sigma_{\mathrm{BH}}}{\mathrm{d}\theta}\mathrm{d}\theta / \int_0^\pi \frac{\mathrm{d}\sigma_{\mathrm{BH}}}{\mathrm{d}\theta}\mathrm{d}\theta$ of $\approx 30\,\mu$rad. Figure. 3.3 (b) shows the integrated angular distribution as a function of the angle θ of the photon. The majority of the photons

are emitted at very small angles: more than 90% at angles lower than 60 μrad. The same angular distribution holds approximately for the emitted electrons if they are highly energetic.

3.2 The luminosity measurement system LUMI

The LUMI system [6] used after the HERA upgrade consisted of three components, the photon calorimeter, the photon spectrometer, and the 6 m tagger (electron calorimeter), as sketched in Fig. 3.4. The latter was used primarily for calibration and acceptance measurements of the other two components.

Here only the photon calorimeter and the photon spectrometer are discussed; the 6 m tagger is presented in detail in Chapter 4.

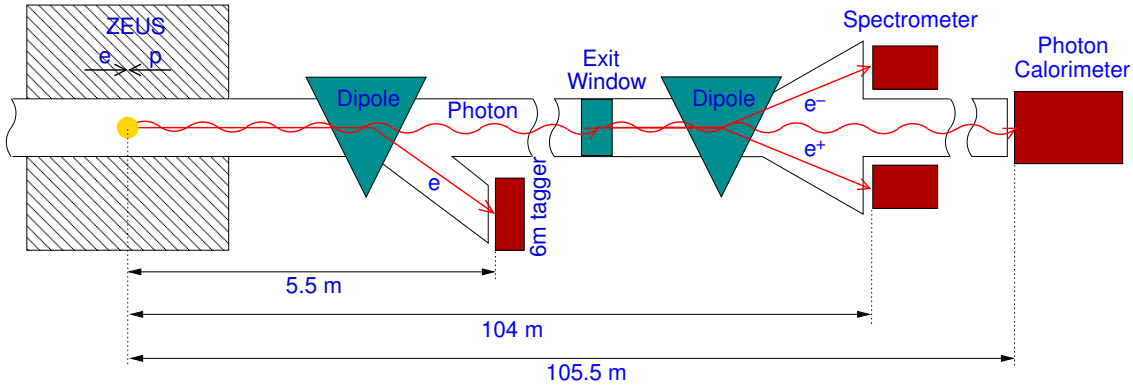

Figure 3.4: Schematic view of the ZEUS luminosity system.

The photon and the electron from a Bethe-Heitler process inside the ZEUS detector were generally radiated at very small angles w.r.t. the direction of the incoming electron (comp. Section 3.1). Therefore both the electron and the photon left the detector through the beampipe in the direction of the electron beam (comp. Fig. 3.4).

The photon, unaffected by magnetic fields, traveled straight down the beampipe and left it through an exit window located 92 m behind the nominal interaction point. Its energy and position was measured by the photon calorimeter which was installed 105.5 m from the interaction point. The photon calorimeter was a lead-scintillator sampling calorimeter with a depth of 24 X_0, read out by two photomultipliers. It was shielded against synchrotron radiation by an active filter system consisting of two carbon absorber in series, each with a depth of 2 X_0. Behind each absorber an aerogel counter was installed which was read out by one photomultiplier. These counters enabled an estimation of the amount of energy absorbed in front of the calorimeter and therefore a correction of the energy measurement. This lead to an energy resolution of $25\%/\sqrt{E\,(\mathrm{GeV})}$ [6].

In order to determine the luminosity, effects like Bethe-Heitler radiation from the interaction of the electrons with residual gas in the beam pipe had to be taken into account. Moreover, as more than one Bethe-Heitler process per bunch crossing was expected (comp. Section 3.1), *pile-up* events in which more than one photon hit the calorimeter had to be considered [6].

The exit window was composed of an alloy made mainly of aluminum and silicon with a thickness of about 1 cm, corresponding to $0.12X_0$. Hence, about 8.9% of the traversing photons having energies larger than ≈ 1 MeV converted into an electron-positron pair. These leptons were deflected upward and downward, respectively, by a dipole magnet and detected by the two modules of the photon spectrometer, installed 104 m behind the interaction point. Both modules were tungsten-scintillator sampling calorimeters with a depth of $24X_0$ and an energy resolution of $17\%/\sqrt{E\,(\mathrm{GeV})}$. They were placed above and below the beampipe thus avoiding exposure to synchrotron radiation. Contributions from pile-up events to the luminosity measurements were reduced due to the conversion factor in the exit window [15]. In turn, this factor had to be known accurately; a measurement was for example possible using the 6 m tagger which could tag the Bethe-Heitler electrons in a certain energy range (see Section 6.2.3).

4 The 6 m tagger

The 6 m tagger [6, 16, 17, 18] was a small tungsten-scintillator spaghetti calorimeter that was installed at about 6 m from the nominal interaction point of ZEUS in the direction of the electron beam. It was located next to the beampipe inside the HERA ring behind the dipole magnet of the GG system [2], as illustrated in Fig. 4.1. The bending power of the dipole was such that electrons with energies between ≈ 4 and ≈ 7 GeV[1], originating for instance in a Bethe-Heitler or photoproduction process, were deflected out of the nominal beam orbit and hit the 6 m tagger.

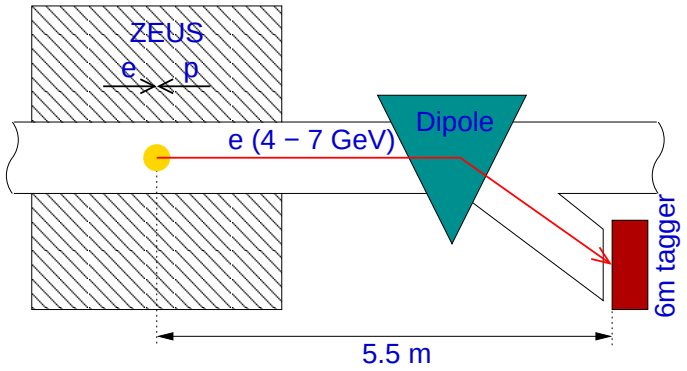

Figure 4.1: Schematic view of the position of the 6 m tagger. Electrons with energies between about 4 and 7 GeV were deflected by the dipole such that they hit the 6 m tagger.

As mentioned before, the 6 m tagger was originally designed as part of the LUMI system for acceptance studies and cross calibration. It is also used for the determination of the total photoproduction cross section and for the determination of the background of the measurement of the longitudinal structure function F_L.

4.1 Geometry and design

The 6 m tagger was located inside the HERA quadrupole magnet GI06SR5 [2]. Its front surface was situated at $z = -5512.0$ mm [19] in the ZEUS coordinate system[2].

[1] The energy acceptance range of the 6 m tagger is evaluated in Section 6.2.3.

[2] The ZEUS coordinate system was a right-handed Cartesian system with the origin at the nominal interaction point. The z axis was pointing in the proton beam direction and the x axis pointing

The left side touched the beam pipe and therefore had a distance of 64.5 mm or 68.8 mm from the nominal electron or positron beam, respectively [20], as shown in Fig. 4.2.

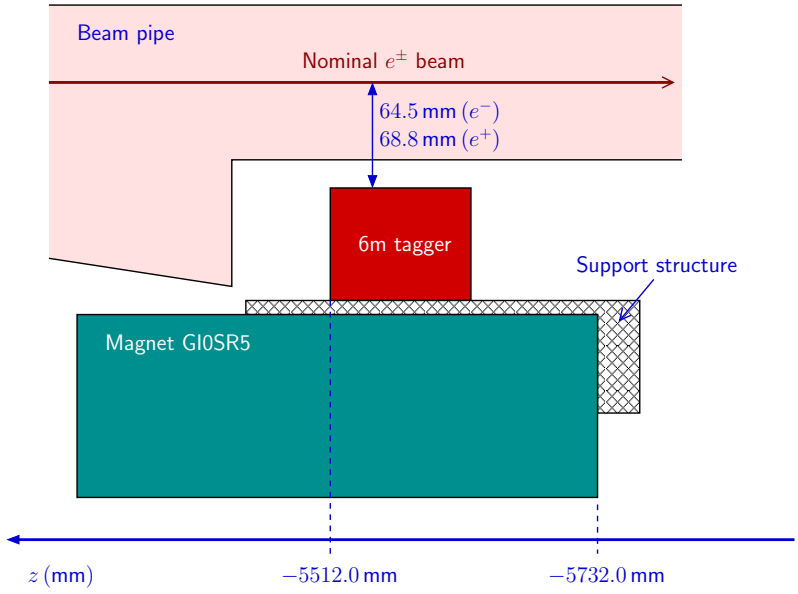

Figure 4.2: Position of the 6 m tagger inside the quadrupole magnet GI06SR5 in the ZEUS reference system.

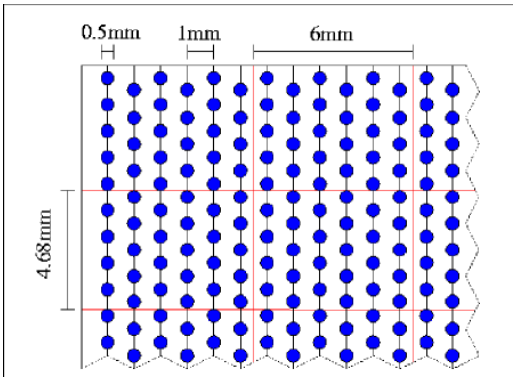

Figure 4.3: Geometry of the tungsten plates and fibers. The size of the cells containing one group of 27 fibers are indicated [17].

The 6 m tagger had a size of $84 \times 23.4 \times 100\,\text{mm}^3$ [17]. It had a radiation length of 3.561 mm and a Molière radius of 7.089 mm [21]. The limited dimension of the

toward the center of the HERA ring [11].

device were dictated by the spatial constraints given by the magnet inside which it was installed.

The detector was built out of 84 tungsten plates with a size of $1 \times 23.4 \times 100\,\mathrm{mm}^3$. Semi-circular grooves were milled in the plates which provide space for scintillator fibers. The fibers were made of SCSF-38M scintillator material and had a length of 1.5 m and a diameter of 0.5 mm. In total the 6 m tagger contained 1890 fibers, grouped into 70 channels of 27 fibers each. Each channel was readout by a photomultiplier. The calorimeter was thereby divided into $14 \times 5 = 70$ cells, each having a size of $6 \times 4.68\,\mathrm{mm}^2$ [18]. The geometry of the whole detector as well as the grouping of the fibers are shown in detail in Figs. 4.3 and 4.4 .

4.2 Coordinate system

Figure 4.4 illustrates the coordinate system of the 6 m tagger as used in this report. The origin is located at the left edge of the detector. The x axis points from the beampipe to the right toward the center of the HERA ring, the y axis from the bottom to the top, and the z axis points in the direction of the proton beam, thus forming a right-handed coordinate system.

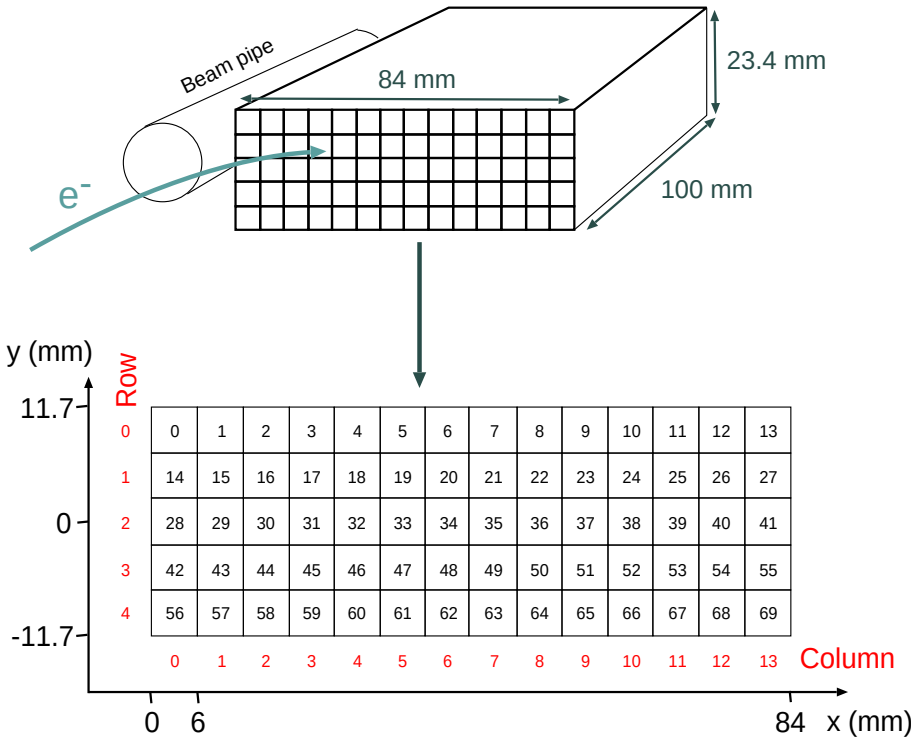

Figure 4.4: The coordinate system of the 6 m tagger.

There are two ways to label a cell. First, cells are numbered from 0 to 69, starting in the upper left corner and then counting from left to right. Second, columns are numbered from 0 to 13 in the x direction and rows are numbered from 0 to 4 in the negative y direction.

4.3 Energy reconstruction

An electron hitting the 6 m tagger produced an electromagnetic shower and released most of its energy in a cylinder with radius of a few R_M (see Chapter 2). As the Molière radius was of the order of the size of a cell, most of the energy was consequently deposited in a few cells around the shower center. An example is shown in Fig. 4.5.

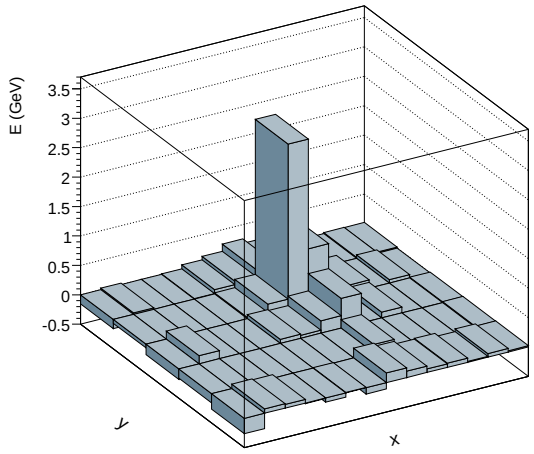

Figure 4.5: Example of an electromagnetic shower in the 6 m tagger (event 5061 in run 70204). The reconstructed energy deposition in each cell is plotted. The reconstructed energy of the shower was $E = 5.2$ GeV. Note that the dimensions of the cells are not to scale.

The signal in one cell k measured by the photomultipliers was converted to counts, $\mathcal{A}_k$, by an *analogue-to-digital-converter* (ADC). These were then further converted into an energy, E_k, by subtracting a pedestal, $\mathcal{P}_k$, and multiplying by a calibration factor:

$$E_k = (\mathcal{A}_k - \mathcal{P}_k)\, c^{\text{base}} c_k^{\text{orig}}.$$

The pedestal $\mathcal{P}_k$ was the mean signal of the electronic noise in that cell given in ADC counts. The constant $c^{\text{base}} = 0.0157875$ GeV did the basic conversion from ADC counts to GeV; it was the same for all cells. Changes in this conversion factor

due to damages of the fibers etc. were compensated by the calibration constants c_k^{orig}. The calibration constants as well as the pedestals were derived for each run as described in Section 4.5.

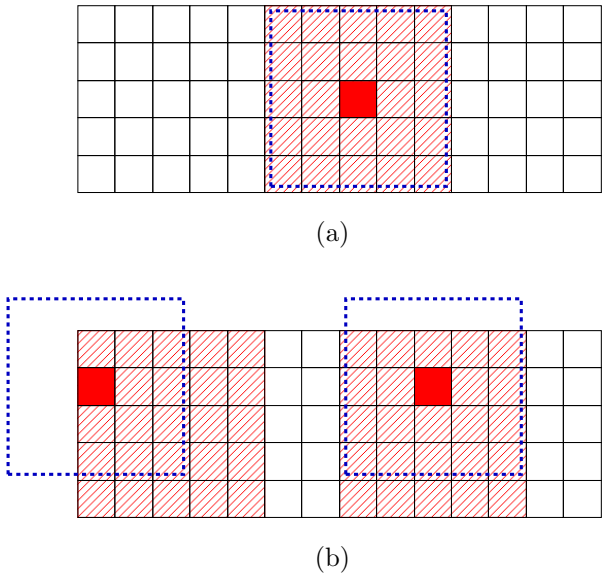

Figure 4.6: Standard volume for energy reconstruction (hashed area) around the hottest cell (filled cell). (a) If the hottest cell was in the central detector region, the volume lay symmetrically around it. (b) Otherwise, if the reconstruction volume overlapped the 6 m tagger edges (dashed line) it was shifted inside the 6 m tagger (hashed area) to compensate for the missing parts.

For the reconstruction of the energy, the cell with the highest energy deposition, the *hottest cell*, was taken to be the one containing the shower center. The total energy deposited in a *reconstruction volume*, V, around the hottest cell was assumed to be the energy E of the shower:

$$E = \sum_{k \in V} E_k.$$

The default reconstruction volume consisted of 5×5 cells. If the hottest cell was so close to the detector border that the reconstruction volume would partially lie outside the 6 m tagger, the volume was shifted to fit completely into the detector [16]. This is illustrated in Fig. 4.6.

In the following, an event in the 6 m tagger is said to belong to one column or one row, if the hottest cell is found in that column or row, respectively.

4.4 Description of the electron energy spectrum

Electrons radiating a photon in a Bethe-Heitler process at the ZEUS interaction point were predominantly deflected at very small angles – of the order of a few tens of μrad – from their original direction, as discussed in Section 3.1. The actual deflection also depended on the divergence of the electron beam at the vertex, however. The angle relative to the mean angle of the electron beam could be estimated from the spread of the beam spot measured with the photon calorimeter. It was ≈ 1 cm and ≈ 3 cm in the vertical and in the horizontal direction, respectively [22]. Considering that the distance of the calorimeter from the nominal interaction point was 105.5 m, this means that the vast majority of Bethe-Heitler electrons left the interaction point at angles of the order of 100 μrad w.r.t. the nominal beam direction (comp. Fig. 4.7(a)). They were then deflected horizontally by the GG dipole, as illustrated in Figs. 4.1 and 4.7(b). For high-energy electrons the radius R of curvature in a magnetic field is given by

$$R \approx \frac{E}{0.3B} \frac{\mathrm{T\,m}}{\mathrm{GeV}},$$

where E is the electron energy and B the component of the magnetic flux density orthogonal to the direction of the electron. Therefore, the deflection of the electron in the GG dipole field was the bigger the smaller the energy of the electron. As a consequence, the x position of incidence of an electron on the 6 m tagger was correlated with its energy, as shown in Fig. 4.8 (a). The electron hit the 6 m tagger at an angle of about 3 to 7 ° w.r.t. the normal in the xz plane [17], as shown schematically in Fig. 4.9.

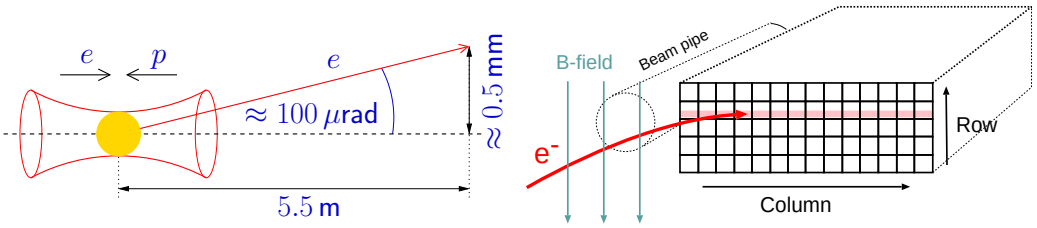

(a) (b)

Figure 4.7: (a) Displacement of the Bethe-Heitler electron from the nominal beam position at the distance of the 6 m tagger owing to the initial angle of emittance. (b) Position of incidence of the electron at the 6 m tagger surface (shaded band); the y position was almost constant while the x position depended on the energy of the electron due to the deflection in the magnetic dipole field.

The vertically deflecting components of the fields of the magnets installed between the nominal vertex and the 6 m tagger had a much smaller effect than the

horizontally bending components [23]. Therefore, the y position of incidence of the electrons at the 6 m tagger surface was mainly depending on the aforementioned original angle of deflection at the vertex and on the distance of about 5.5 m from the vertex to the 6 m tagger (comp. Fig. 4.7(a)). Hence, the variation of the y position was of the order of 500 μm and therefore, compared with the cell width of a few mm, constant for all electrons.

The position of incidence of the electrons on the 6 m tagger consequently laid on a narrow band parallel to the x axis, which was located at $y \approx 2.5$ mm, i.e. in row 1 of the 6 m tagger close to row 2. This is illustrated in Fig. 4.7(b).

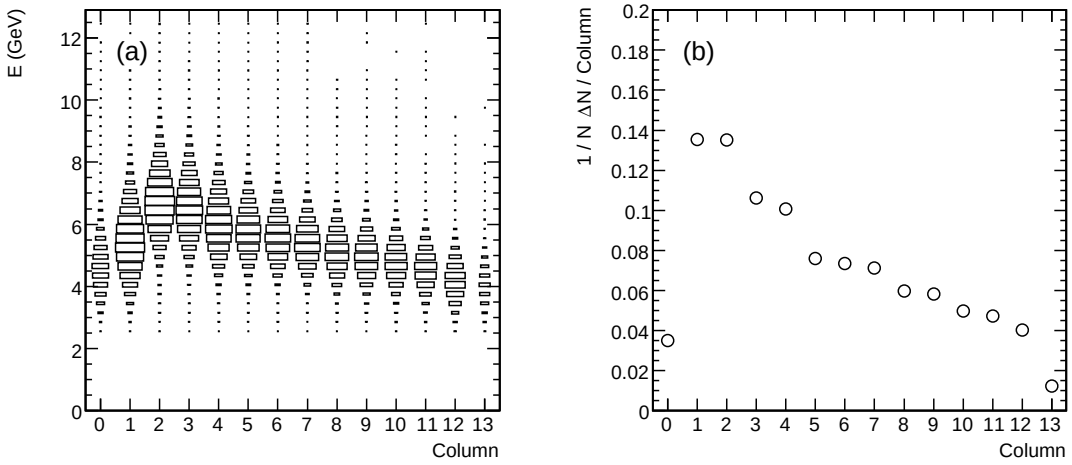

Figure 4.8: Correlation between the x position and (a) the reconstructed energy and (b) the number of electrons in the 6 m tagger in the LER period. The x position is given in bins of the column containing the hottest cell. The drop in the two outer columns was caused by the reconstruction method which did not allow a correct energy reconstruction at the borders of the 6 m tagger.

The Bethe-Heitler cross section is largest for events in which photons with small energies are radiated and decreases with increasing photon energy (see Fig. 3.2). Therefore more electrons were expected having higher than lower energies. Owing to the correlation between the x position and the energy more electrons were expected to hit the 6 m tagger at small x than at large x. This relation is shown in Fig. 4.8 (b).

The electrons hit the 6 m tagger in a band parallel to the x axis if the detector was aligned parallel to the HERA plane. Otherwise the band was tilted and the distribution of the energy and the distribution of the number of events per column had to be convoluted with the y dependence of x.

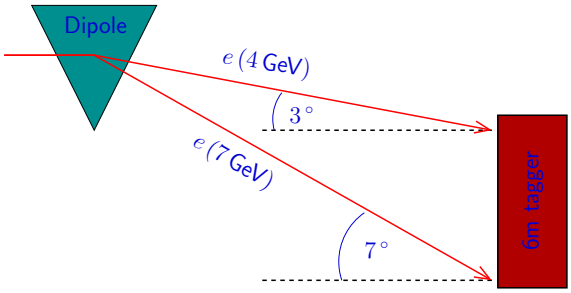

Figure 4.9: Depending on their energies, electrons were deflected and hit the 6 m tagger with different angles.

4.5 Original calibration

The 6 m tagger was calibrated using Bethe-Heitler events in which the photon was detected in the photon spectrometer and the electron in the 6 m tagger. The photon calorimeter was not used for reference as its energy resolution was worse than that of the spectrometer (comp. Section 3.2). The basic assumption was that the sum of the electron energy deposited in the 6 m tagger and the photon energy measured in the photon spectrometer (via e^+e^- conversion) was equal to the original electron beam energy of about 27.5 GeV[3]. This assumption was used to extract a set of 14 calibration constants, one for each column of the 6 m tagger. The details of this method are described elsewhere [16].

A set of calibration constants was determined for each run with more than 15000 *Third-Level-Trigger* (TLT) events [24, 25]. These constants were multiplied with different constants coming from previous test beam measurements and which took care of the relative calibration of the single cells within a column. The result was a set of 70 different calibration constants, c_k^{orig}, one for each cell k [21]. Figure 4.10 shows as an example the calibration constants for runs of the LER period (corresponding to ≈ 2 months) in two different cells. The mean value of the calibration constants was slightly increasing with the run number compensating for the decreasing response of the 6 m tagger due to radiation damage. The constants varied generally with a spread of about 5% around that mean owing to statistical fluctuations. The calibration constants obtained with this procedure will be referred to as "original", since a distinction will be necessary in the following.

The relative calibration of the cells within a column was not changed during the calibration procedure; it was still the same as that derived from the test beam measurement. One of the objectives of this study is therefore to improve the relative calibration.

[3]The nominal electron beam energy had slightly different values in the different HERA run periods; they are listed in Table B.5 in Appendix B.

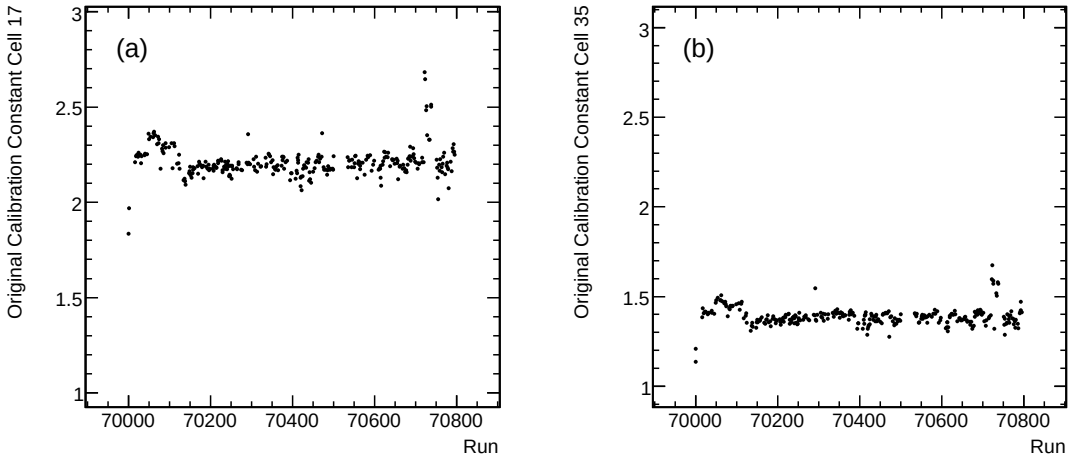

Figure 4.10: Example of the original calibration constants.

Like for the calibration constants, pedestal values were computed per run. Some electron bunches in HERA were not matched with a proton bunch and therefore did not collide when traversing the ZEUS detector (*empty bunch crossings*). Consequently no electron was expected to hit the 6 m tagger and any measured signal was therefore assumed to be due to electronic noise of the readout electronics. The pedestals were hence evaluated as the mean value of the ADC counts recorded during empty bunch crossings.

4.6 Motivation for an improvement of the calibration

In the following, the energy reconstruction and the original calibration of the 6 m tagger are analyzed in detail. Some ideas are illustrated to improve the reconstruction algorithm and evidence is given suggesting the potential to significantly improve the calibration, in particular in the outer columns.

4.6.1 Reduction of the reconstruction volume

The first method developed to reconstruct the energy in the 6 m tagger consisted in defining a volume of 5×5 cells symmetrically around the hottest cell (comp. Fig. 4.6) and in summing up the energies in these 25 cells, as described in Section 4.3. However, as can be seen from the shower profile in Fig. 4.11, only about 1 to 5% of the total energy is deposited in the outer columns of this volume (50 to 200 MeV). This signal is comparable to the noise level: the width (standard deviation of a

Gaussian fit) of the pedestal peak in one cell is about 3 ADC counts (see Table B.1 in Appendix B) and one ADC count corresponds to ≈ 15 MeV (see Section 4.5). Therefore, the fluctuations due to noise in one cell is approximately of 50 MeV and in one column in Fig. 4.11, i.e. in five cells, of about 100 MeV.

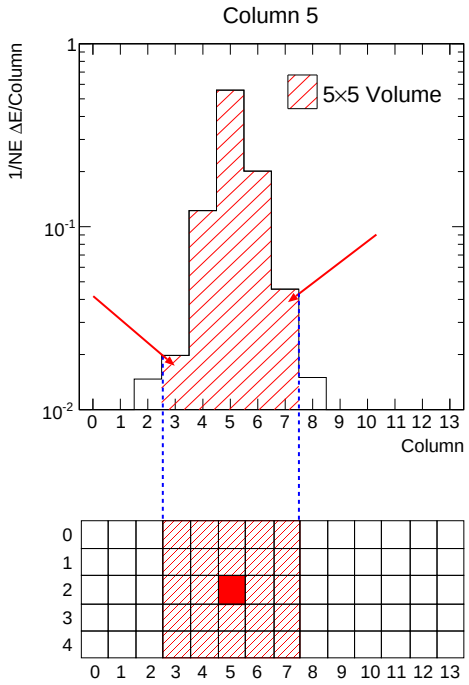

Figure 4.11: A typical transverse shower profile, normalized to the total energy of the shower. The hashed columns are included in the standard 5×5 reconstruction volume. The relative amount of energy deposited in the outer columns (arrows) of the reconstruction volume is about 5%.

If the reconstruction volume exceeds the edges of the 6 m tagger and is therefore shifted into the 6 m tagger (comp. Fig. 4.6(b)), less than 1% of the total energy is expected to be deposited in the added parts of the reconstruction volume. In this case the signal to noise ratio becomes even worse. This was, in fact, the standard case for Bethe-Heitler events; in the LER and MER periods approximately 95% of the events had the shower maximum in row 1, in the HER period still about 70%. The situation is yet worse for events with the maximum at the left or right edge of the 6 m tagger (in column 0 or 1 and 12 or 13, respectively).

In order to reduce the effects mentioned above, the calibration was to be tuned such that the reconstruction volume consisted only of nine cells, a 3×3 volume with the hottest cell in the center, as illustrated in Fig. 4.12. In this way the influence of the noise on the signal would be weakened. At the edges of the 6 m tagger only that

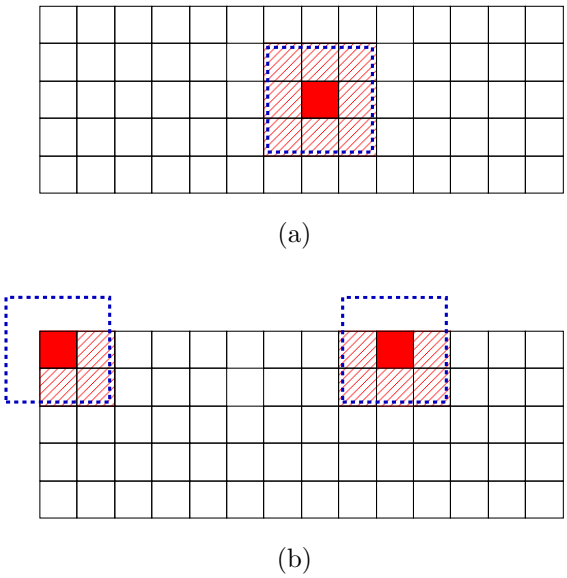

Figure 4.12: The new 3×3 volume for energy reconstruction (hashed area) around the hottest cell (filled cell). (a) If the hottest cell was in the central detector region, the volume laid symmetrically around it. (b) Otherwise, if the reconstruction volume exceeded the edges of the 6 m tagger (dashed line) it was reduced to the cells contained in the detector.

part of the volume being contained in the detector was considered for the energy reconstruction.

4.6.2 Relative calibration within one column

The original calibration of the 6 m tagger was done column wise, as described in Section 4.5. The relative calibration of the five cells within one column was taken from test beam data and could not be adjusted using the original calibration method.

A way to check the relative calibration inside one column is to investigate the column dependence of the ratio of the energies measured in different cells of the same column, as illustrated in Fig. 4.13. The positions of incidence of the electrons in Bethe-Heitler events were located within a narrow (≈ 0.5 mm) band orthogonal to the dipole field of the GG magnet owing to the angular distribution of the Bethe-Heitler process. The band was well located in row 1, close to the edge of row 2, as discussed in Section 4.4. When neglecting the incident angle of the electron, the energy deposition in the cells of one column of the 6 m tagger was dictated by the transverse profile of the electromagnetic shower. It was therefore dependent on the radial distance from the shower maximum and on the energy of the initial

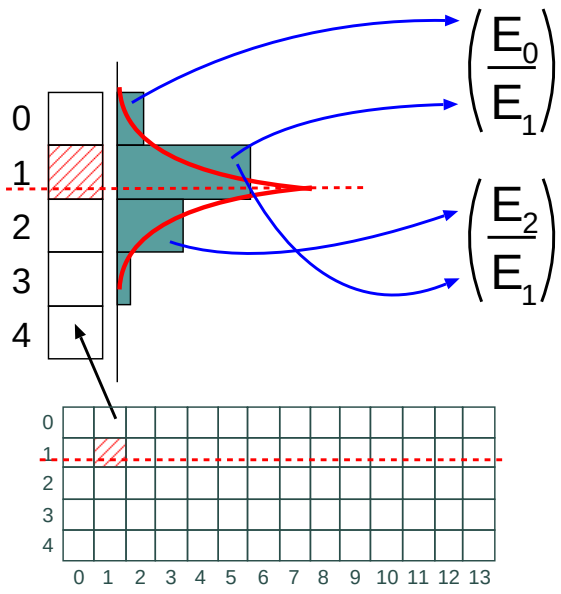

Figure 4.13: The transverse shower profile is approximately constant for electrons hitting the 6 m tagger in the same column i.e. which have approximately the same energy. As a consequence, the ratio of energies in two different cells of one column is expected to be constant for different events.

electron (Section 2.1). Thus, the ratio of deposited energy in two different cells of the same column was expected to be approximately constant for different events (comp. Fig. 4.13). If the shower profile is smoothly dependent on the energy, this ratio should have a smooth dependence on the energy of the initial electron and therefore on the column (owing to the correlation between the energy and the x position). Figure 4.14 shows the quantity

$$\frac{\bar{E}_r^n}{\bar{E}_1^n},$$

where n is the column index $(0-13)$ and $r \in \{0,2,3\}$ the row index. This is the ratio of the mean energies in row r and row 1 as function of n. It shows no smooth dependence on n. This suggested the presence of a miscalibration of the individual cells within one column.

Another indication of a relative miscalibration of the cells within one column arose from looking at the number of events per column within one row (Fig. 4.15). A smoothly decreasing distribution $\mathrm{d}N/\mathrm{d}x$ is expected from the energy dependence of the Bethe-Heitler cross section, as discussed in Section 4.4. This is true even if the 6 m tagger was not aligned horizontally i.e. $\mathrm{d}N/\mathrm{d}y$ depends on x. In that case the original $\mathrm{d}N/\mathrm{d}x$ relation was to be convoluted with the $\mathrm{d}N/\mathrm{d}y(x)$ relation. The

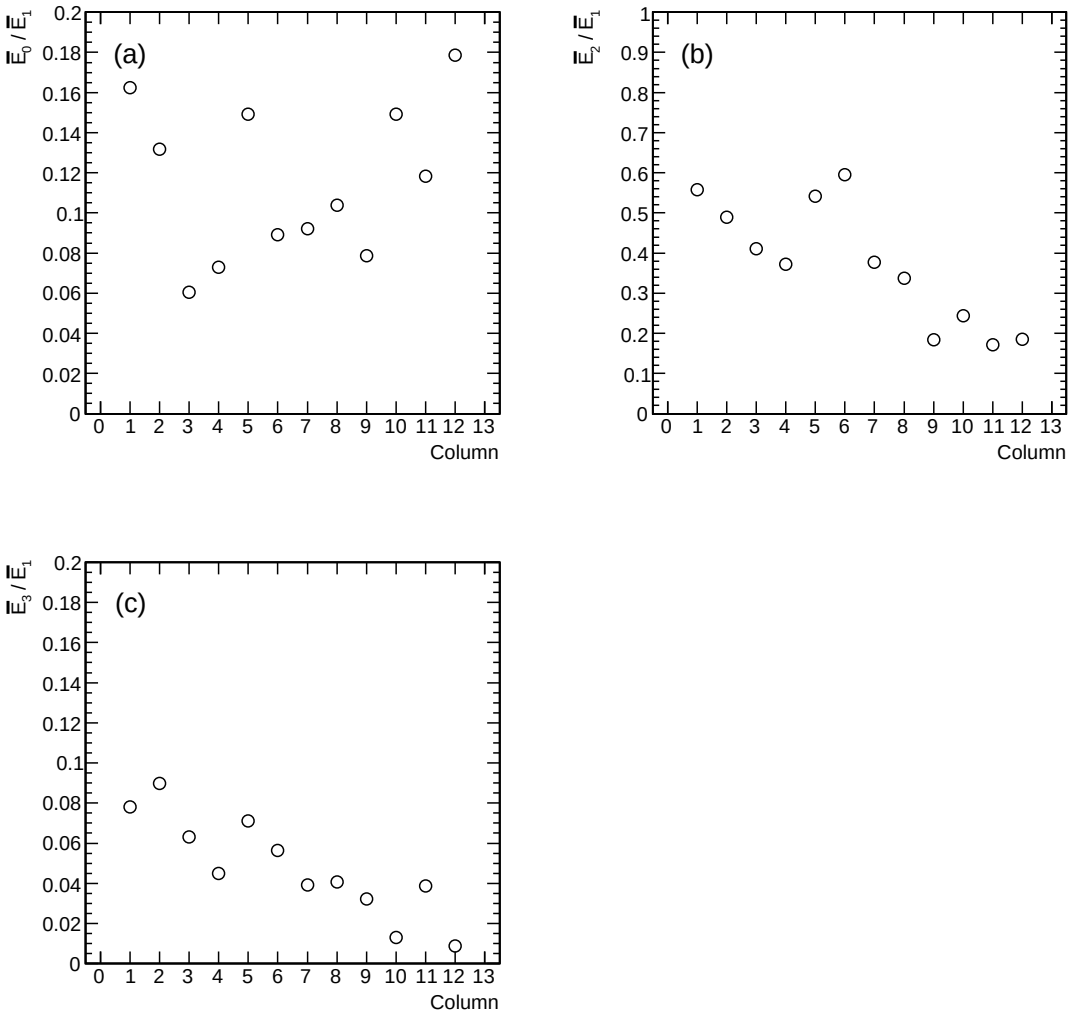

Figure 4.14: Fractions $\bar{E}_r^n/\bar{E}_1^n$ of the mean energies in row r and row 1 (where the maximum energy is deposited) as a function of the column number n for (a) $r = 0$, (b) $r = 2$, and (c) $r = 3$ in the LER period. The energies were reconstructed using the original calibration. There is no smooth dependence of the fractions on the column number. Note that the errors on the mean values (standard deviation) are smaller than the markers.

histogram deviates from the expected behavior. Particularly severe miscalibration is visible in column 5 and 6; events seem to be missing in row 1 and appear in row 2 instead. It is likely that the cells in row 2 were over-calibrated causing the measured energy to be too large and vice versa for the cells in row 1. As the maximum was

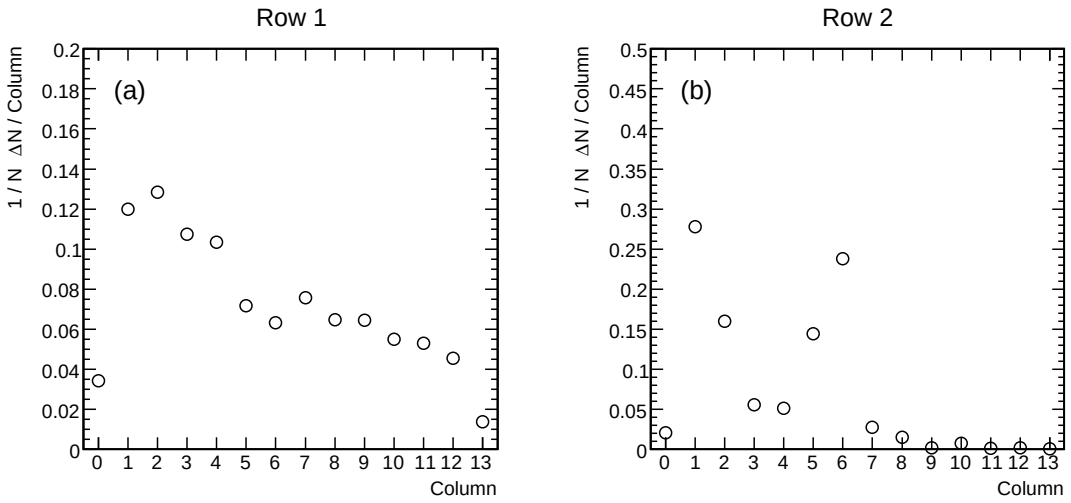

Figure 4.15: Number of events in a particular column in LER data with (a) the hottest cell in row 1, (b) the hottest cell in row 2. The deviations from a smoothly decreasing relation, like in column 5 and 6, reveal the relative miscalibration of the cells within one column.

close to the border between row 1 and row 2, the hottest cell in this case might have been wrongly reconstructed in row 2.

4.6.3 Absolute energy calibration

Another residual miscalibration, besides the relative miscalibration within one column, has been identified. If the hottest cell is located in column 0 and 1 or 12 and 13, the 5×5 reconstruction volume exceeds the edges of the 6 m tagger (comp. Fig. 4.6(b)). Therefore, the reconstructed energy was expected to be smaller than the true energy. This is visible for column 0 and 1 in Fig. 4.16 (b).

The shower profile Fig. 4.16 (a) shows the relative amount of energy deposited in the different columns for an electron hitting the 6 m tagger. The columns at the left-hand side of the maximum contain about 10% of the shower energy. As a consequence, the drop in energy in column 0 in Fig. 4.16 (b) should be also of the order of 10%, if the calibration is correct. This is not observed; the drop is $\approx 40\%$. On the other hand, there is hardly any drop visible for column 12 and 13 although it should be even larger than for column 0 and 1, as follows from the asymmetry of the shower profile in Fig. 4.16 (a).

The original calibration was based on the assumption that the energy of the electron measured in the 6 m tagger and the energy of the photon measured via e^+e^- conversion in the spectrometer should on average be equal to the initial electron

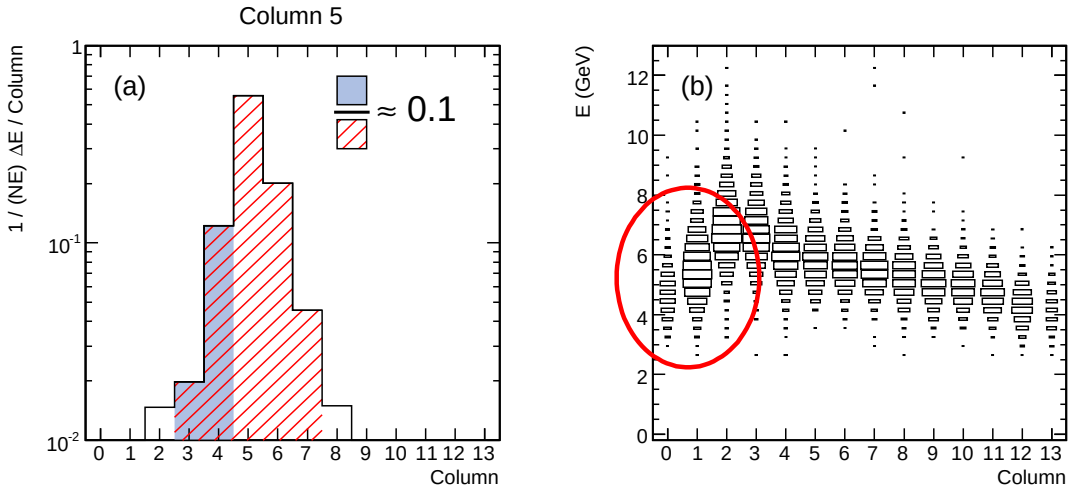

Figure 4.16: (a) Normalized transverse shower profile for events with the hottest cell in column 5 from the LER period. The hashed columns were included in the original energy reconstruction volume. (b) Distribution of reconstructed energy versus column. The marked energy drop at the left side is larger than expected.

beam energy. Thus, the distribution of the sum of the energies measured in the 6 m tagger and in the spectrometer should be centered around the initial beam energy (see Table B.5 in Appendix B for the initial beam energies). This sum is shown in Fig. 4.17 (a). As the energy reconstruction in column 0 and 1 as well as in column 12 and 13 suffered from the aforementioned effects of the exceeding reconstruction volume, only the events having the hottest cell in columns 2 to 11 were considered in this plot. The same distribution was generated individually for each column and fitted with a Gaussian. The mean values of these Gaussians are plotted in Fig. 4.17 (b) and their standard deviations are given as error bars. The figures reveal deviations from the initial beam energy of the order of 1%.

4.7 Strategy for an improvement of the calibration

It is the objective of the presented studies to investigate possible techniques to improve the calibration of the 6 m tagger. All approaches used the original calibration constants as a basis to determine the new constants. The original calibration constants were expected to correctly

- compensate for overall effects of radiation damages per column. The fibers were exposed to the particles in the electromagnetic showers in the 6 m tagger

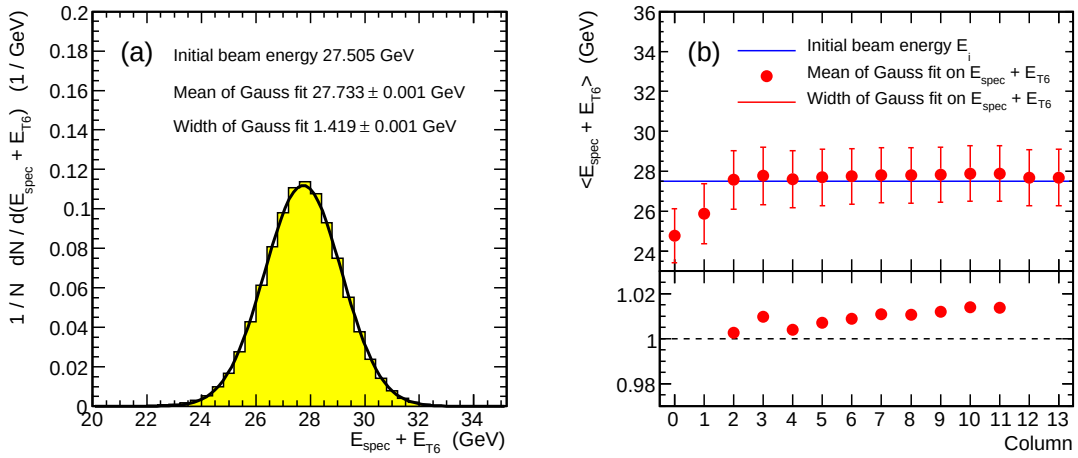

Figure 4.17: (a) Sum of the energies measured in the spectrometer and in the 6 m tagger in the LER period. All events were considered with the hottest cell between column 2 and 11. The mean of a Gaussian fit deviates by 1% from the initial beam energy. (b) The mean values of a Gaussian fit on the same sum, separately for each column of the 6 m tagger. The error bars give the standard deviation of the Gaussian. The bottom plot states the ratio between the measured mean value and the nominal beam energy (for the central columns 2 to 11).

as well as to scattered synchrotron radiation[4] while HERA was running. As a consequence, they darkened and transmitted less light. This had to be compensated for by increasing the calibration constants;

- provide a basis calibration for the following correction procedure which relies on the correct determination of, for example, the hottest cell in the first place.

The correction procedures were aimed to determine *correction factors*. These were used as multiplicative factors to the original calibration constants to obtain the new calibration constants:

$$c_k^{\text{new}} = \left(\prod_i^N c_k^i \right) c_k^{\text{orig}}.$$

The new calibration constant, c_k^{new}, for cell k was obtained by multiplying the original calibration constant, c_k^{orig}, with N correction factors, c_k^i. The new constants were meant to cure the effects of miscalibration described in the previous Section:

[4] As the 6 m tagger was located inside the HERA ring it was not exposed to direct synchrotron radiation.

- compensation of local effects of radiation damage, i.e. correction of the relative calibration within one column;
- correction of the overall energy calibration, in particular at the edges of the 6 m tagger;
- reduction of the energy reconstruction volume to 3×3 cells.

Since these corrections were expected not to have fast variations with time, they were calculated integrating over long time periods. In this way, the data sample was large enough to provide sufficient statistics for a reliable determination of the correction factors.

4.8 Monte Carlo simulation

A simulation of the 6 m tagger was included within the Monte Carlo simulation of the ZEUS detector system. There were, however, severe disagreements between the measured data and the predictions, for example in the energy spectrum. The problems were related among others to the difficulties of the simulation of the magnetic fields in front of the 6 m tagger and of unknown inhomogeneities in the response of the fibers of the 6 m tagger. Although a lot of progress toward a better description has been made [23], there was no reliable simulation available by the time the presented studies were done.

It was therefore decided to abandon the use of the Monte Carlo simulation and to rely solely on the data which was possible since the spectrometer as well as the photon calorimeter could be used as references. This is the reason why, for example, the studies of the shape of the electromagnetic showers in the 6 m tagger (Section 6.2.1) or the event selection studies (Section 7.1) were not based on Monte Carlo simulations.

5 Event selection

In this Chapter the basic selection of Bethe-Heitler events is presented. The selection aimed primarily at a high purity of the data sample. The efficiency of the selection was not an issue due to the large statistics available for the analysis.

5.1 `6mtake` quality flags

Each run was assigned a flag consisting of an integer number indicating the quality of the data. In general a positive number indicated good quality and a negative number worse quality. This number was derived by investigating the details of the calibration constants and of the recorded data [26, 27].

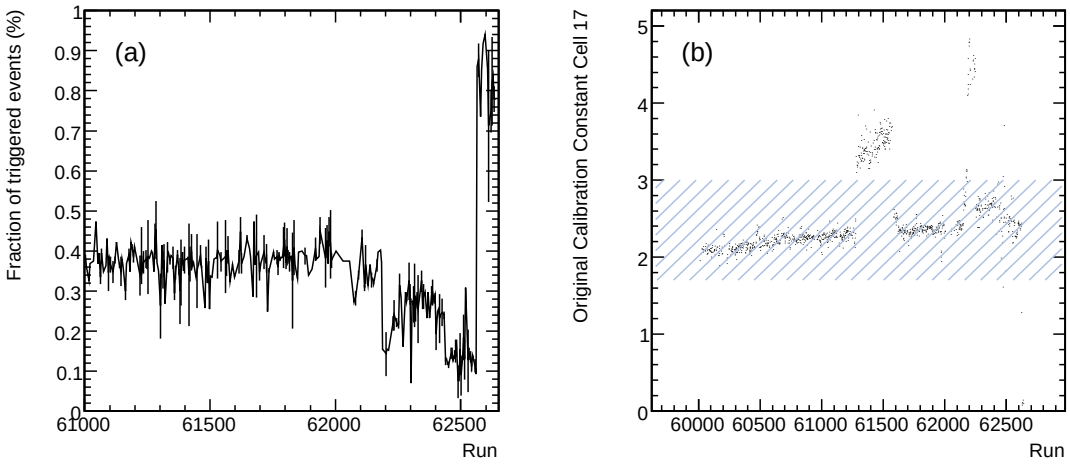

Figure 5.1: (a) Fraction of events in the LUMI system files with a coincidence of a good event in the 6 m tagger and in the spectrometer for some runs of the HER period. (b) Original calibration constants in cell 17 for some runs of the HER period. Runs in which the constants lay outside the hashed band were flagged as problematic. They correspond mainly to runs in which the spectrometer had technical problems [26, 27].

The following criteria were used (a short overview of the definitions of the different flags is given in Table 5.1.):

- the calibration was based on Bethe-Heitler events from files stored by the LUMI system. The fraction of the number of events in these files with a coincidence of a good event in the 6 m tagger and in the spectrometer is shown in Fig. 5.1 (a) for part of the HER period as a function of the run number. It is relatively constant at about 0.4%. Runs in which this fraction was significantly lower were considered as problematic and flagged '-1' if they were short (runs with less than 15000 TLT events) and '-2' if they were long (runs with more than 15000 TLT events);

- the calibration constants were generally stable in time (comp. Section 4.5). A horizontal band taking into account the spread was fitted around their mean value, as shown in Fig 5.1 (b) for part of the HER period. If in one run the constants lay outside this band in one or more cells the run was also considered problematic and generally assigned the flag '-3'. Note that there was a strong correlation between the cells: if the constants were off the band in one particular cell they were usually off in other cells as well;

- if the files storing the data from a particular run suffered corruption and could not be read out, the run was assigned the flag '-4';

- as the calibration procedure depended on the energy measured in the spectrometer, the quality of the spectrometer data was considered. This criterion was correlated with the aforementioned ones. For instance, in runs in which the spectrometer was not working well it was likely that the calibration constants were determined incorrectly and lay outside the band, or that the number of good 6 m tagger-spectrometer coincidences was lower than the average. For example, the range around run 61500 with calibration constants outside the band in Fig. 5.1 (b) corresponds to a period during which the spectrometer suffered technical problems. Runs with bad quality of the spectrometer data were flagged '-5';

- calibration constants were only determined for long runs; short runs without any of the above problems were considered good and flagged with '2';

- long runs without any of the problems stated above were considered good and assigned the flag '1'.

Runs with a flag different than '1' i.e. short good runs and problematic runs are nonetheless available in the ZEUS analysis framework. They were reconstructed using the calibration constants of the closest long good run.

The definitions of the 6mtake quality flags are summarized in Table 5.1. The fraction in percentage of integrated luminosity of the runs flagged with the different qualities is stated. Runs in which the spectrometer did not work properly amount to the by far largest contribution to the problematic runs.

6mtake	Size	Definition	% of L
1	Long	Calib const from this run	72.0
2	Short	Calib const from nearest good run	1.2
-1	Short	Low number of coincidences	0.1
-2	Long	Low number of coincidences	0.1
-3	Long	Calib const off band	1.1
-4	Long	Corrupted files	2.1
-5	—	Bad spectrometer runs	23.0

Table 5.1: Definitions of the 6mtake quality flags and the amount in percentage of integrated luminosity, L, of runs flagged with the different qualities.

The studies presented in the following were done using runs which met the 6mtake quality conditions '1' or '2'.

5.2 Selection of run periods

It was checked that the correction to the original calibration constants remained relatively stable over longer run periods. Different run ranges were therefore selected during which the HERA machine parameters, for example the center of mass energy or the magnetic fields, did not change. A set of correction factors was extracted for each period, using Bethe-Heitler events collected in that period. The chosen run ranges are listed in Table 5.2.

Label	Runs	Dates
MER	71000 - 71414	1 Jun 2007 to 2 Jul 2007
LER	70000 - 70854	26 Mar 2007 to 1 Jun 2007
HER1s	61548 - 62154	4 Dec 2006 to 20 Feb 2007
HER2s	60645 - 61280	12 Sep 2006 to 9 Nov 2006
HER3	60011 - 60644	16 Jul 2006 to 12 Sep 2006

Table 5.2: Run periods for which different sets of correction factors were obtained.

When the HERA machine switched to different proton beam energies in the LER and MER periods, some machine parameters were changed. Some of these changes had a direct impact on the energy spectrum of the electrons observed in the 6 m tagger. For instance the magnetic field of the GG dipole magnet, which bent the electrons in front of the 6 m tagger, was altered, and also the electron beam energy was varied ($\approx 0.5\%$). Therefore, different sets of correction factors were determined

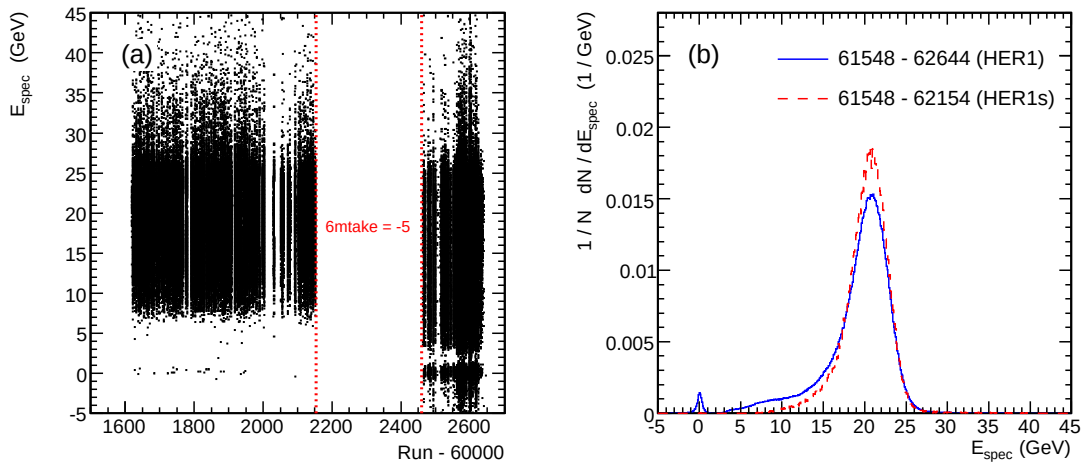

Figure 5.2: (a) Energy measured in the spectrometer versus the run number for the HER1 period. After the offline period of the spectrometer (`6mtake` $= -5$), the selection of Bethe-Heitler events did not work properly anymore; events with too low energies were included. (b) Comparison of the energy spectra of the spectrometer for HER1 and HER1s periods.

for the LER and MER periods. The HER period was subdivided further since its duration in time was much longer.

On December 4, 2006, the polarization of the electron spin rotators was inverted [28]. The time span from this date to the end of the HER period (the runs from 61548 to 62644, (*HER1*), was investigated as a possible range for the determination of a set of correction factors.

Some problems were affecting the spectrometer data taking during the HER1 period. By looking at the energy measured in the spectrometer, Fig. 5.2 (a), it turns out that it returned unexpected results at the end of the period (from run 62450 onward). The energy spectrum had a large low energy shoulder and an extra peak around 0 GeV. Before that period, the spectrometer was offline due to technical problems. The corresponding runs (62150 to 62450) were consequently marked with the `6mtake` quality flag '-5' and not included in the analysis (therefore the empty band in Fig. 5.2 (a)). When the spectrometer was put back online, some trigger parameters were changed such that the standard selection of Bethe-Heitler events (as described in Section 5.3) was not possible anymore. The data sample was therefore contaminated with non-Bethe-Heitler events. This became apparent in the low energy shoulder and in the peak at 0 GeV in the energy spectrum of the

spectrometer (solid curve in Fig. 5.2 (b)).

Owing to the difficulties in selecting a clean Bethe-Heitler sample out of these data, it was decided to exclude the runs at the end of the HER1 period for the determination of the set of correction factors. They were produced only from events of the shorter run range 61548 to 62154, (*HER1s*). In that run range, the extra peak in the energy spectrum of the spectrometer was not apparent anymore and the low energy shoulder was strongly reduced (dashed curve in Fig. 5.2 (b)). The remaining shoulder was due to radiative corrections and is discussed in Section 6.2.2.2.

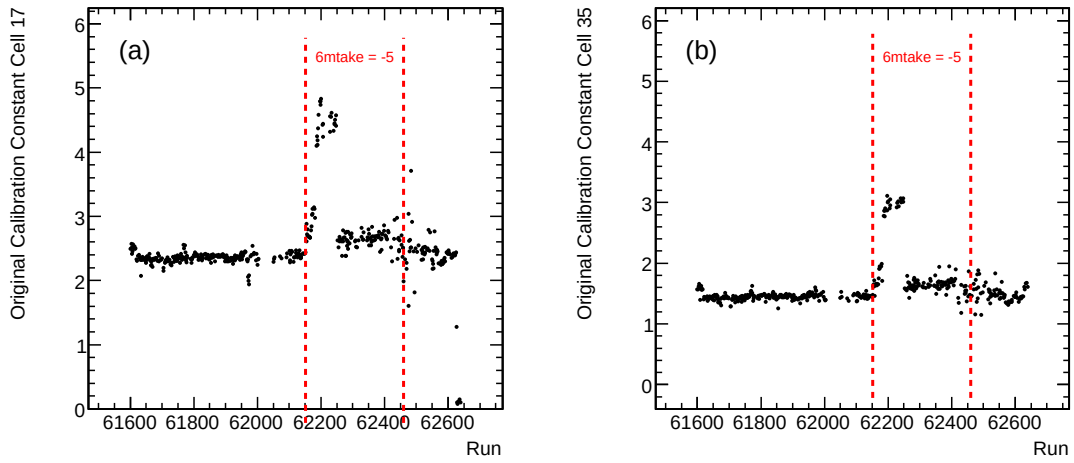

Figure 5.3: Example of the original calibration constants during the HER1 period.

The original calibration constants of the excluded range at the end of the HER1 period, from run 62460 onward, seemed nonetheless to have reasonable values, comparable to the ones of the period before run 62154 (comp. Fig. 5.3). The correction factors of the HER1s set can therefore also be applied in this period at the end of HER1, which is not given any negative `6mtake` flag.

The time span before 61548 back to run 60011 (July 16, 2006), which was the first run for which original calibration constants existed, was further investigated. There was a period (from run 61280 to 61547) during which the spectrometer was not working properly (`6mtake` $= -5$) and which could consequently not be used for the generation of correction factors. The remaining runs before 61280 did not feature any restrictions. They were therefore divided into two periods, *HER2s* and *HER3*, of an equal number of runs, corresponding roughly to the number of runs during HER1s, as listed in Table 5.2.

5.3 Selection of Bethe-Heitler events

Electrons from the Bethe-Heitler process within a certain energy range were detected by the 6 m tagger while the corresponding photons were measured either with the photon calorimeter or the photon spectrometer, as discussed previously (Section 3.2). Bethe-Heitler events could therefore be selected by requiring a simultaneous hit in the 6 m tagger and in the spectrometer. The photoproduction events were expected not to feature such a coincidence. A possible contribution from random coincidences was neglected.

The files written by the LUMI system stored the trigger information of both the 6 m tagger and the spectrometer as well as some information on the quality of the event reconstructed by the spectrometer. The trigger conditions were defined as follows [21, 22]:

6 m tagger trigger: the signal in ADC counts had to be larger by $8\sigma_{\mathcal{P}}$ or more than the pedestal in at least one cell, where $\sigma_{\mathcal{P}}$ is the width of a Gaussian fit to the peak around the pedestal;

Spectrometer trigger: a minimum signal in ADC counts was required in both the modules;

Spectrometer quality: the channel with maximum energy had not to be at the edge and the total energy had to be larger than 3.5 GeV in each module.

If both the spectrometer trigger fired (`TAGGER_6m_TRIGGER & 2`) and the 6 m tagger trigger fired (`TAGGER_6m_AFLAGS & 0x10`), the coincidence condition was met. Additionally, the event in the spectrometer was required to have good quality (`SPEC_flags & 2`) [21].

The effect of the selection can be seen in the distributions of the energy measured by the 6 m tagger (Fig. 5.4) for the runs 70000 to 70300 as an example. If only the spectrometer trigger was required (Fig. 5.4 (a)) a lot of events contribute with no energy deposition in the 6 m tagger creating a peak at 0 GeV. The reason is that the energy acceptance range of the spectrometer was larger than that of the 6 m tagger. It ranged roughly from 10 to 30 GeV [15], while the 6 m tagger measured electrons from about 4 to 7 GeV corresponding to photons with an energy of roughly 20.5 to 23.5 GeV. In many events the spectrometer consequently detected a photon while the corresponding electron was out of the 6 m tagger acceptance. The peak around 0 GeV vanishes if the 6 m tagger trigger is requested on top of the spectrometer trigger (Fig. 5.4 (b)): in this case there is a coincidence of a hit in the spectrometer and an electron in the 6 m tagger. The additional request of the quality flag on the spectrometer rejects $\approx 30\%$ of the events. The shape of the energy distribution in the 6 m tagger remains unchanged (Fig. 5.4 (c)).

A different way to illustrate the effect of the trigger and quality flags on the event selection and to evaluate the quality of an event in the 6 m tagger was to study the

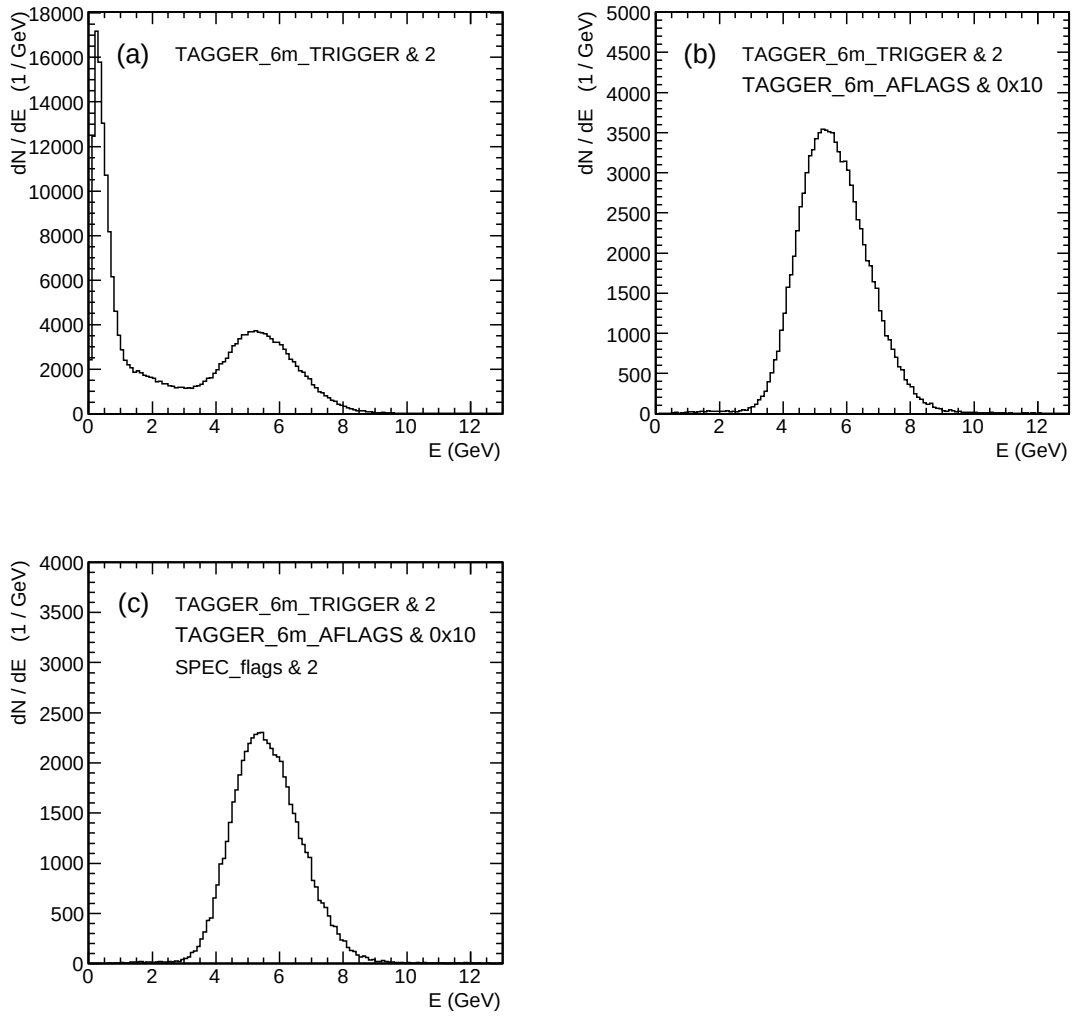

Figure 5.4: Effect of the trigger and quality flags on the event selection. Shown is the energy distribution in the 6 m tagger for events with (a) a hit in the spectrometer, (b) a hit in the spectrometer and a hit in the 6 m tagger, and (c) a good quality hit in the spectrometer and a hit in the 6 m tagger (for events from runs 70000 to 70300).

$(E, E_{\mathrm{hot}}/E)$ distribution (Fig. 5.5, runs 70000 to 70300 as an example). Here, E_{hot} is the energy in the hottest cell and E is the energy of the shower. The fraction of E_{hot}/E is related to the strength of the confinement of the energy within the central cell of the reconstruction volume. It therefore provides an estimation of the transverse profile of the electromagnetic shower: the sharper the profile, the more

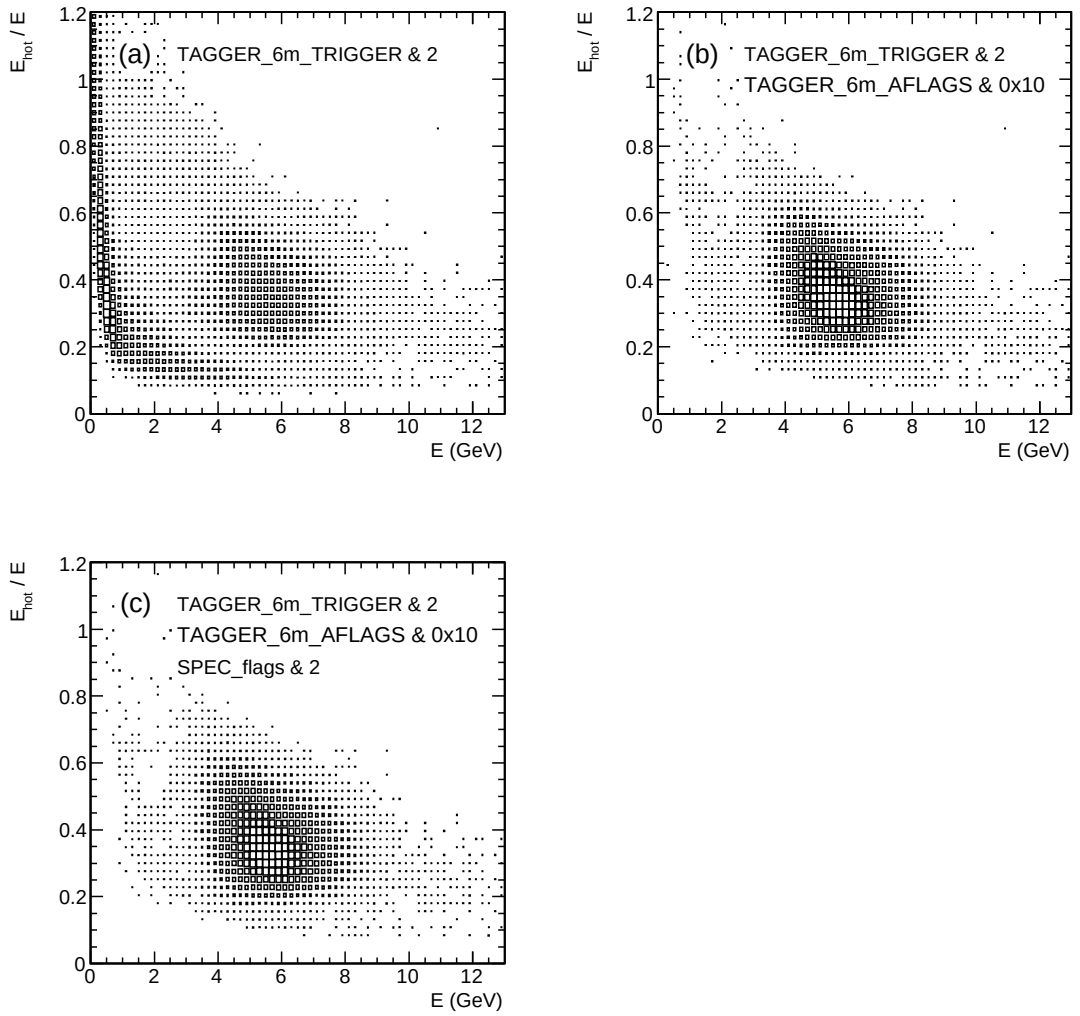

Figure 5.5: Effect of the trigger flags on the events in the $(E, E_{\mathrm{hot}}/E)$ plane (for events in runs 70000 to 70300). The spectrometer quality flag (c) appears to additionally remove some of the events with not well confined showers.

energy is generally expected to be deposited in the central cell. There is, however, also a strong dependence of E_{hot}/E on the position of the shower maximum within the hottest cell. If the maximum is located close to the center of the cell, the fraction is expected to be large. On the other hand, if the shower maximum is close to the edge of one cell, more energy is deposited in the neighboring cells and E_{hot}/E is reduced.

The vast majority of the events meeting the coincidence requirement is located in

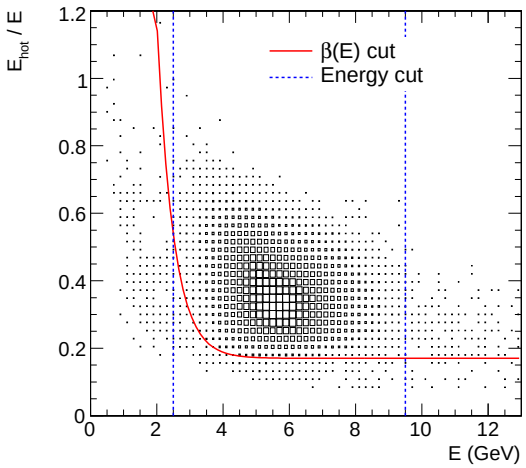

Figure 5.6: Illustration of the cuts on the energy and on the fraction E_{hot}/E in the $(E, E_{\text{hot}}/E)$ plane (for events in runs 70000 to 70300).

a central spot with energies between 3 and 9 GeV and fractions E_{hot}/E between 0.2 and 0.7 (Fig. 5.5 (b)). These events are of good quality and the spot is considered to be the fiducial region. Its vertical width is mainly caused by the aforementioned geometrical effects i.e. by electrons hitting the 6 m tagger at different positions w.r.t. the cell center. The influence of the variation of the transverse shower profile with the energy should be small as the width of an electromagnetic shower is only weakly dependent on the energy (comp. Section 2.1).

Some events lie outside this fiducial region. In some cases their energy is outside the acceptance range of the 6 m tagger. In other cases the reconstruction of the shower might have failed leading to a broadened profile. It seems unlikely that those events are caused by electrons hitting the 6 m tagger exactly between several cells, as this should have happened frequently but the events in question are only a small fraction of the total sample. The spectrometer quality flag appears to additionally remove some of those events (Fig. 5.5 (c)) but a small fraction of events remains outside the fiducial region. They are therefore rejected using the combination of an energy cut

- $2.5 < E < 9.5$ GeV;

and a cut on the fraction E_{hot}/E

- $E_{\text{hot}}/E > \beta(E)$;

which is illustrated in Fig. 5.6. These cuts removed $\approx 1.5\%$ of the events. β was

defined for all run periods as

$$\beta(E) = 0.17 + e^{4-\frac{2E}{\mathrm{GeV}}}.$$

It is an empirically derived cut separating events with well confined electromagnetic showers from events with a smeared shower profile.

5.4 Corrupted events

Events having ADC counts corresponding to non-physical energy values were found in the data taken with the 6 m tagger. The plots shown in the following as an example were done using the data taken during the LER period. The other periods were also investigated and the results were found to be similar to those of the LER period.

5.4.1 Signature of corrupted events

The data acquisition system for the 6 m tagger worked as follows. The analogue signals of the photomultipliers of the 6 m tagger were converted to unsigned 12-bit numbers by ADCs. They were transfered to five readout boards, one for each row of the 6 m tagger. Four empty bits were added at the boards to each ADC count leading to 16-bit numbers which were used for further processing [29].

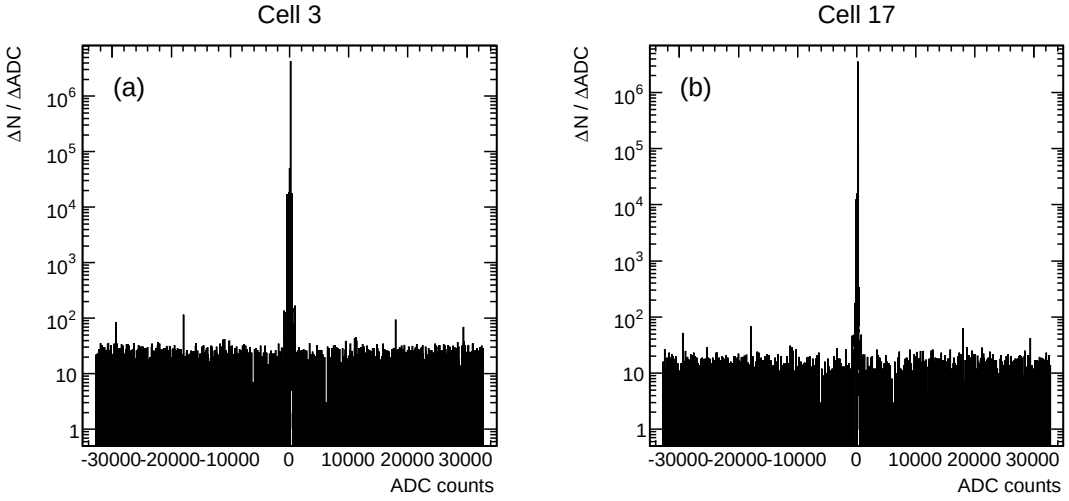

Figure 5.7: Example spectra of ADC counts in cells 3 and 17. ADC counts lower than 0 or greater than 4095 were registered in some events.

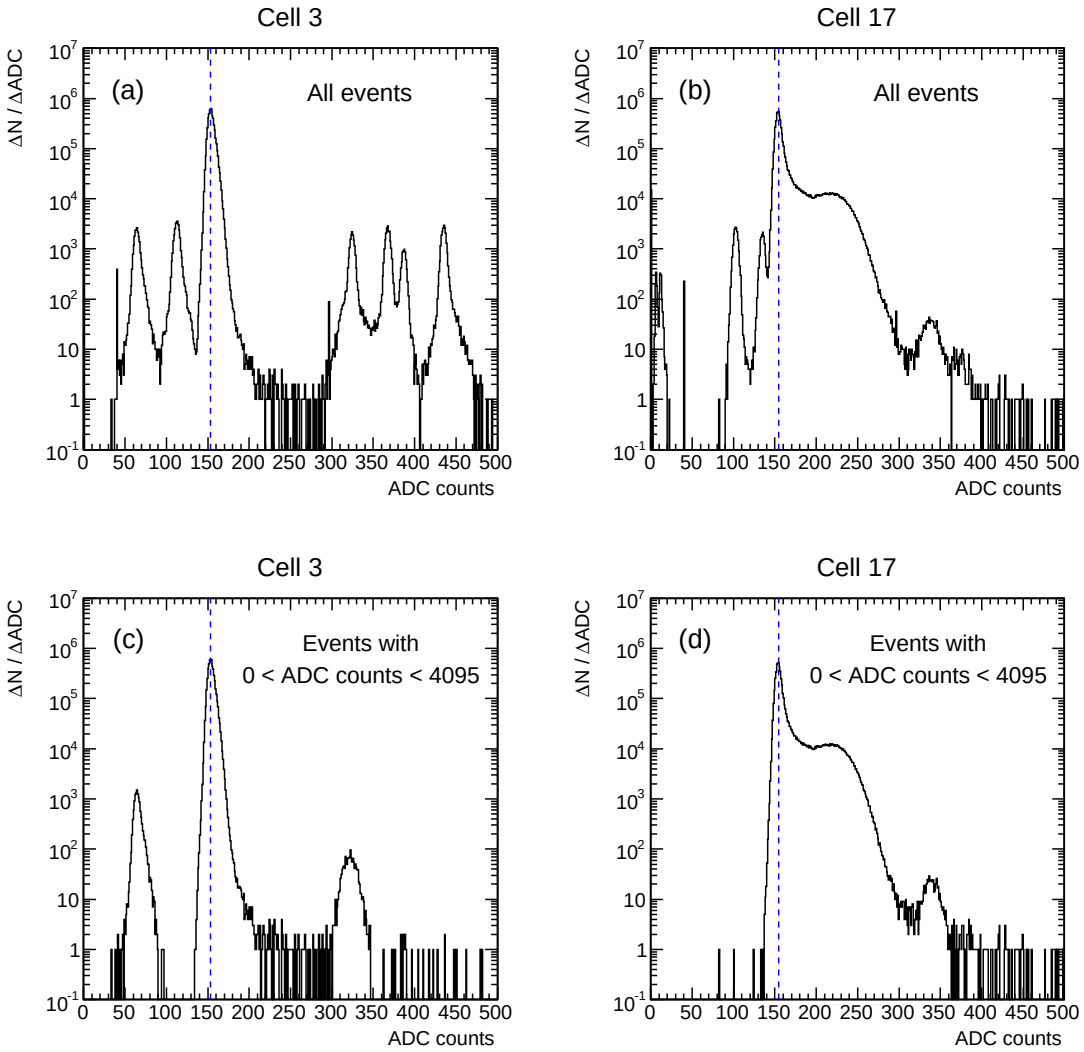

Figure 5.8: Example spectra of ADC counts around the pedestals in cells 3 and 17. (a),(b) Extra peaks off the pedestal peak were registered in some events. (c),(d) They were reduced when rejecting events with ADC counts out of range due to a correlation of corrupted cells. The dashed lines indicate the pedestal values.

The corruption of the ADC counts in an event became manifest in two effects. First, the ADC counts exceeded the range allowed for unsigned 12-bit numbers (0 to 4095) in one or more of the 70 channels of the 6 m tagger. The counts in corrupted events filled the whole range of 16-bit numbers, from −32768 to +32767; example spectra of two cells from different rows of the 6 m tagger are shown in

Fig. 5.7. Second, extra peaks were found in the ADC spectrum, this time within the allowed range of unsigned 12-bit numbers. They were located next to and on top of the pedestal as well as the signal peak. The actual positions of those extra peaks depended on the cell. An example is shown in Fig. 5.8 (a) and (b).

In these kind of events, usually two or three cells in the same row of the 6 m tagger showed corruption. This correlation suggests that the corruption occurred at the readout boards since one board per row was used for the readout. It looks likely that in a corrupted event one or more bits were falsely set at the readout boards. In particular, if during the conversion of the ADC counts to 16-bit numbers one or more non-empty bits were added to the original 12-bit number the resulting counts would exceed the allowed range, as observed. Investigations of the bit pattern were made to resolve whether it was possible to recover the affected events. No pattern, like for example a shift in the bit structure or a bit remaining from previous events, was found.

In conclusion, no way to recover the corrupted events was found. It was therefore necessary to exclude them.

5.4.2 Definition and rejection of corrupted events

The two corruption signatures described above were strongly correlated. When all the events with ADC counts smaller than 0 or greater than 4095 in one or more cells were rejected, most of the events forming extra peaks were also removed. Nonetheless, some extra peaks remained in the spectrum and had to be rejected. This is shown in Fig. 5.8 (c) and (d). Defining and removing them was not straightforward. The peaks on top of the main signal caused the worst difficulties.

As a first attempt, simple cuts on the energy spectrum rather than on the ADC counts were made to avoid the problems arising from the fact that each cell has different pedestals. A way to exclude the peaks on the left hand side of the pedestals, i.e at negative energies, was to require an energy greater than -0.6 GeV in every cell. This value roughly reflects the width of the peak around 0 GeV. By applying this cut, the extra peaks at the right hand side of the pedestal, i.e. at positive energies, disappear, too, due to the aforementioned row-wise correlation. This definition has the disadvantage that it is dependent on the calibration. It was therefore only used as a quick tool during the studies of the χ^2-minimization method described in Section 6.1.

For all later studies a new definition was used which was formulated at the level of ADC counts and was therefore independent of the calibration. Events were considered corrupted if in one or more cells ADC counts occurred which were smaller than $\mathcal{P} - 8\sigma_{\mathcal{P}}$, where $\mathcal{P}$ is the pedestal value and $\sigma_{\mathcal{P}}$ the width of the pedestal peak. $\sigma_{\mathcal{P}}$ is defined as the standard deviation of a Gaussian fit of the ADC spectrum. This fit was done in two steps to be sure that the signal shoulder at the right side of the peak did not affect the determination of $\sigma_{\mathcal{P}}$:

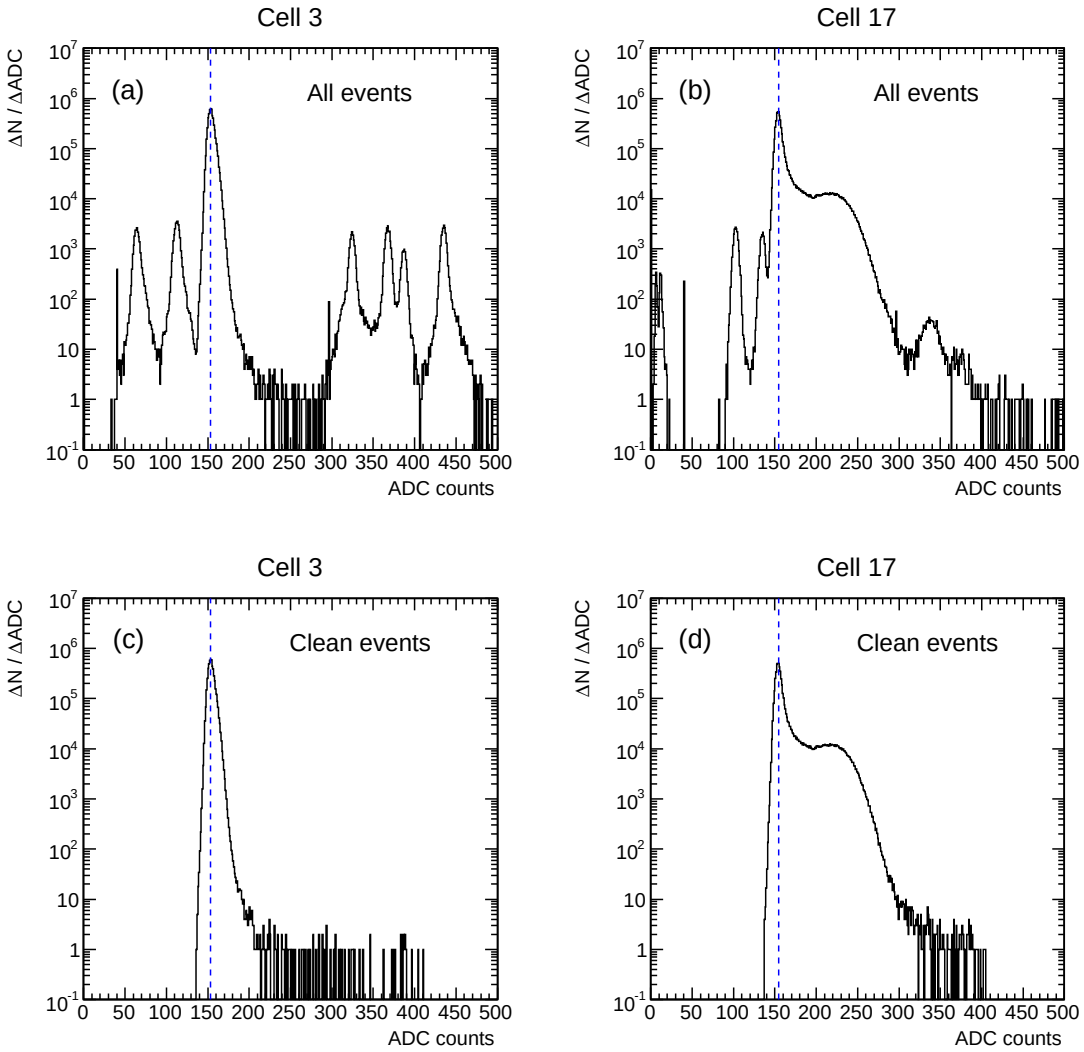

Figure 5.9: ADC spectra in cells 3 and 17 (a),(b) before and (c),(d) after the rejection of the corrupted events. The dashed lines indicate the pedestal values.

1. a rough estimate, σ_1, of the width was obtained via a first fit on the whole spectrum;

2. a second fit was then done on an asymmetric range from 0 to $\mathcal{P} + 3\sigma_1$. The width, σ_2, of this second fit was taken to be the width $\sigma_{\mathcal{P}}$ of the pedestal peak.

To account for changes in time of the response of the channels, the widths were determined individually for the different run periods. Their values are listed in Table B.1 in Appendix B.

This definition of a corrupted events corresponds to a cut on the energy and removes the peaks at negative energies as well as the extra peaks on top of the signal due to the row-wise correlation. To be sure to exclude all the corrupted events, an upper cut was also introduced: an event is corrupted if the ADC counts are above $\mathcal{P} + 80\sigma_{\mathcal{P}}$. This corresponds to the upper end of the signal peak (Fig. 5.8 (c) and (d)).

In summary, an event is considered corrupted if in one or more channels the following condition is not satisfied:

$$\mathcal{P} - 8\sigma_{\mathcal{P}} < \mathcal{A} < \mathcal{P} + 80\sigma_{\mathcal{P}}.$$

This definition also includes the events with negative or too large ADC counts. The rejection power is illustrated in Fig. 5.9.

5.4.3 Occurrence of corrupted events

The amount of corrupted events depended on the data acquisition system used to store them; here, the files recorded by the LUMI system were considered. Between 6 and 8% of the events were corrupted in these files. The exact numbers for each run period are listed in Table 5.3. They were evaluated after cutting on the coincidence and quality condition of the Bethe-Heitler event selection but before the energy and β cut were applied (see Section 5.3). The reason for this was that if the stored ADC counts were corrupted, also the reconstructed energy was possibly incorrect. As the mentioned cuts were based on the energy their effect on corrupted events might have been incorrect, too.

MER	LER	HER1s	HER2s	HER3
6.55%	7.63%	6.15%	5.70%	5.22%

Table 5.3: Amount of corrupted events per run period. The numbers are given in percentage of the total number of events passing the cuts on the coincidence and quality flags of the Bethe-Heitler event selection presented in Section 5.3.

In principle the corrupted events should have been rejected even before the coincidence cut as that was based on the 6 m tagger trigger which in turn was based on ADC counts. There were two different possibilities in which corrupted ADC counts could affect the trigger and thus spoil the event selection: either an event which would not pass the trigger condition fired the trigger, or an event which would pass the trigger condition was rejected.

The first case was unproblematic. It was equally possible to reject the corrupted events before or after the cut on the trigger. Since the identification of corrupted events was computationally extensive it was better done afterward.

The latter case was more problematic as most of the events rejected by the trigger were not stored. Though some events might have been stored because they were triggered by a different detector of the LUMI system, it was not possible to recover them. The events were therefore lost. The amount of affected events might well have been at the percentage level since the overall corruption was of the order of 10% (Table 5.3). Although the efficiency of the selection might thus have been reduced, this was uncritical as for the calibration a high purity was most important and still a large amount of Bethe-Heitler events remained available. As long as the corrupted events occurred randomly, the selection was not biased.

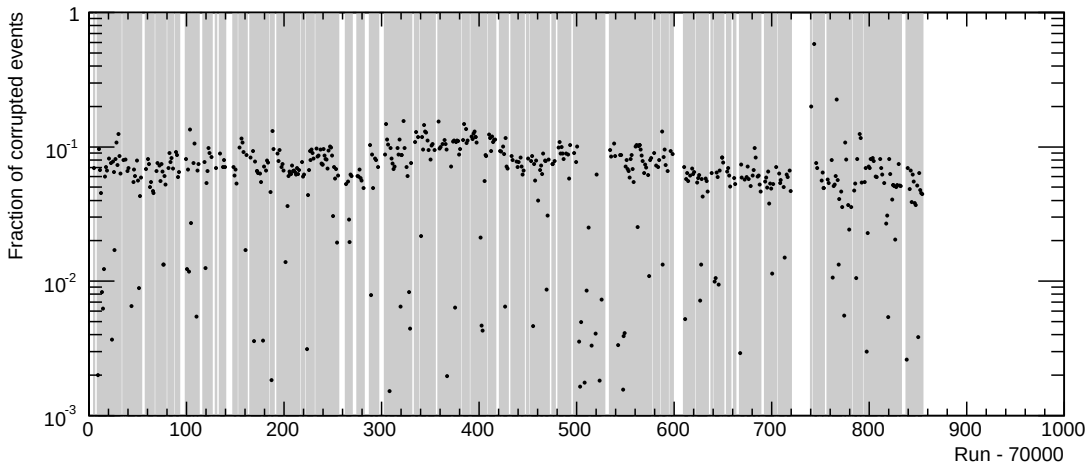

Figure 5.10: The fraction of corrupted events per run. The corrupted events were evenly distributed. Data were available only for runs indicated by the shaded bins.

Figure 5.10 shows the fraction of corrupted events per run. The corrupted events are evenly distributed over the investigated runs; the corruption does not depend on how long the run is. The distribution was generated from the events which met the coincidence conditions i.e. in particular passed the 6 m tagger trigger cut.

Some tests were made to check whether the corruption was happening randomly. If the corruption happened randomly with a mean occurrence p, the probability $P(n)$ of n consecutive clean events was described by an exponential function:

$$P(n) = (1-p)^n = e^{\ln(1-p)n}.$$

Figure 5.11 (a) and (b) show the distribution of the number of clean events between two corrupted events. In (a) events were selected which passed the coincidence cut and in (b) events were selected by a random trigger. The distributions are not

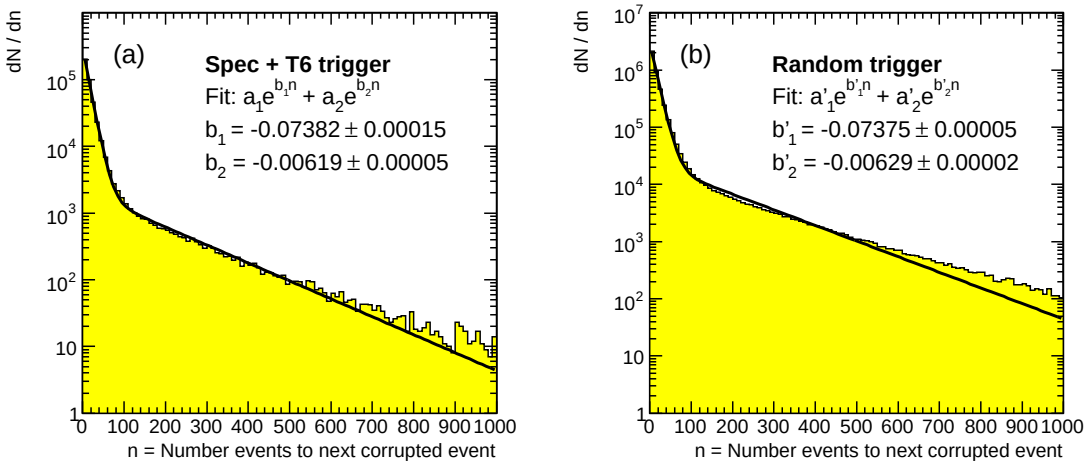

Figure 5.11: The number of events between two corrupted events. (a) Spectrometer and 6 m tagger trigger coincidence required. (b) Random trigger required.

described by a single exponential function but rather by the sum of two exponentials. This behavior is not fully understood.

Nonetheless, corrupted events were rejected to allow a correct energy measurement. The studies presented in the following investigated in detail the energy spectrum observed in the 6 m tagger, using different sets of energy cuts. No evidence was found that the rejection of corrupted events had introduced some kind of bias in the analyzed data samples.

5.5 Summary of the selection of Bethe-Heitler events

The selection criteria for Bethe-Heitler events are summarized in this Section.

Runs were selected which met the

1. `6mtake` quality conditions '1' or '2'.

A coincidence of a good event in the spectrometer and a hit in the 6 m tagger was required by asking the following conditions to be true:

2. 6 m tagger and spectrometer trigger fired;

3. good quality of the event in the spectrometer.

To reject corrupted events it was demanded:

4. $\mathcal{P} - 8\sigma_{\mathcal{P}} < \mathcal{A} < \mathcal{P} + 80\sigma_{\mathcal{P}}$ for each of the 70 channels.

To select only events with a well confined shower in the 6 m tagger in the expected energy range it was additionally required:

5. $E_{\mathrm{hot}}/E > \beta(E)$;

6. $2.5 < E < 9.5$ GeV.

6 Improved calibration procedures

Two different approaches were studied to improve the original calibration of the 6 m tagger and to obtain correction factors to the original constants. Both rely on Bethe-Heitler events as the energy of the electrons hitting the 6 m tagger were in principle known by measuring the energy of the radiated photon with the spectrometer, as discussed in Section 4.5.

As a first attempt a χ^2-minimization method was used. The correction factors were varied to find the best agreement between the expected and measured energy. The studies are presented in Section 6.1; they did not turn out to have the expected result.

A second approach separated the correction procedure into a *vertical* and a *horizontal correction*. The vertical correction made use of the expected properties of the transverse profile of the electromagnetic showers in the 6 m tagger. It allowed a consistent relative calibration within one column for the cells of the first four rows but left the totally reconstructed energy unchanged. The energy reconstruction, especially at the edges of the 6 m tagger, was optimized by the horizontal correction which was a variation of the original calibration procedure. The details of this method are presented in Section 6.2; the final correction factors are given in Appendix C.

6.1 χ^2-minimization

As a first attempt to improve the calibration, the original calibration constants in each cell were weighted with a correction factor. The shower energy reconstructed in this way was compared to the expected energy. The correction factors were varied in order to find the best agreement between the reconstructed and the expected energy. This optimization was done by using a χ^2 method [9, 30].

6.1.1 Technique of the χ^2-minimization

The presented method made use of Bethe-Heitler events. The energy E_{exp} expected in the 6 m tagger was determined from the energy E_{spec} measured by the photon spectrometer. The expected energy was determined in each event ϵ as

$$E^{\epsilon}_{\mathrm{exp}} = E_i - E^{\epsilon}_{\mathrm{spec}},$$

where E_i is the initial beam energy. In this first feasibility study, E_i was approximated with 27.6 GeV; the correct values are given in Table B.5 in Appendix B.

The energy E^ϵ of the electromagnetic shower in the 6 m tagger was reconstructed by summing the energies E_k^ϵ measured in the cells k of a certain volume around the hottest cell (Section 4.3). The original calibration was optimized for a 5×5 reconstruction volume. To improve the calibration ,the energies E_k^ϵ were weighted with correction factors c_k, resulting in the new energy

$$E'^\epsilon = \sum_{k \in V^\epsilon} c_k E_k^\epsilon. \tag{6.1}$$

The reconstruction volume V^ϵ of the improved calibration contained 3×3 cells with the central cell being the hottest cell (Section 4.6.1). The correction factors were assumed to be constant for all events. To determine their values, the function

$$\chi^2(\mathbf{c}) = \sum_{\epsilon=1}^{N} \left(\frac{E_{\text{exp}}^\epsilon - E'^\epsilon}{\sigma^\epsilon} \right)^2 \tag{6.2}$$

was defined. This quantifies the deviation of the measured energy in the 6 m tagger from the expected value. Each summand represents one event. The sum runs over N events. σ^ϵ denotes the error on the measurement of E'^ϵ and E_{exp}^ϵ. They were assumed to be of the order of 20% and therefore the combined error was estimated as

$$\sigma^\epsilon = 0.3\sqrt{E_{\text{exp}}^\epsilon / \text{ GeV}}. \tag{6.3}$$

The correction factors c_k were varied to find their optimal values i.e. the values that minimized χ^2. The minimization was done using the class `TFitterMinuit` [31] of the ROOT-framework which is based on the `Minuit2` package [32]. Each summand in Eq. (6.2) contains the nine correction factors of the cells included in the reconstruction volume V^ϵ of the event ϵ. (If the hottest cell was at the edge of the 6 m tagger, less cells were included accordingly.) As the position of the hottest cell varied, all cells were eventually covered. Hence, correction factors could in principle be obtained for all cells. This is illustrated in Fig. 6.1.

6.1.2 Event selection for the χ^2-minimization

The analysis was performed using the data collected during the LER period. The short runs in the range 70100 to 70199 were used to develop and test the correction procedure[1]. All the plots shown in this Chapter were generated using the data of these runs. As this procedure was not chosen as the final one it was not extended to a larger run range.

[1]The reason for this was that shorter runs were stored on a `dCache` file system and quickly accessible.

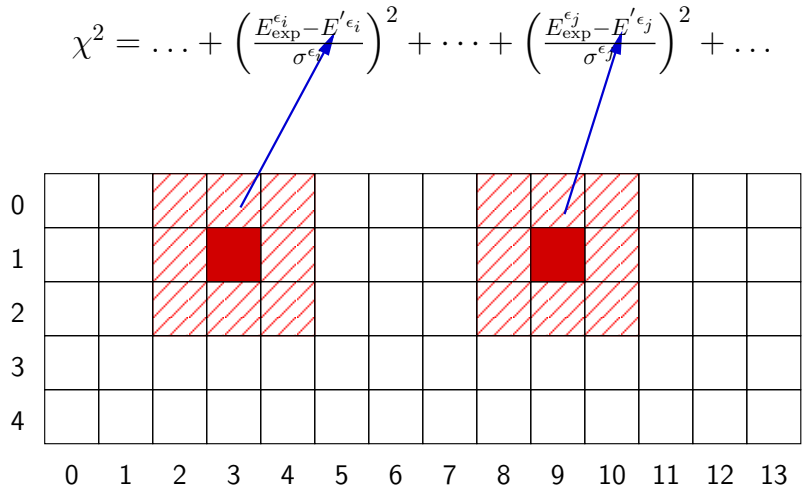

Figure 6.1: The reconstruction volume covered different cells in different events due to the variation of the position of the hottest cell. Therefore all cells were eventually covered.

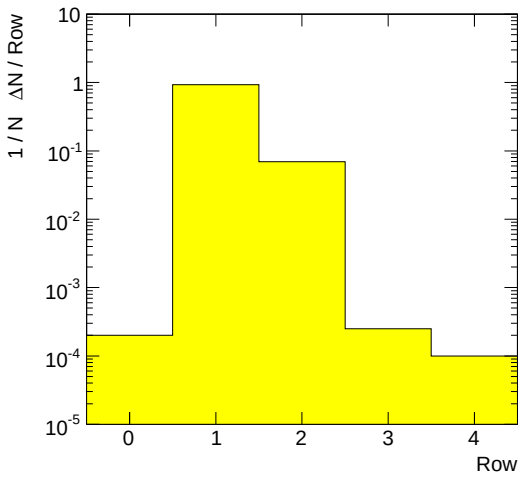

Figure 6.2: The relative amount of events with the hottest cell in a certain row.

Bethe-Heitler events were selected by the six cuts described in Section 5.5. In the LER period about 93% of all Bethe-Heitler events had the hottest cell in row number 1 (Fig. 6.2). They were therefore selected by requiring further

7. the hottest cell in row 1.

In this way the chosen 3×3 reconstruction volume covered cells in the first three

rows of the 6 m tagger; hence correction factors could be determined for these rows.

To avoid the inclusion of outlier events, in which the measured energy differed significantly from the expected energy and which would, due to the quadratic term, have a large impact on the value of χ^2, the cut

8. $|\psi^\epsilon| < 5$

was also applied, where

$$\psi^\epsilon = \frac{E^\epsilon_{\text{exp}} - E'^\epsilon}{\sigma^\epsilon}$$

denotes the non-squared summand of χ^2 in Eq. (6.2).

6.1.3 Results of the χ^2-minimization

The distributions of ψ^ϵ (*pull*) and $(\psi^\epsilon)^2$ before and after the minimization are shown in Fig. 6.3. The mean of ψ^ϵ improved from 1.31 to 0.29 due to the minimization. The standard deviation σ of the mean, however, was not at all affected by the minimization; its value remained at ≈ 2.

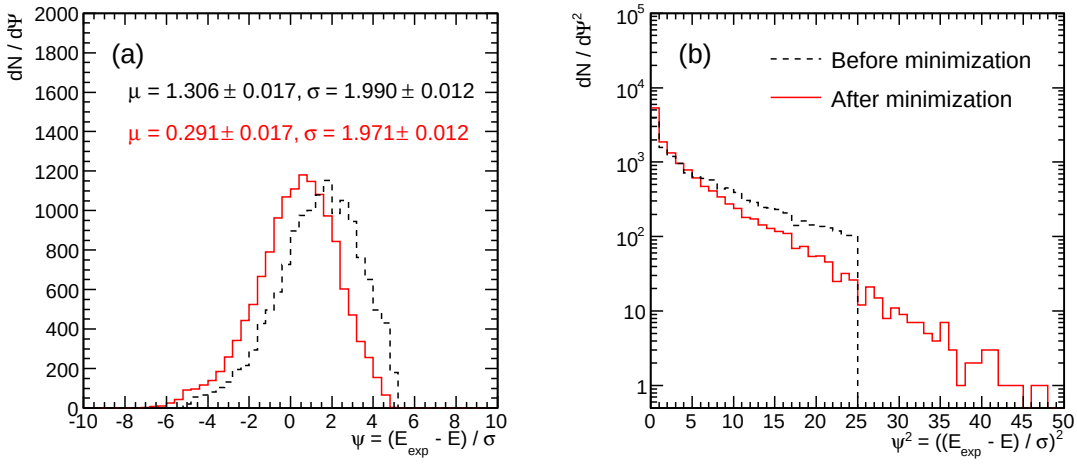

Figure 6.3: Distributions of (a) ψ and (b) ψ^2 before and after the minimization of χ^2. The mean value μ of ψ and its standard deviation σ are stated. The sharp cutoff at $\psi^2 = 25$ in (b) was due to cut 8. of the event selection.

The obtained correction factors in the cells of the first three rows of the 6 m tagger are shown in Fig. 6.4. They are larger than 1 on average because the original calibration constants were obtained assuming that the whole energy of the shower was deposited in a reconstruction volume of 25 cells. The correction factors, as

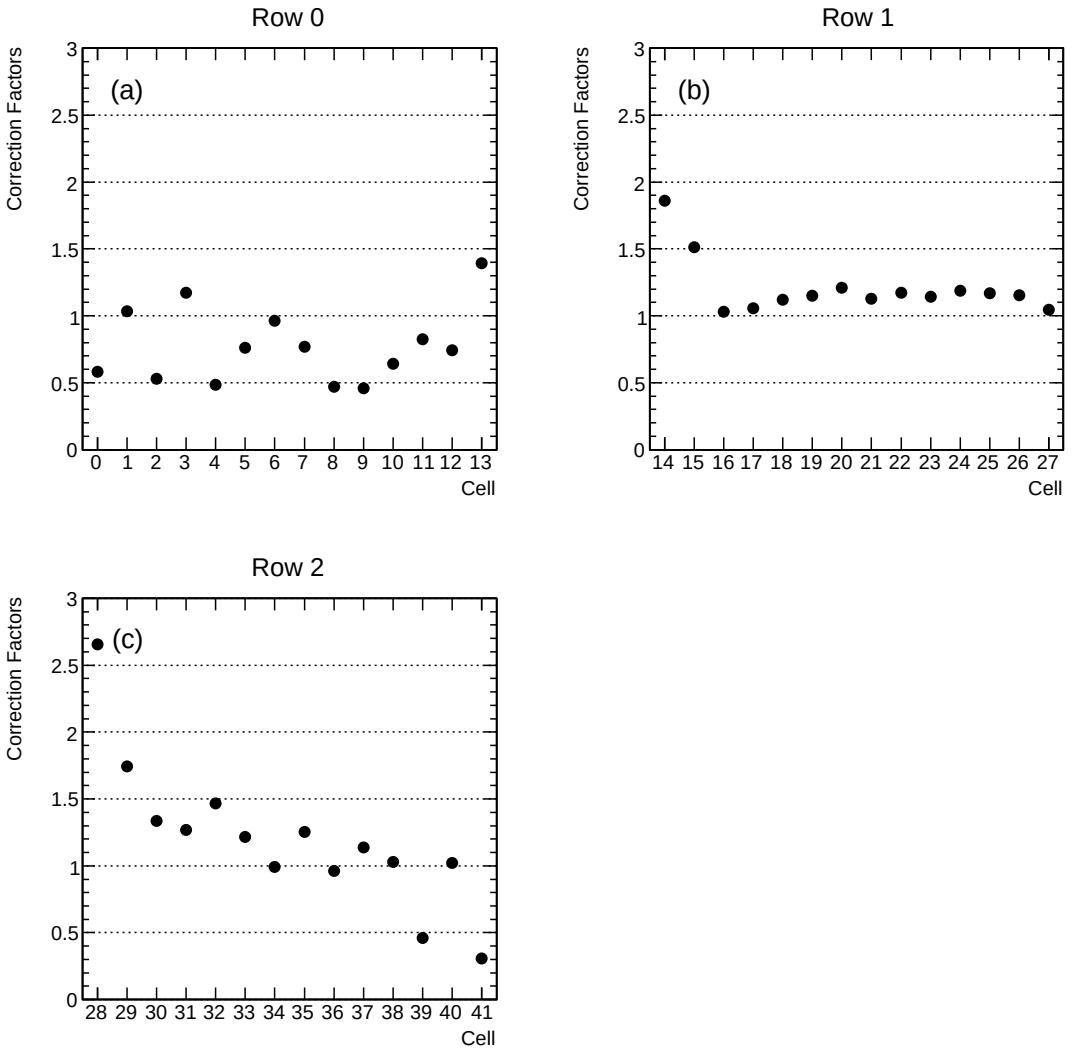

Figure 6.4: Correction factors obtained from the χ^2-minimization.

already stated, were extracted assuming the same energy to be deposited in 9 cells, thus requiring larger contributions from each cell.

Figure 6.5 (a) shows the energy measured in each column of the 6 m tagger. The dependence of the mean energy on the column (Figure 4.8 (b)) was obtained from this plot as illustrated in Fig. 6.6. An energy distribution was projected out of each column and fitted with a Gaussian. The mean value of the Gaussian was taken as the mean energy $\bar{E}$ in that column and the standard deviation of the Gaussian was given as error.

In the same way, the mean expected energy was derived from the distribution of

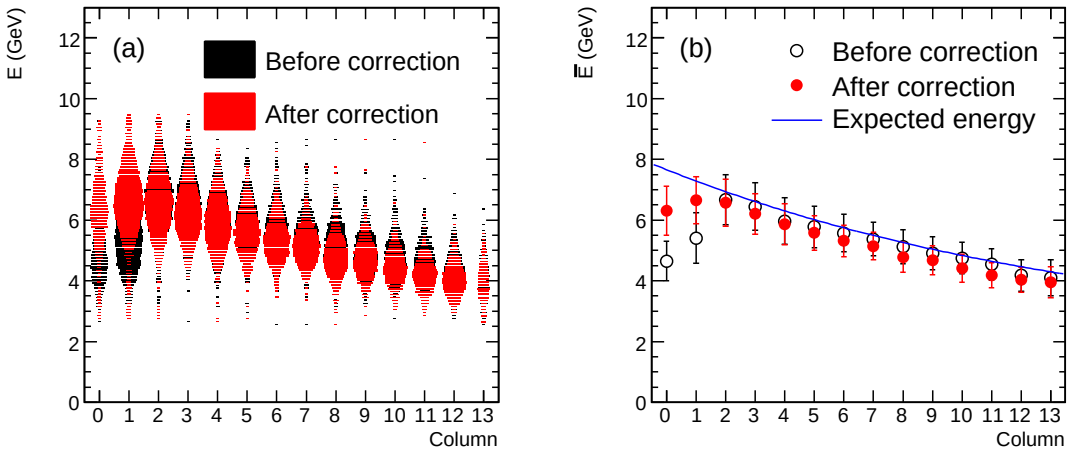

Figure 6.5: (a) Energy and (b) mean energy versus the column as obtained with the original calibration and the correction factors applied. The function $E_{\mathrm{exp}}(n)$ coming from the expected energy is superimposed in (b).

expected energy $E_{\mathrm{exp}} = 27.6\ \mathrm{GeV} - E_{\mathrm{spec}}$ for each column n (as an example column 5 is shown in Fig. 6.7). The mean values as a function of the column were fitted with an exponential function $E_{\mathrm{exp}}(n)$ with offset (comp. Fig. 6.27 and the corresponding discussion). The fitted curve is superimposed in Fig. 6.5 (b).

The distributions of E_{exp} features radiative tails at high energies (Fig. 6.7) which dragged the mean of the Gaussian fit toward higher values and in turn also shifted $E_{\mathrm{exp}}(n)$ toward higher energies. The effect is discussed in detail in Section 6.2.2.2. It is of the order of 4% and it was not considered in these first studies of the minimization method.

The relation between the energy and the column obtained using the new calibration constants as well as that coming from the original calibration are compared to the function of expected energy (Fig. 6.5). This allows to evaluate the performance of the absolute calibration. The systematic difference in energy was due to the aforementioned radiative tails. In these events, $E^{\epsilon}_{\mathrm{exp}}$ is expected to be much larger than E'^{ϵ} and the events could not pass cut 8 of the event selection (Section 6.1.2). They did therefore not contribute to the measured mean energies in the 6 m tagger but to the determination of $E_{\mathrm{exp}}(n)$. Therefore, the values of the mean energies are not compared here. The slope of the distributions corresponds to the expected one.

The original calibration is in particular problematic in the outer columns, as discussed in Section 4.6.3. The quality has improved when applying the correction factors. The drop of energy in column 0 due to the reconstruction method w.r.t. the expected energy is of the order of 15% which was closer to the expected 10%.

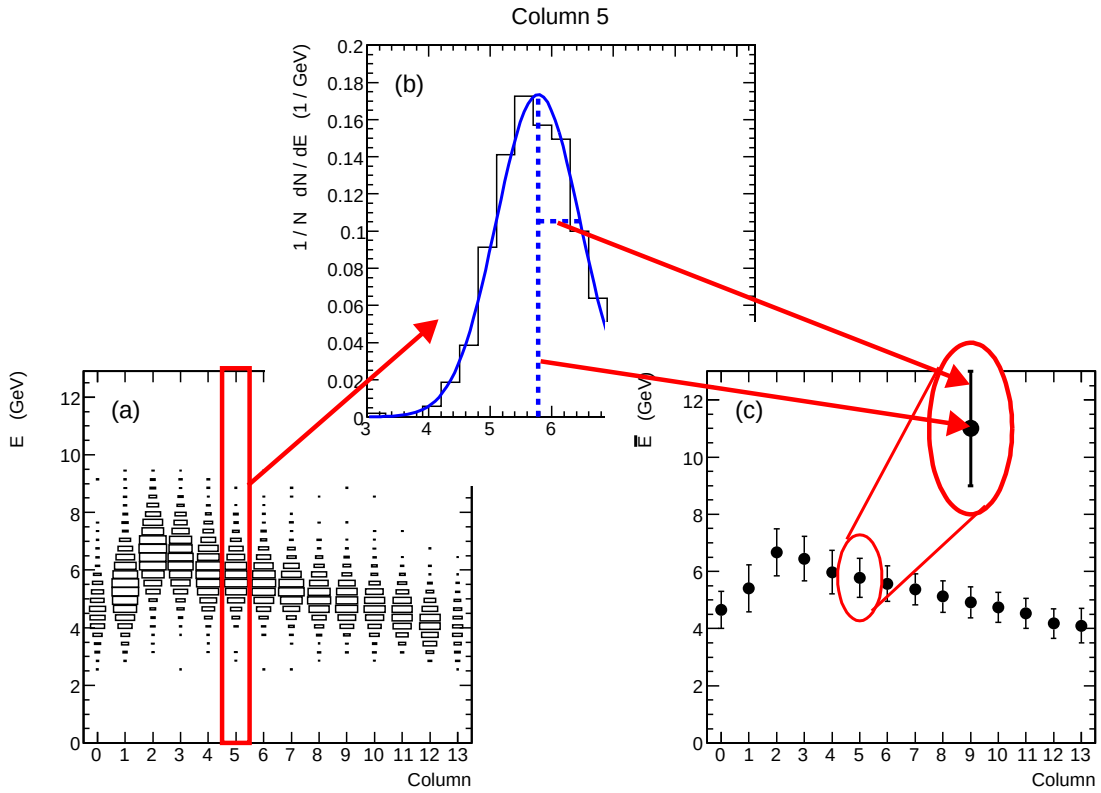

Figure 6.6: Illustration of the determination of the mean energy $\bar{E}$ per column (c). For each column, the energy distribution was projected out of the energy versus column distribution (a). This distribution was fitted with a Gaussian (b). The mean value of the Gaussian was taken as the mean energy $\bar{E}$ and the standard deviation of the Gaussian as its error.

The expected drop in column 13 is not apparent. Moreover there is an obvious miscalibration in column 1: the reconstructed energy is smaller than expected. With the 3×3 reconstruction volume, the energy should have been correctly reconstructed in column 1.

The performance of the relative calibration within one column can be investigated using the column dependence of the fraction of energies in different cells of the same column. A smooth dependence on the column would be expected for a correct relative calibration, as discussed in Section 4.6.2. The fractions $\bar{E}_0/\bar{E}_1$ and $\bar{E}_2/\bar{E}_1$ of the mean energies in the cells in row 0 and row 1 as well as row 2 and row 1, respectively, are given in Fig. 6.8. The behavior did not improve when applying the correction factors.

The distribution of the number of events per column within one row allowed a

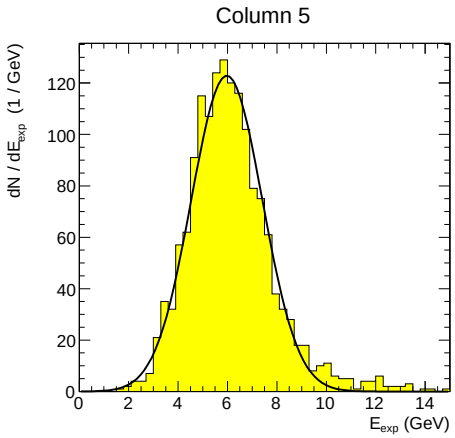

Figure 6.7: Distribution of the expected energy $E_{\mathrm{exp}} = 27.6\ \mathrm{GeV} - E_{\mathrm{spec}}$ for events having the hottest cell in column 5. The mean expected energy was evaluated from a Gaussian fit; it was shifted higher energies due to the presence of a radiative tail.

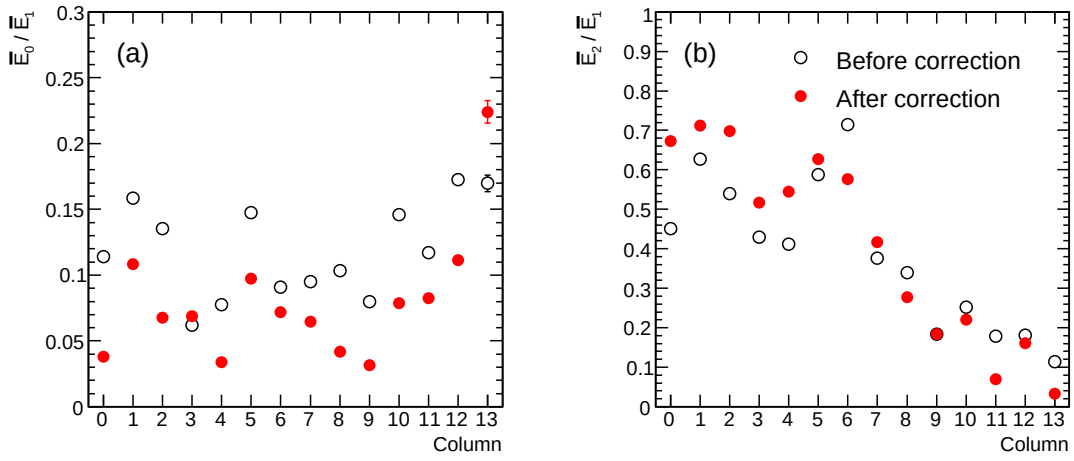

Figure 6.8: Ratios of the mean energy in (a) row 0 and (b) row 2 over the mean energy in row 1 (where the maximum energy is deposited). The values obtained using the original calibration are compared to the ones obtained using the correction factors. Note that the errors on the mean values (standard deviation) are in most cases smaller than the marker points.

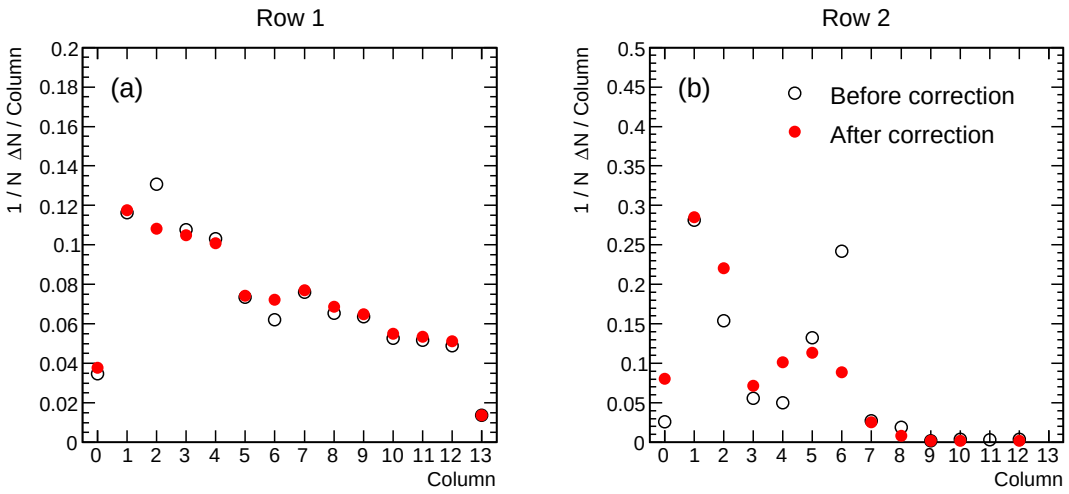

Figure 6.9: Number of events with the hottest cell in a particular column with (a) the hottest cell in row number 1, (b) the hottest cell in row number 2. The distribution obtained with the original calibration is compared to that obtained with the correction factors applied.

further investigation of the relative calibration. The distribution obtained with the original calibration constants deviated from the expected monotonically decreasing behavior, as discussed in Section 4.6.2. There were in particular effects of migration between row 1 and 2 in column 5 and 6. Figure 6.9 shows this distribution compared to the one obtained using the corrected calibration. The miscalibration is not cured.

In conclusion, the correction technique turned out to be incapable of improving the relative calibration of the cells within one column. The reason is probably that the y position of the incident electron was approximately the same in all events in one column (comp. Section 4.4). Local inhomogeneities of the fiber responses could therefore not be detected by varying the y position of the electromagnetic shower and hence the relative amount of energy deposited in each cell.

6.1.4 Other techniques for the χ^2-minimization

Some modifications were made to the method described above in order to improve its performance. They are briefly described in the following.

- If the hottest cell was in one of the two outer columns (0 or 13), part of the reconstruction volume lay outside the 6 m tagger. In this case only the six cells of the reconstruction volume contained in the 6 m tagger were considered for the evaluation of E'^{ϵ} in Eq. (6.1). It is also possible to exclude the events

in which the hottest cell was in one of the outer columns. The cells in those columns are in any case covered by the reconstruction volumes of the events having the hottest cell in columns 1 and 12.

The correction factors obtained in this way differed only in the last two columns and here particularly in row 2 from those shown in Fig. 6.4. No improvement of the relative calibration could be observed in the distributions of Figs. 6.5 to 6.9.

- The expected energy was determined for each event from the energy measured in the photon spectrometer. A different approach used another relation $E^{\mathrm{t6}}_{\mathrm{exp}}(n)$ between the mean energy of the electron hitting the 6 m tagger and the column n containing the hottest cell. It was taken from the relation between the mean energy and the column obtained using the original calibration constants (open markers in Fig. 6.5 (b)). This was fitted with an exponential function with offset and the result of the fit was used as $E^{\mathrm{t6}}_{\mathrm{exp}}(n)$. The four outer columns were excluded from the fit to avoid influences of the drop in energy owing to the reconstruction algorithm. $E^{\mathrm{t6}}_{\mathrm{exp}}(n)$ was then put in Eqs. (6.2) and (6.3) instead of $E^{\epsilon}_{\mathrm{exp}}$. This had the general advantage that fluctuations in $E^{\epsilon}_{\mathrm{exp}}$ due to the energy resolution of the spectrometer were removed. The relation had to be used with caution, as it was obtained from the original calibration constants which were to be improved using the relation itself.

  This method has a better performance in the minimization; the mean of the pull distribution is reduced from 1.154 to 0.089. Nonetheless, the quality of the relative calibration as evaluated by the above discussed distributions (Figs. 6.5 to 6.9) could not be improved satisfactorily, either.

  Instead of using $E^{\mathrm{t6}}_{\mathrm{exp}}(n)$, the function $E_{\mathrm{exp}}(n)$, which is shown in Fig. 6.5 (b), could have been used. This would additionally have the advantage of being more independent of the original calibration as $E_{\mathrm{exp}}(n)$ was derived from the energies measured with the spectrometer. As the two function did not differ significantly in slope, no essential improvement in performance was expected.

- For the 3×3 reconstruction volume it was also tried not to use only the events having the hottest cell in row 1 but to include also the events having the hottest cell in row 2. In that way correction factors could also have been extracted for the cells in row 3. Yet by doing so the minimization did not return reasonable results; some factors, particularly in row 3, had negative values. The reason was probably that only 6% of the events covered row 3 with their reconstruction volume (comp. Fig. 6.10), consequently leading to only 6% of the summands in the χ^2 of Eq. (6.2) to include correction factors for the cells in row 3.

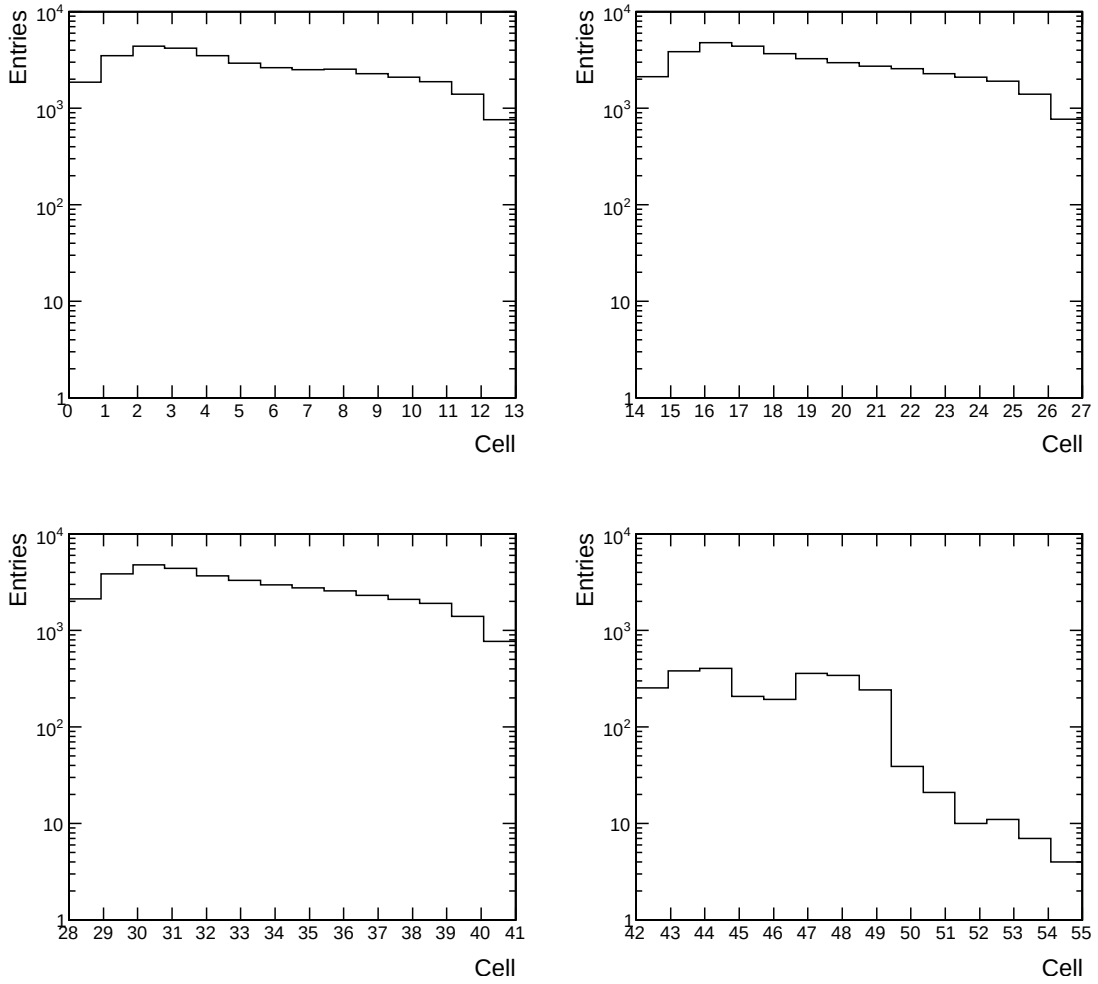

Figure 6.10: The number of times each cell, and therefore the correction factor of each cell, appeared in χ^2 of Eq. (6.2) when selecting events with the hottest cell in row 1 or 2.

- A different method was tried to handle the different positions of the reconstruction volume. An individual χ^2_n as in Eq. (6.2) was defined for each column n. Only events with the hottest cell in column n contributed to χ^2_n. Like before, events with the hottest cell in row 1 were considered. Thus the minimization of each χ^2_n lead to nine correction factors for the cells in the reconstruction volume centered around the corresponding hottest cell. As the volumes overlapped, three values for the correction factors of each cell were obtained from three different χ^2_n minimizations, as illustrated in Fig. 6.11. This did not hold

for the cells in the four columns located at the 6 m tagger edges. There was only one correction factor for cells in columns 0 and 13, and there were two for cells in columns 1 and 12.

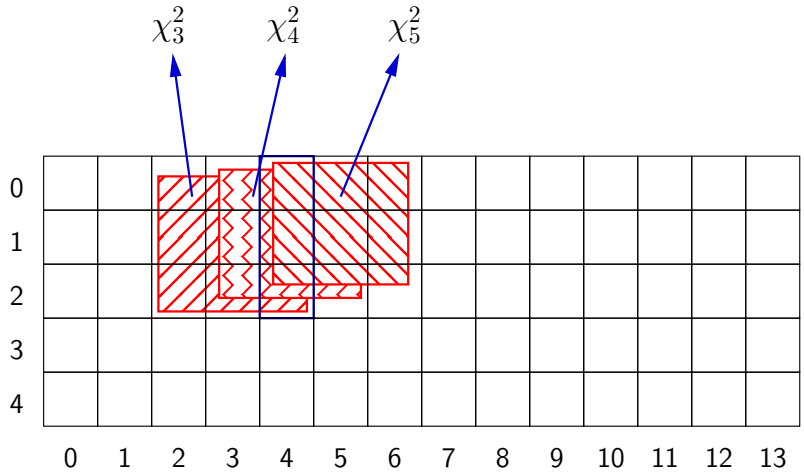

Figure 6.11: An alternative approach performed one separate χ^2 minimization for each column. Due to the overlap of the reconstruction volumes, three different correction factors were obtained for each central cell. This is illustrated for the cells of column 4: correction factors are obtained from the minimization of χ^2_3, χ^2_4, and χ^2_5.

The different correction factors for each cell should agree. However, the values obtained for the different factors featured large differences, and some of them were negative. When taking the mean values of the – up to three – factors determined for each cell the resulting values were usually close to one. The quality of the relative calibration was not improved.

- Instead of a 3×3 reconstruction volume, it was tried to use the four cells adjacent to the hottest cell which contained the most energy. This volume seemed to be too small to allow a reasonable energy reconstruction. The minimization did not return positive values for all the correction factors.

6.1.5 Conclusions

The presented studies demonstrated the feasibility of the use of a χ^2 minimization method for a partial improvement of the energy reconstruction as well as the absolute calibration of the 6 m tagger. However, some miscalibrations were not corrected using this method. None of the investigated procedures turned out to significantly improve the relative calibration of the cells within one column. They were consequently not further pursued.

6.2 Vertical and horizontal correction

Another approach was developed to improve the original calibration, which separated the correction procedure into a vertical and a horizontal correction.

The vertical correction took care of a correct relative calibration within one column by one correction factor c_k^v for each cell k. The factors were obtained using the expected relation between the ratios of energy in different cells and the columns derived from the transverse profile of the electromagnetic showers in the 6 m tagger. The total reconstructed energy was left unchanged, only the individual weights of the cells were changed.

The energy reconstruction was optimized applying the horizontal correction which compared the reconstructed energy with the energy expected from the spectrometer. Furthermore, the calibration was tuned for a 3×3 energy reconstruction volume. The horizontal correction introduced a second factor $c_{n(k)}^h$ for each cell k in column n. Thus the original calibration constants had to be multiplied by two factors to obtain the new constants:

$$c_k^{\text{new}} = c_{n(k)}^h c_k^v c_k^{\text{orig}} \qquad k \in \{0, 70\},\, n \in \{0, 13\}. \tag{6.4}$$

It was not possible to determine vertical correction factors for the outermost columns, 0 and 13, due to the event selection (Section 6.2.1.2). Also, the reconstructed energy in these columns was too low owing to the fact that the reconstruction volume lay partly outside the 6 m tagger (Section 4.6.1). Therefore the fiducial volume of the 6 m tagger was restricted to the inner columns 1 to 12. This is an improvement w.r.t. the previous situation where the fiducial volume was restricted to columns 2 to 11 due to the 5×5 reconstruction volume.

The figures shown in this Chapter were generated from the data of the LER period, if not stated otherwise. The results for the other run periods were similar.

6.2.1 Vertical correction

6.2.1.1 Technique of the vertical correction

The position of incidence of the electrons in Bethe-Heitler events were located within a narrow band orthogonal to the dipole field of the GG magnet owing to the angular distribution of the Bethe-Heitler process. The transverse profile of electromagnetic showers is smoothly dependent on the energy of the initial particle. Therefore, the ratio of the mean energies deposited in two different cells within the same column was expected to have a smooth dependence on the column as discussed in Section 4.6.2.

The energy deposition in the cells of the 6 m tagger was not exclusively determined by the transverse shower profile because of the non-zero incident angle of the electron. It was dictated by the projection of the three dimensional shower profile on the surface of the 6 m tagger. This is a convolution of the transverse and the

longitudinal shower profile, taking into account the incident angle. The relation between the aforementioned energy ratio and the column is weakly dependent on the longitudinal profile. This is due to the fact that the variation of the angle of incidence over the 6 m tagger volume is small. In this case the longitudinal profile is smoothly dependent on the energy. Therefore, the combined profile – and hence the resulting ratio of mean energies – is expected to have a smooth dependence on the energy. This assumption was used to obtain vertical correction factors.

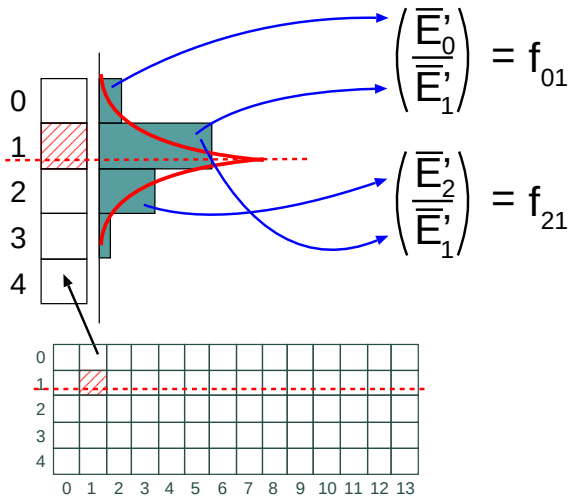

Figure 6.12: Demonstration of the vertical correction technique: The ratio $\bar{E}'_r/\bar{E}'_1$ of the mean of the corrected energies E'_r in a certain row r was required to be f_{r1}.

The vertical correction factor c_k^v for cell k was determined from events with the hottest cell in row 1 which were the majority as shown in Fig. 6.13. If E_k was the energy in cell k measured using the original calibration, the correction factors were required to ensure for the new energy $E'_k = c_k^v E_k$ (comp. Fig. 6.12):

I) the ratio $\bar{E}'_0/\bar{E}'_1$ of the mean energies of row 0 and row 1 to be f_{01};

II) the ratio $\bar{E}'_2/\bar{E}'_1$ of the mean energies of row 2 and row 1 to be f_{21};

III) the ratio $\bar{E}'_3/\bar{E}'_1$ of the mean energies of row 3 and row 1 to be f_{31};

IV) the sum of the mean energies in the cells of the first four rows to be the same before and after the correction, $\bar{E}'_0 + \bar{E}'_1 + \bar{E}'_2 + \bar{E}'_3 = \bar{E}_0 + \bar{E}_1 + \bar{E}_2 + \bar{E}_3$.

With

$$\alpha = \frac{\bar{E}_0 + \bar{E}_1 + \bar{E}_2 + \bar{E}_3}{f_{01} + 1 + f_{21} + f_{31}} \tag{6.5}$$

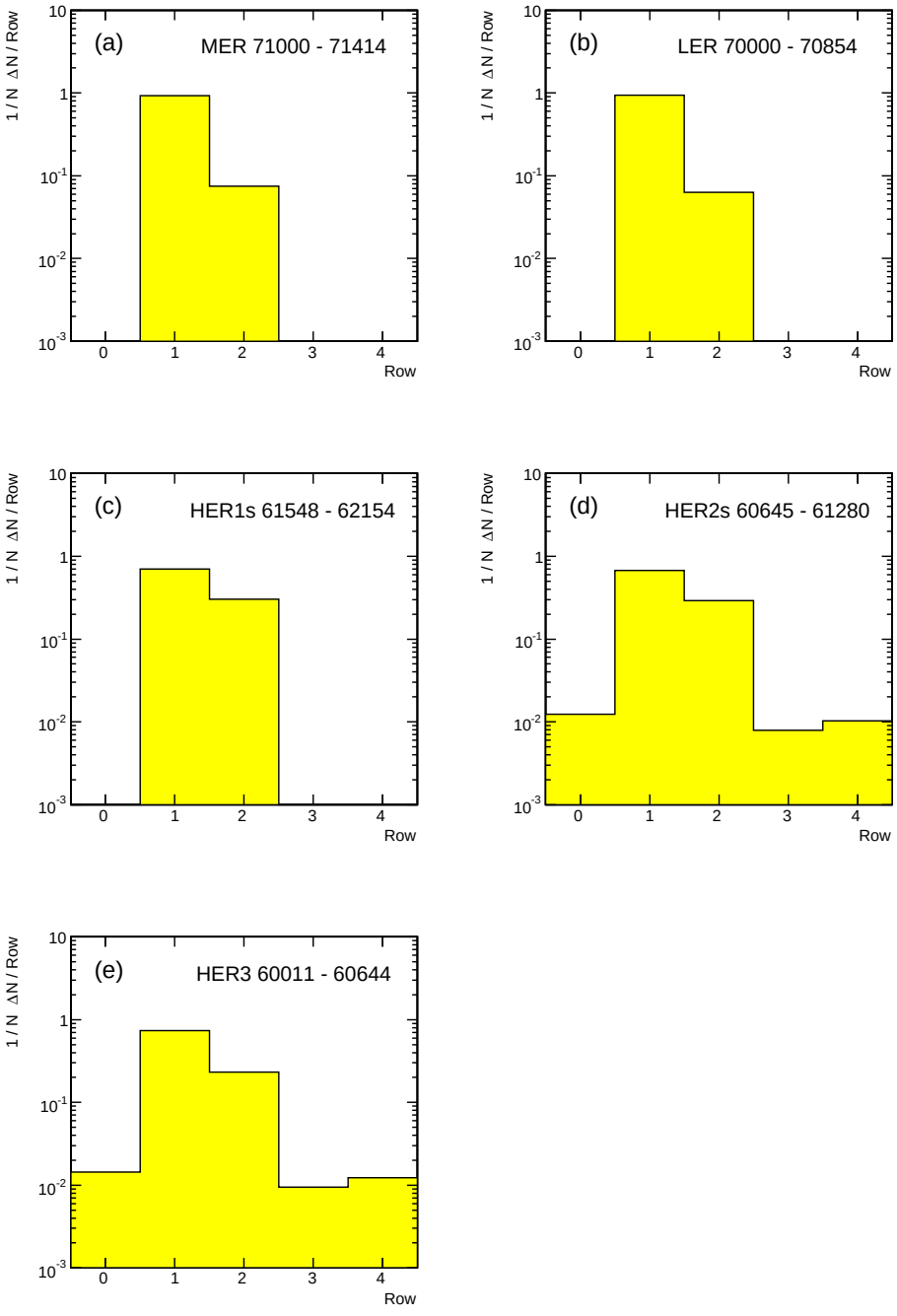

Figure 6.13: Fraction of events with the hottest cell in a certain row. The distributions are shown for the different run periods.

the vertical correction factors were therefore

$$\begin{aligned} c_0^v &= f_{01}\frac{\alpha}{\bar{E}_0} \\ c_1^v &= \frac{\alpha}{\bar{E}_1} \\ c_2^v &= f_{21}\frac{\alpha}{\bar{E}_2} \\ c_3^v &= f_{31}\frac{\alpha}{\bar{E}_3} \end{aligned} \tag{6.6}$$

The actual values of f were taken from the ratios of the mean energies obtained with the original calibration. Figure 6.14 shows the ratios of the mean energy in row 0, row 2, and row 3 over the mean energy in row 1, where the hottest cell was located, as a function of the column of the 6 m tagger for the LER period. The values feature fluctuations but depend approximately linearly on the column index n. This tendency is very pronounced for $\bar{E}_2/\bar{E}_1$ and $\bar{E}_3/\bar{E}_1$. There are larger fluctuations for $\bar{E}_0/\bar{E}_1$ which might be due to the influence of electronic noise. In general noise had a larger impact on the mean energies in row 0 and row 3 since the energies measured there were considerably lower than in row 1 and row 2, and comparable to the noise level. The linear dependencies of the measured ratios (Fig. 6.14) have different tendencies:

- $\bar{E}_0/\bar{E}_1$ has a positive slope, but the tendency is not very significant due to the large fluctuations observed;
- $\bar{E}_2/\bar{E}_1$ and $\bar{E}_3/\bar{E}_1$ have negative slopes.

Several effects contribute to these slopes, like for example the dependence of the combined transverse and longitudinal shower profile on the energy. This behavior could also have been caused by a displacement of the electron position of incidence in the positive y direction, as illustrated in Fig. 6.15. The reason for this shift might be that the 6 m tagger was not mounted exactly parallel to the plane orthogonal to the magnetic dipole field.

Random miscalibration causing the observed column dependency of the ratios appeared unlikely. A possible systematic miscalibration due to radiation damage of the fibers was investigated. The damage was constantly monitored during the running period by cobalt scans of the apparatus [16]. The damage was measured by comparing the signal in the 6 m tagger generated by a radioactive `Co` source with the signal from a reference measurement, leading to a relative signal strength s. s was 1 in case of no damage and 0 in case of total damage. If a certain true energy, E_{true}, was deposited in a cell of the row r, the damage reduced the registered energy to $E_r^{\text{raw}} = s_r E_r^{\text{true}}$. The original calibration constant c, which is the same for all the cells within the same column, led to a corrected measured energy $E_r^{\text{meas}} = cE_r^{\text{raw}}$.

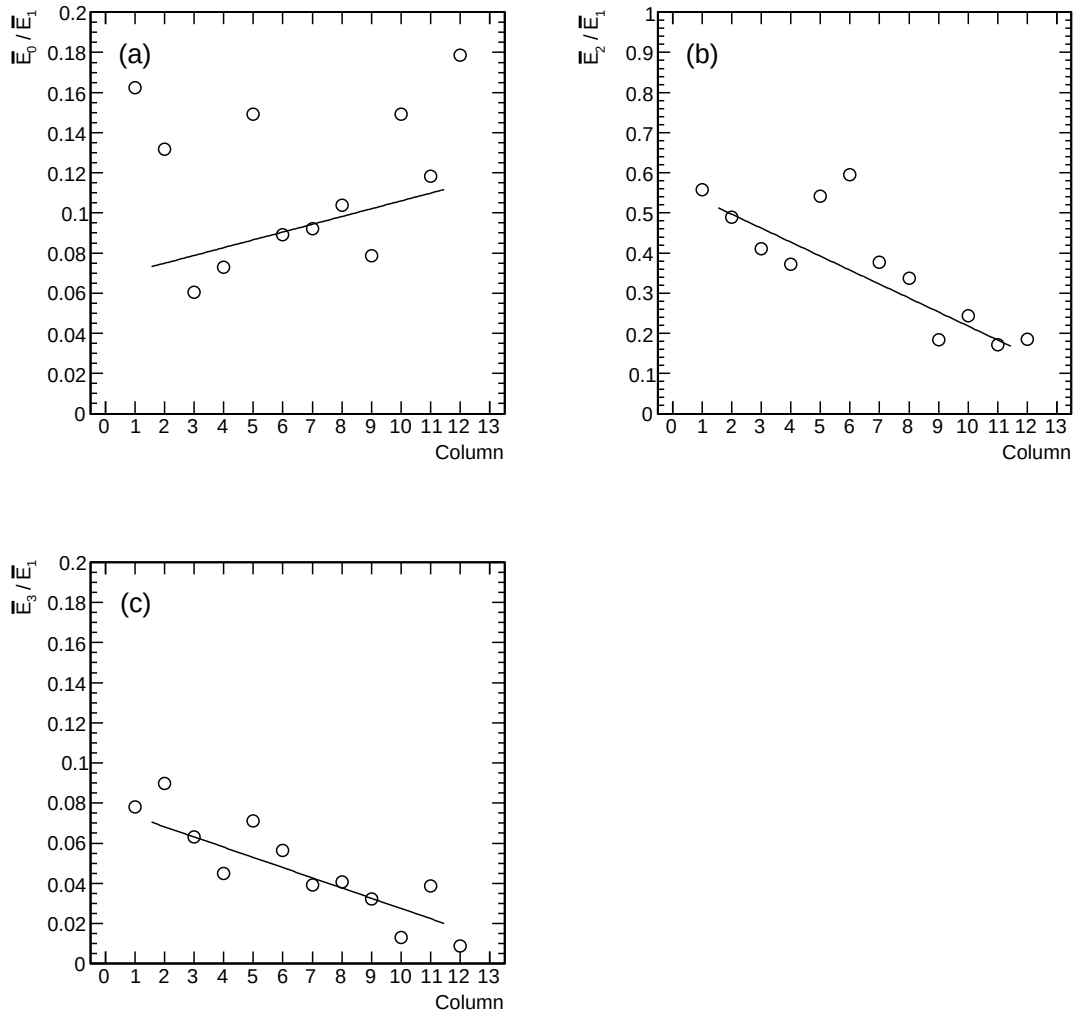

Figure 6.14: Ratios between the mean energy in (a) row 0, (b) row 2, and (c) row 3 and the mean energy in row 1 (where the maximum energy is deposited) from the original calibration as a function of the column index n for the LER period. No ratios were obtained for columns 0 and 13 owing to the event selection (Section 6.2.1.2). Linear fits from column 2 to 11, where the full energy was reconstructed, are superimposed. Note that the errors on the mean values (standard deviation) are smaller than the marker points.

Therefore the relation between the ratio of true energies in row A and B and the

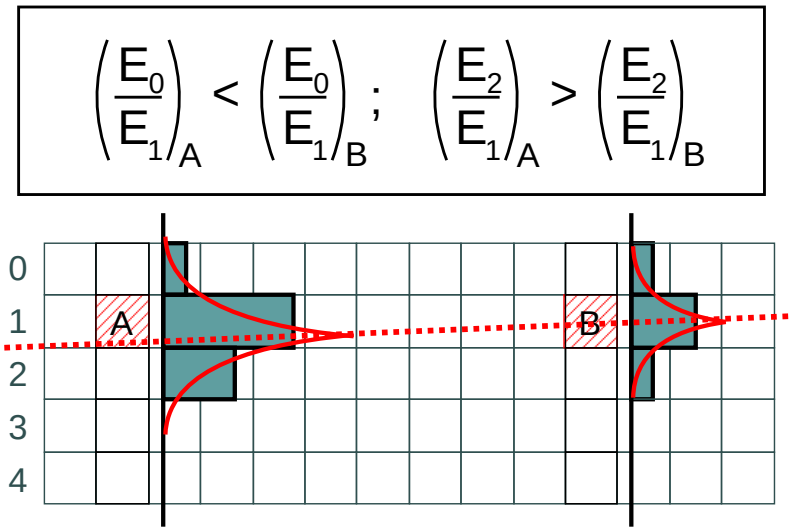

Figure 6.15: Effect of a vertical shift of the position of incidence of the electron on the ratios of energy in different columns of the 6 m tagger.

ratio of measured energies is

$$\left(\frac{E_A}{E_B}\right)_{\text{meas}} = \frac{s_A}{s_B}\left(\frac{E_A}{E_B}\right)_{\text{true}}, \tag{6.7}$$

and thus dependent on the ratio of the relative signals in row A and B.

The fraction s_2/s_1 of the relative signals in row 2 and row 1 is shown in Fig. 6.16. Three measurements done at different times are shown. The value is smaller than 1 for small column indices and approaches 1 when going to larger column indices. As follows from Eq. (6.7), this behavior of the relative signals would cause the fraction $\bar{E}_2/\bar{E}_1$ to rise with the column number – opposite from what was measured.

To summarize, it was concluded that the measured dependence of the ratio f of mean energies on the column is compatible with an increase of the incident y position of the electron with increasing x. This can be attributed to a tilt of the 6 m tagger w.r.t. to the plane of incidence perpendicular to the magnetic dipole field of the GG system. The tendencies in f were weakened owing to radiation damages.

In consequence, f was parameterized as a linear function of the column index n with parameters obtained from a linear fit. The energy reconstruction in the original calibration scheme was insufficient in the the two outer columns on each side of the 6 m tagger owing to the 5×5 reconstruction volume. Thus, only the inner columns 2 to 11 were included in the fit (Fig. 6.14). Table B.2 in Appendix B lists the functions returned from the linear fits.

Using these values for f, a set of vertical correction factors $c_k^{v,0}$, $k \in \{0, 69\}$, was calculated using Eq. (6.6). The 6 m tagger was calibrated by multiplying the original

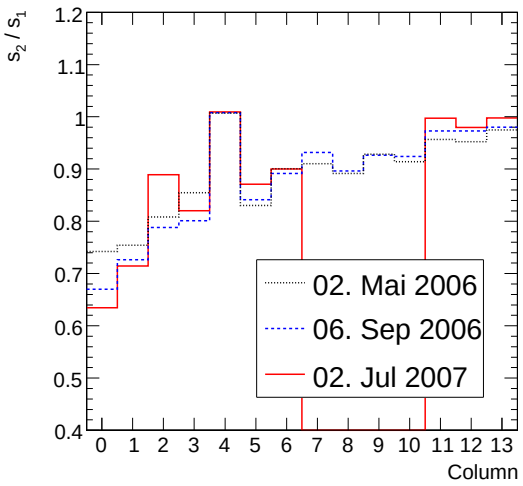

Figure 6.16: Fraction of the relative signal s in row 2 and row 1. s is the signal measured in the Co-Scan at the given dates relative to the second Co-Scan on Mai 6, 2004 [16].

calibration constants with these correction factors, resulting in the new calibration constants $c_k^{\text{new},0}$. This procedure was iterated several times. Each time a new correction was obtained to apply on top of the previous one:

$$\begin{aligned} c_k^{\text{new},0} &= c_k^{v,0} \cdot c_k^{\text{orig}} \\ c_k^{\text{new},1} &= c_k^{v,1} \cdot c_k^{v,0} \cdot c_k^{\text{orig}} \\ &\dots \end{aligned} \tag{6.8}$$

The need for an iteration procedure came from the fact that the dependence of f on the column was in each case extracted using the existing calibration. Figure 6.17 shows the convergence of the iteration procedure for $\bar{E}_2/\bar{E}_1$ as an example. In total, three or four steps were done depending on how well the actual ratios f and the fit agreed (Table B.2 in Appendix B).

Choosing f using the original calibration is obviously somewhat arbitrary. If in fact the original relative calibration was wrong, the parameterization of f would inherit this miscalibration and lead to a wrong correction. The correction procedure does therefore not necessarily result in a calibration providing the true relative energies. Instead, as the cells were re-weighted according to an assumed shower profile and some assumed tilt of the 6 m tagger, just a consistent overall behavior can be expected. This is nonetheless an improvement. If an electron hits the 6 m tagger at a different y position than the electrons coming from Bethe-Heitler events (like electrons from photoproduction events for instance) the energy should be reconstructed

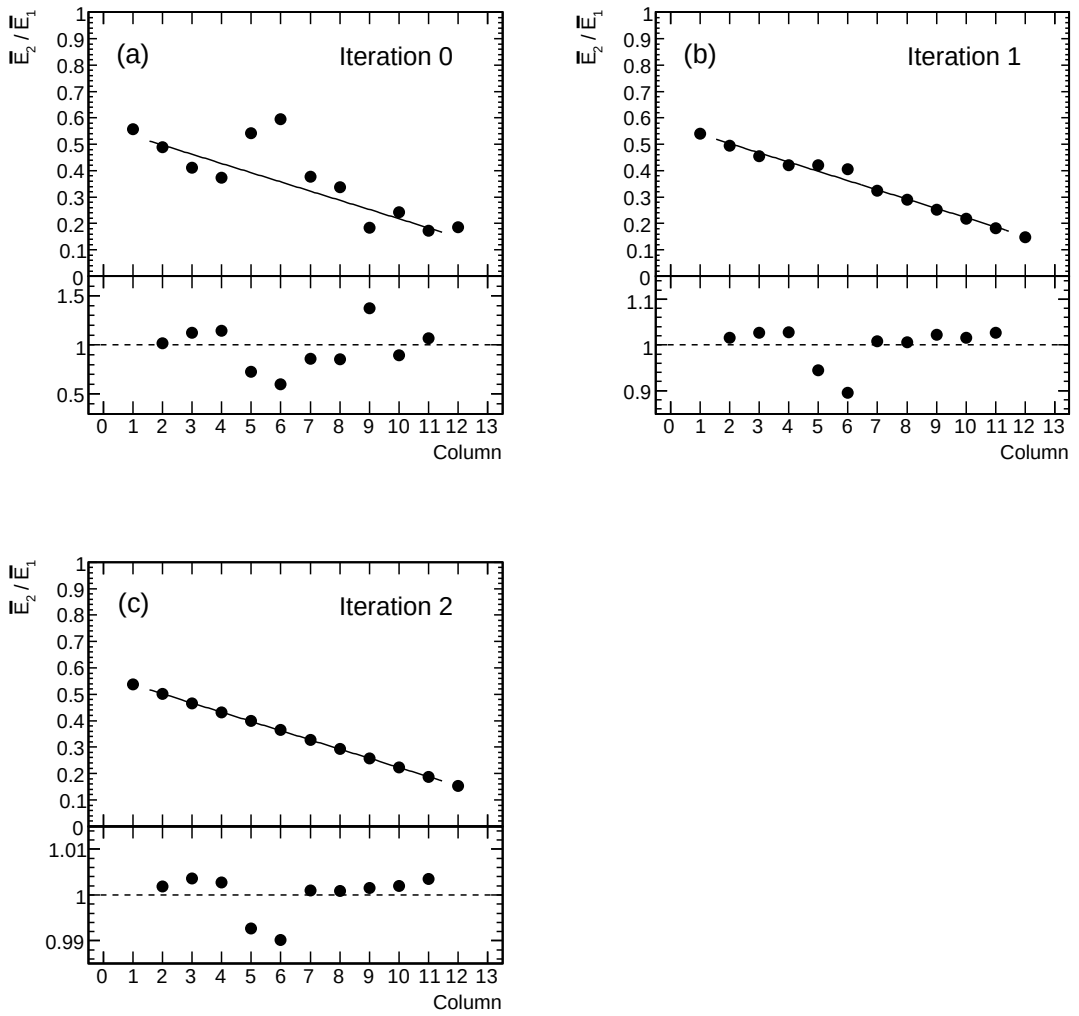

Figure 6.17: Comparison of the ratio $\bar{E}_2/\bar{E}_1$ after the different iterations (LER period). No ratios were obtained for columns 0 and 13 owing to the event selection (Section 6.2.1.2). Linear fits from column 2 to 11, where the full energy was reconstructed, are superimposed. They were used as input to Eq. (6.6) for the following iteration. Note that the errors on the mean values (standard deviation) are smaller than the marker points. The ratio between value predicted by the fit and the measured ratio is plotted in the bottom part of the histograms.

correctly. This is not the case in the original calibration scheme because the relative calibration is inconsistent and the energy reconstruction was tuned for Bethe-Heitler

events, which have a constant y position.

6.2.1.2 Event selection for the vertical correction

Bethe-Heitler events were selected as described in Section 5.5. As mentioned above, the events were selected which had in addition

7. the hottest cell in row 1.

It was furthermore required that the x position of the shower maximum was in the center of the column containing the hottest cell. This assured that most of the shower energy was deposited in that column and thus that the energy fraction was not distorted by the non-central part of the shower profile. The position of the shower maximum inside a column was evaluated as an energy weighted mean of the column index within the 3×3 reconstruction volume: by the mean of the column index weighted linearly with the energy:

$$\xi = \frac{\sum_{m=-1}^{1} m E^m_{\text{sum3}}}{\sum_{m=-1}^{1} E^m_{\text{sum3}}}.$$

Here m is the column index, with $m = 0$ being the column containing the hottest cell. E^m_{sum3} is the energy in column m of a 3×3 volume centered around the hottest cell (comp. Fig. 6.18).

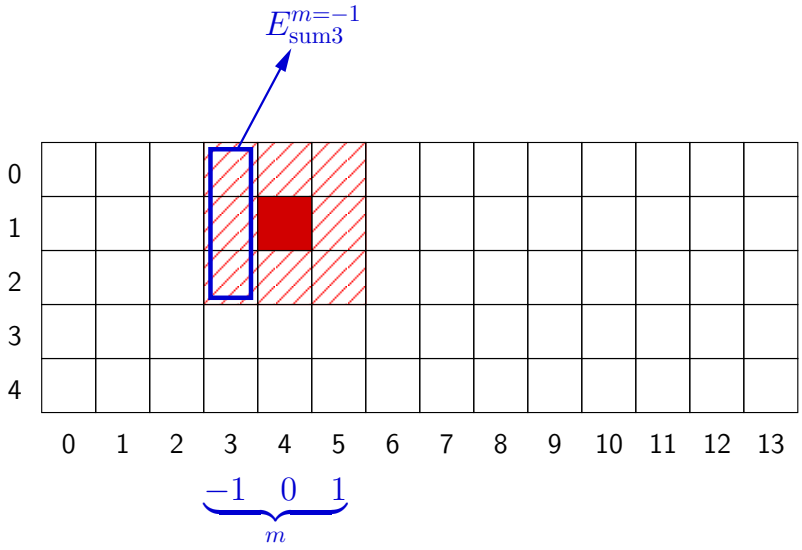

Figure 6.18: Determination of E^m_{sum3} which was used to calculate the shower position with a column, $\xi = (\sum_{m=-1}^{1} m E_{\text{sum3}}(m))/(\sum_{m=-1}^{1} E_{\text{sum3}}(m))$.

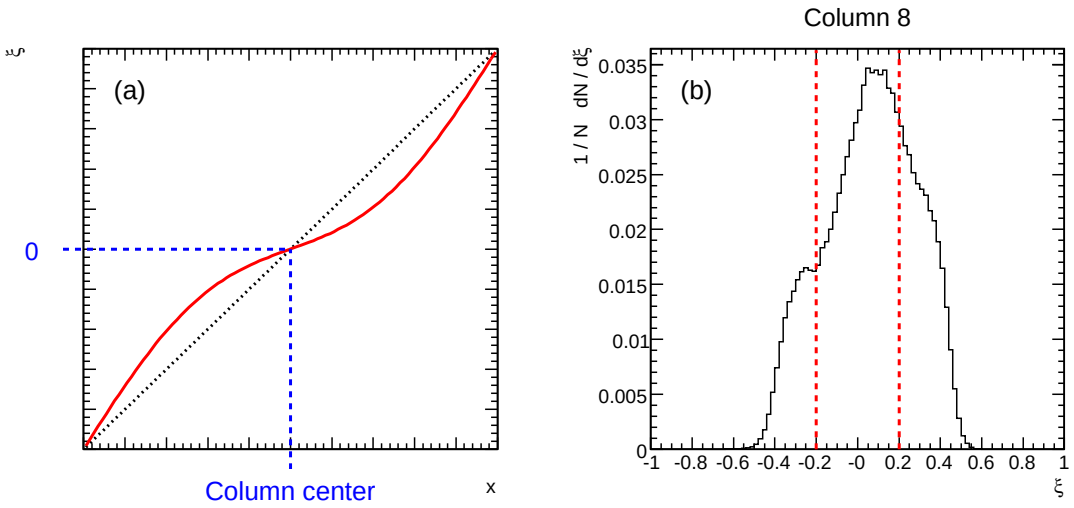

Figure 6.19: (a) Illustration of the non-linear relation between ξ and x. An x position of the column center corresponds to $\xi = 0$. (b) A typical ξ distribution. The shape of the distribution is not understood. The dashed lines indicate the cut on $|\xi|$.

ξ is therefore related to the x position of the shower maximum, such that $\xi = 0$ corresponds to the column center and $\xi > 0$ to a shower position at the right-hand side of the cell center and vice versa. This non-linear relation between ξ and x is illustrated in Fig. 6.19 (a); a typical ξ distribution is shown in Fig. 6.19 (b). To be able to calculate ξ for all the events, those events with the hottest cell in column 0 or 13 had to be rejected:

8. the hottest cell was required to be in column 1 to 12.

Therefore no correction factors could be obtained for the cells in column 0 and 13. To select only central events it was demanded that:

9. $|\xi| < 0.2$.

6.2.1.3 Results of the vertical correction

The vertical correction factors for the LER period at the three different steps of the iteration are shown in Fig. 6.20. The factors obtained in each step were a correction to the factors from the previous step, as stated in Eq. (6.8). As the values approach 1 in a few steps, the procedure is shown to converge quickly. The deviations from 1 are less than 1% – in most cells less than 0.5% – after the third step. No correction factors could be obtained for the cells in column 0 and 13 owing to the event selection

(Section 6.2.1.2). The final correction factors, which are the product of the factors extracted from the three iterations and which are directly used as multiplicative corrections to the original calibration constants, are presented in Fig. 6.21. In row 0 and 3, where little energy was deposited and noise had a larger relative impact, the factors fluctuate more than in the inner rows.

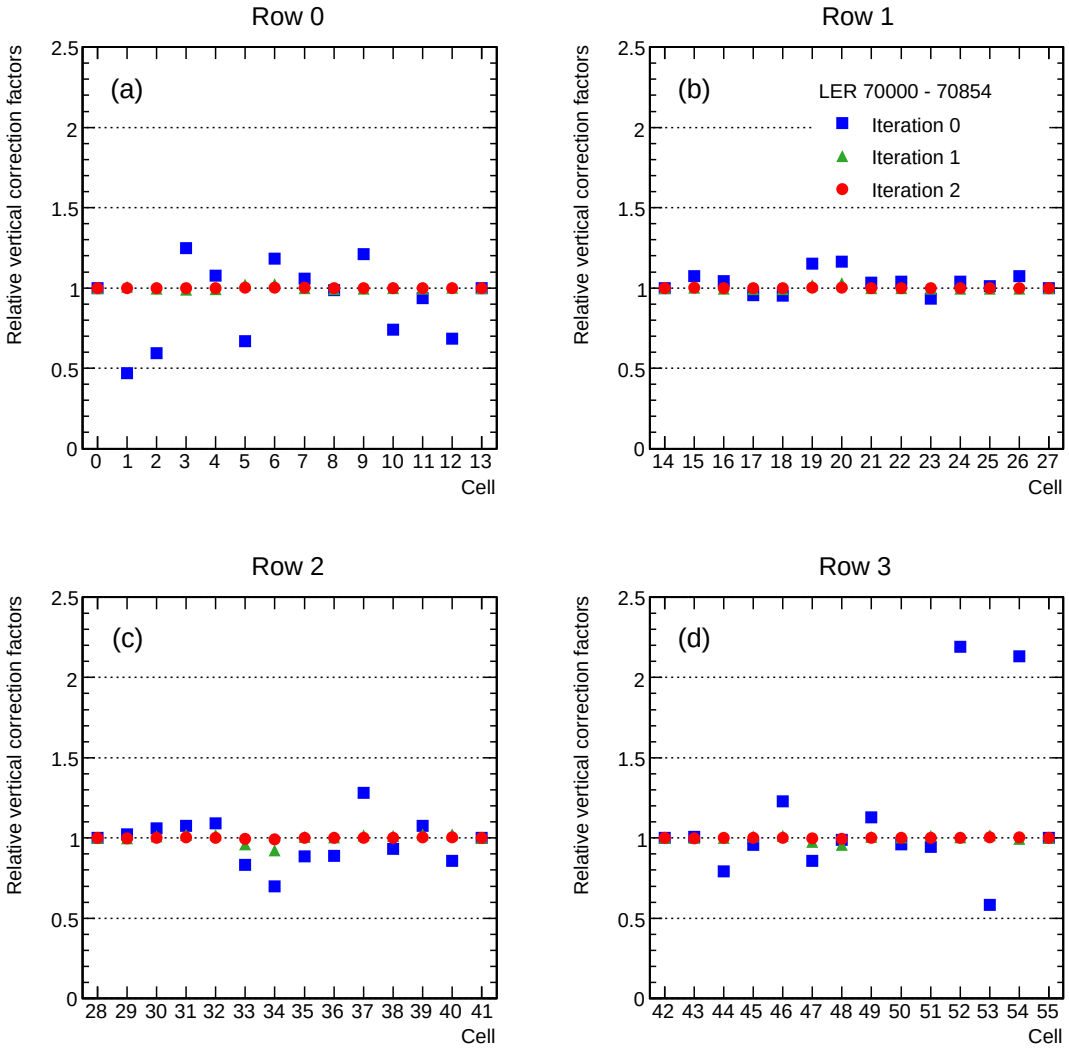

Figure 6.20: Vertical correction factors for the LER period. The factors are shown at the different steps of the iteration. Note that no correction factors could be obtained for columns 0 and 13 due to the event selection.

It is interesting to look at the correction factors in the cells of column 5 and 6. They are significantly larger than the average in row 1 and lower in row 2. This

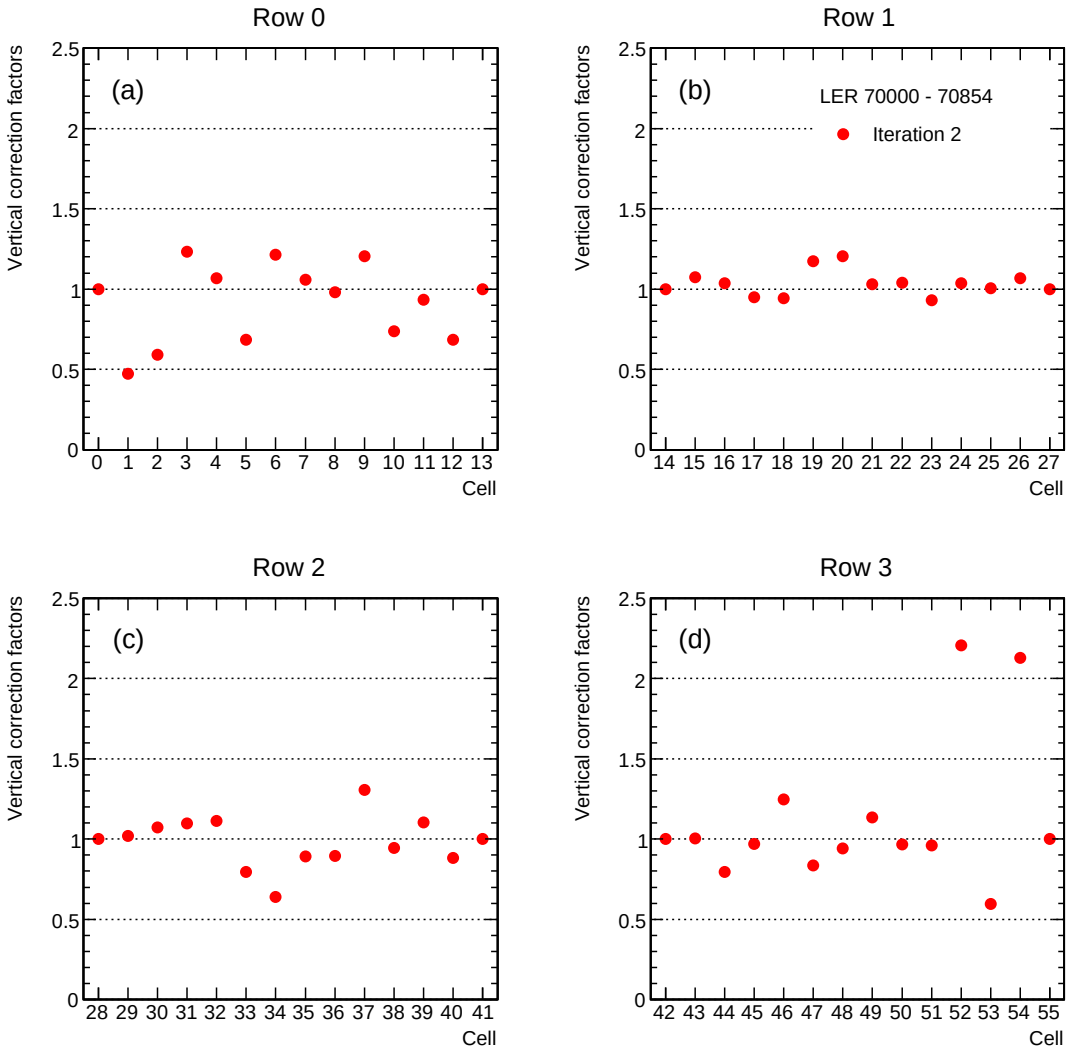

Figure 6.21: Vertical correction factors for the LER period. The multiplicative correction factors to be applied to the original calibration constants to obtain the new calibration are shown.

corrects the miscalibration in those columns which is evident by looking at the number of events per column, as discussed in Section 4.6.2. Figure 6.22 shows the distribution of the number of events within row 1 and 2. It was computed first with the original calibration constants and for comparison after the vertical correction factors were applied. For the original calibration the behavior is not smooth and points to effects of miscalibration especially in columns 5 and 6. The values are closer to the expected ones after the correction factors were applied, while some

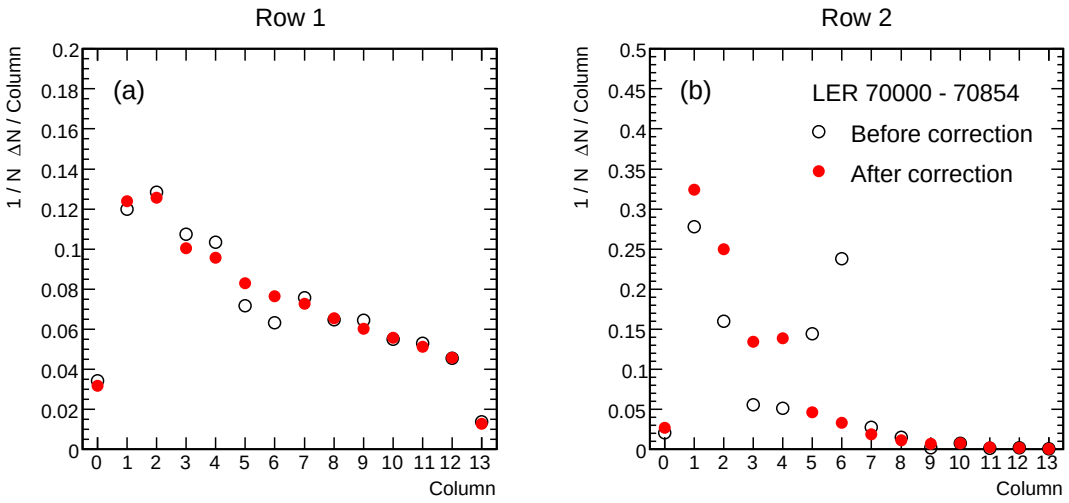

Figure 6.22: Number of events with the hottest cell in a particular column. The distribution obtained using the original calibration is compared to that obtained after the vertical correction factors have been applied. (a) Hottest cell in row 1, (b) hottest cell in row 2.

smaller miscalibration remain in column 3 and 4. The slope in the rows is different, it is much larger in row 2. The reason for this is that the y position of the incident electron moved upward for larger x, as discussed previously. Therefore $\mathrm{d}N/\mathrm{d}y$ is not constant but depends on x i.e. the fraction of events in row 1 gets larger with larger x. The slope of $\mathrm{d}N/\mathrm{d}x$ as coming from the Bethe-Heitler cross section and the electron kinematics has to be convoluted with this $\mathrm{d}N/\mathrm{d}y(x)$ relation.

6.2.1.4 Consistency tests of the vertical correction

Some tests were made to estimate the consistency and stability of the vertical correction procedure.

As mentioned in Section 4.7, the correction was meant to cure systematic miscalibration averaged over a longer run period. The relative differences between the correction factors obtained using the events of a short run range (70100 to 70199) and the factors from the longer LER period are shown in Fig. 6.23. They are, except for the constants of row 3, smaller than 5%. Larger fluctuations occur mostly in cells at the right hand-side of the 6 m tagger where energies and statistics were low and thus fluctuations due to noise and statistics had a larger effect.

The dependence of the vertical correction on the choice of taking events with the hottest cell in row 1 was investigated. Correction factors were calculated using only events with the maximum in row 2. The number of events selected in this way was

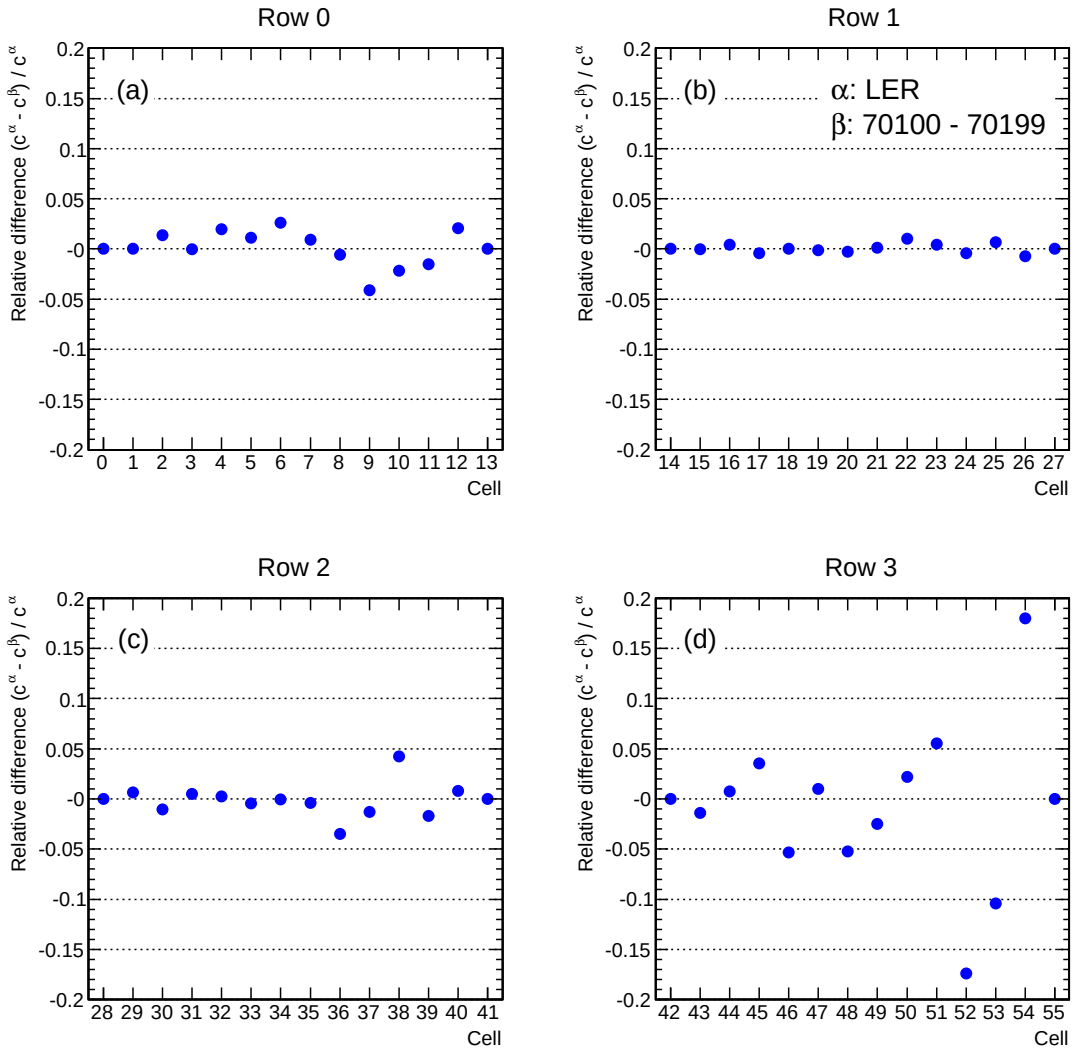

Figure 6.23: Relative difference $(c^\alpha - c^\beta)/c^\alpha$ between the vertical correction factors c^α and c^β for two different LER periods α and β, respectively.

very low, especially in the columns with larger indices, as shown in Fig. 6.22 (b). As a consequence, the error on the ratio of the mean energies increased (Fig. 6.25). Hence, the fits to estimate f were done from column 2 to 7 and the correction factors were evaluated for the same region.

Figure 6.24 shows the relative difference between the correction factors obtained using events with a maximum in row 1 and those with a maximum in row 2. They differ largely in row 0 and up to 20% in the other rows, especially in columns 5 and 6. The factors obtained from events in row 2 rose the calibration in row 0 in

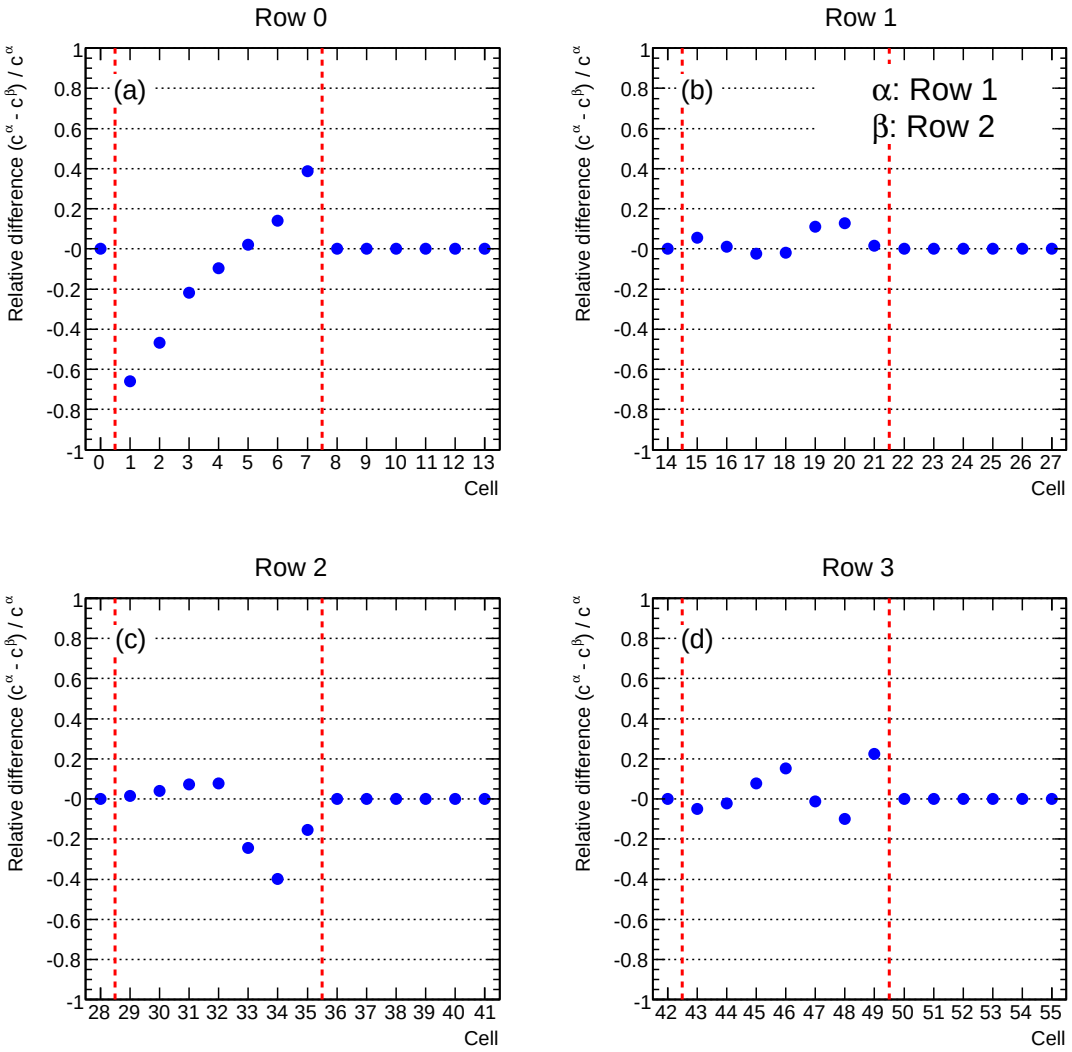

Figure 6.24: Relative difference $(c^\alpha - c^\beta)/c^\alpha$ between the vertical correction factors c^α and c^β obtained using the events with the maximum in row 1 and the maximum in row 2, respectively. Correction factors were only calculated for columns 1 to 7 due to low statistics in the columns further to the right.

the columns close to the beampipe i.e. they caused a different relative calibration.

The 6 m tagger was expected to show a consistent relative calibration of the cells within one column when the vertical correction obtained from events with the maximum in row 1 was applied. If the correction procedure was then repeated for events with the maximum in row 2, the factors obtained were expected to be 1. The de-

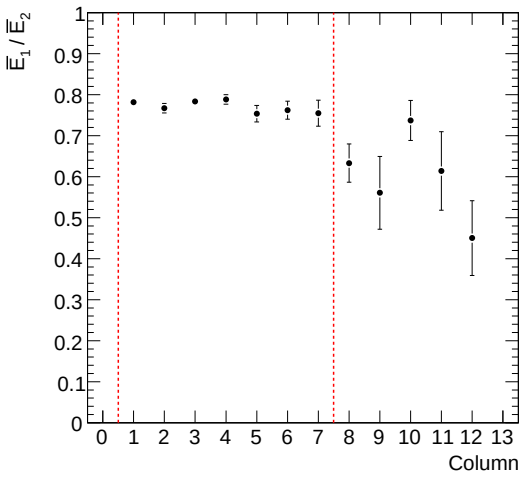

Figure 6.25: Ratio $\bar{E}_1/\bar{E}_2$ of the mean energies in row 1 and row 2 as a function of the column for events with the hottest cell in row 2.

viations of these second correction factors from 1 are shown in Fig. 6.26. They are smaller than 5% in all but two cells located in row 0 and row 3 where noise effects are dominant.

This is owing to the aforementioned aspect, that the vertical correction did not necessarily produce the correct but just a consistent relative calibration. Choosing different sets of events which might have a different original relative calibration to calculate correction factors (for instance those in row 1 and those in row 2) produces different but self-consistent results.

As the vast majority of the events was located in row 1 it appeared reasonable to use the correction factors obtained with these events for further study.

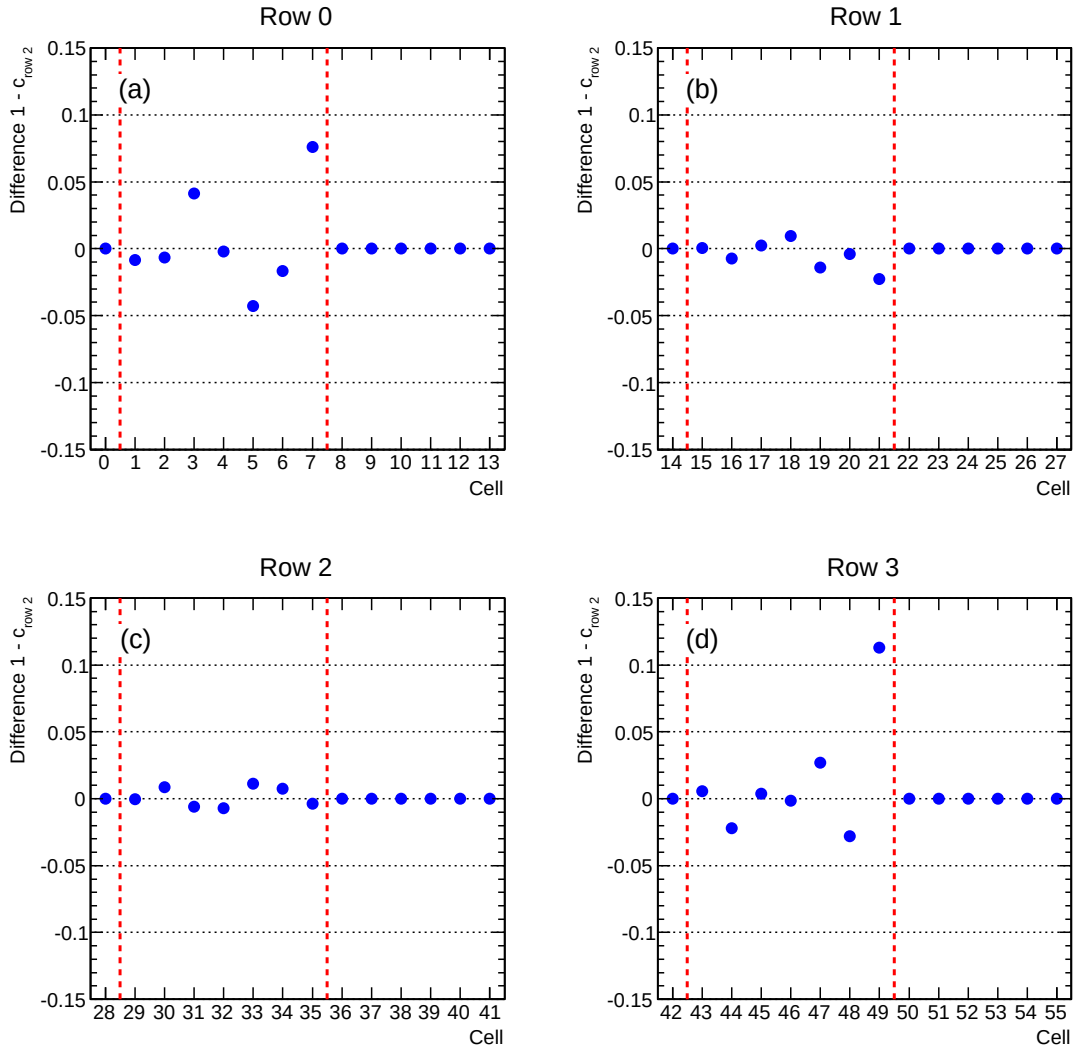

Figure 6.26: Difference $1 - c_{\text{row }2}$ of the vertical correction factors $c_{\text{row }2}$ obtained using the events with the maximum in row 2. The correction from events with the maximum in row 1 was applied before calculating the factors $c_{\text{row }2}$. Correction factors were only calculated for columns 1 to 7 due to low statistics in the columns further to the right.

6.2.2 Horizontal correction

6.2.2.1 Technique of the horizontal correction

The horizontal correction was performed after having applied the vertical correction factors. It was based on the the energy, E_{spec}, of the Bethe-Heitler photon measured by the spectrometer and on the original calibration of the 6 m tagger. E_{spec}

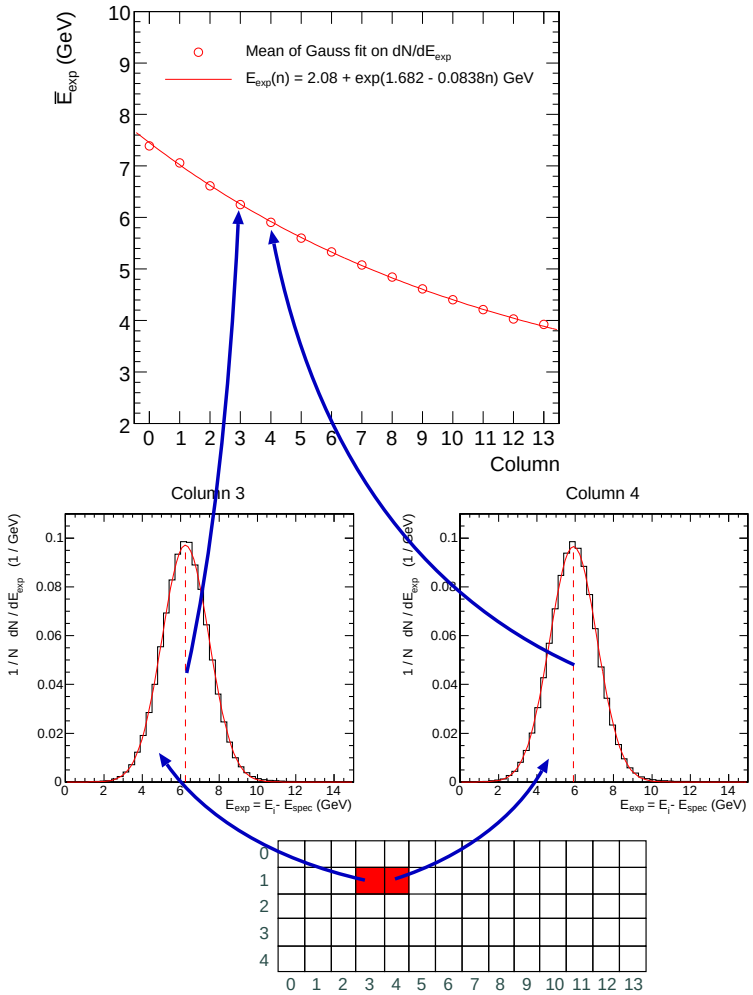

Figure 6.27: Mean energies per column of the 6 m tagger as expected from the spectrometer. The values are the mean values of Gaussian fits to the distributions of $E_i - E_{\mathrm{spec}}$ in each column n. The solid line in the top plot is a fitted relation $E_{\mathrm{exp}}(n)$.

was used to obtain a relation between the expected electron energy, E_{exp}, and the

column containing the hottest cell, used as an approximation for the x position of the incident electron. If the initial electron at the vertex had an energy E_i and if ignoring radiative effects, one expects the electron hitting the 6 m tagger to have an energy

$$E_{\text{exp}} = E_i - E_{\text{spec}}. \tag{6.9}$$

E_i was assumed to be equal to the nominal electron beam energy. The beam energies for all run periods are given in Table B.5 in Appendix B.

For each column, a histogram was filled with the expected energies of the events having the hottest cell in that column. This is illustrated in the bottom part of Fig. 6.27. Each distribution was fitted with a Gaussian and its mean value was taken to be the expected energy in the corresponding column (top part of Fig. 6.27). The error from the fit was taken to be the error on the mean energy. The mean energies per column n were fitted with an exponential function with an offset:

$$E_{\text{exp}}(n) = p_0 + e^{p_1 + p_2 n}. \tag{6.10}$$

The values of the parameters returned from the fits for all run periods are listed in Table B.3 in Appendix B.

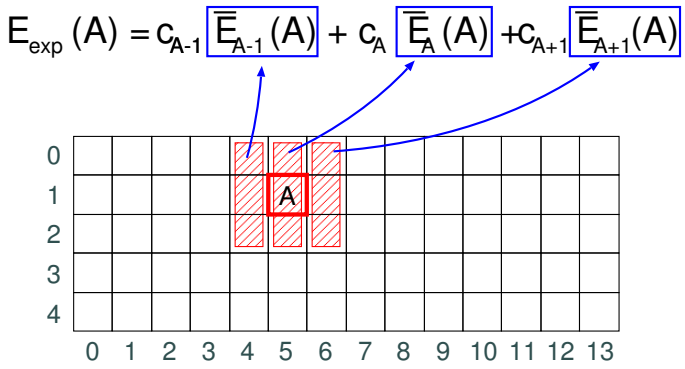

Figure 6.28: Determination of the equations used to calculate the horizontal correction factors for central columns.

To obtain the horizontal correction factors, the events were sorted by the column containing the hottest cell. For each column, the mean energies of the three columns belonging to the corresponding reconstruction volume were calculated, as illustrated in Fig. 6.28. For example, if the hottest cell was in column A, the reconstruction volume consisted in the standard case of three columns, $A-1$, A, and $A+1$, each containing three cells. They contained the energies $E_{A-1}(A)$, $E_A(A)$, and $E_{A+1}(A)$. Correction factors c^h for each column were obtained by requiring:

$$E_{\text{exp}}(A) = c^h_{A-1}\bar{E}_{A-1}(A) + c^h_A\bar{E}_A(A) + c^h_{A+1}\bar{E}_{A+1}(A). \tag{6.11}$$

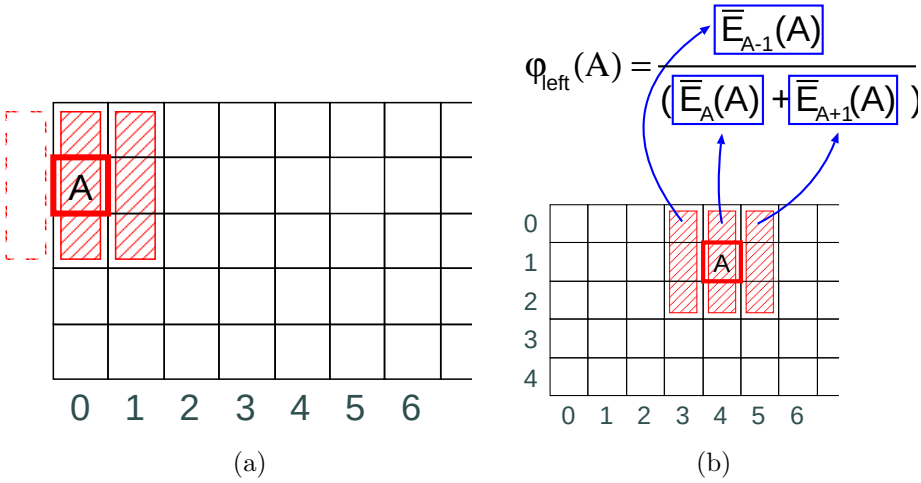

Figure 6.29: (a) The reconstruction volume exceeds the 6 m tagger edges for events having the hottest cell in column 0. (b) Illustration of the definition of φ_{left}, which estimates the fraction of energy deposited in the left column of the reconstruction volume.

If the hottest cell was in column 0 or 13, the 3×3 reconstruction volume exceeded the volume of the 6 m tagger and therefore the reconstructed energy was too small (comp. Fig. 6.29(a)). Equation (6.11) had to be modified to account for this. The quantity φ_{left},

$$\varphi_{\text{left}}(A) = \frac{\bar{E}_{A-1}(A)}{\bar{E}_A(A) + \bar{E}_{A+1}(A)},$$

was defined for events with the maximum in a central column A to estimate the amount of energy deposited in the left column of the reconstruction volume relative to the energy in the other two columns. This is illustrated in Fig. 6.29(b). The quantity φ_{right} described analogue the energy in the right column of the reconstruction volume.

Figure 6.30 shows the mean values, $\bar{\varphi}_{\text{left}}(n)$ and $\bar{\varphi}_{\text{right}}(n)$, in the LER period as a function of the different columns n. As they agreed quite well for columns 2 to 11, which was the region where the original 5×5 reconstruction scheme worked best, their mean values in this region, $\bar{\varphi}_{\text{left}}$ and $\bar{\varphi}_{\text{right}}$, were used in the following. The mean values were obtained by fitting the plots in Fig. 6.30 with a horizontal line. The asymmetry of the two values is probably owing to the incident angle of the electron which could have caused the asymmetric shower profile in Fig. 4.16 (a). Table B.4 in Appendix B lists the values of $\bar{\varphi}_{\text{left}}$ and $\bar{\varphi}_{\text{right}}$ for the different run periods.

Assuming that $\bar{\varphi}_{\text{left}}(0)$ was the same as $\bar{\varphi}_{\text{left}}$, which was a reasonable assumption due to the weak dependence of the transverse profile of an electromagnetic shower on the energy (Section 2.1) and due to the results shown in Fig. 6.30, it was possible

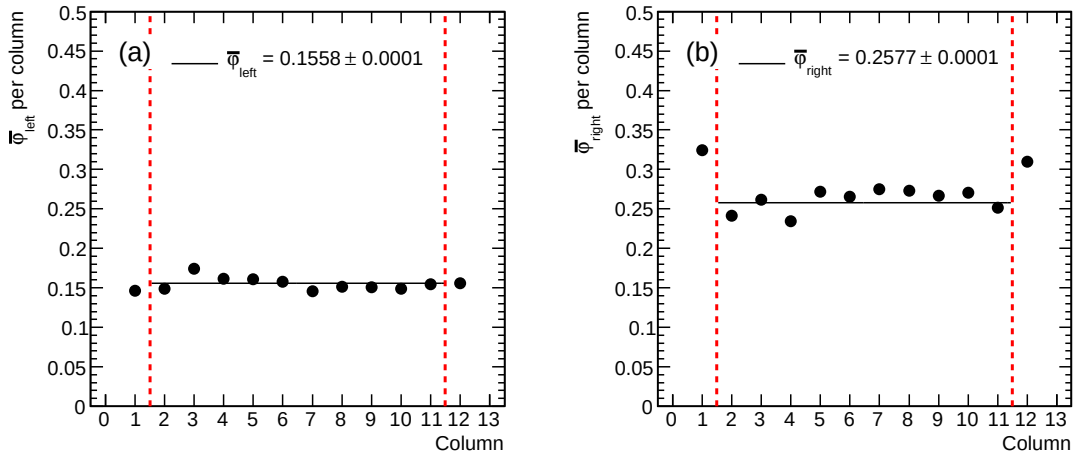

Figure 6.30: Mean values of $\varphi_{\text{left}}(n)$ and $\varphi_{\text{right}}(n)$ in the different columns n for the LER period. Note that the error bars (standard deviation) are smaller than the markers. The values from column 2 to 11 were used to calculate the overall mean values $\bar{\varphi}_{\text{left}}$ and $\bar{\varphi}_{\text{right}}$ using a horizontal fit.

to modify Eq. (6.11) for events having the hottest cell in column 0:

$$E_{\text{exp}}(0) = (1 + \bar{\varphi}_{\text{left}})(c_0^h \bar{E}_0(0) + c_1^h \bar{E}_1(1)).$$

The factor $(1+\bar{\varphi}_{\text{left}})$ compensated for the missing energy in the column not included in the 6 m tagger volume (Fig. 6.31). An analogue equation could be set up for column 13 using $\bar{\varphi}_{\text{right}}$ and assuming it to be equal to $\bar{\varphi}_{\text{right}}(13)$.

A system of 14 linear equations was built to evaluate the 14 horizontal correction factors $c^h_{n(k)}$, $n \in \{0, 14\}$, $k \in \{0, 69\}$:

$$\begin{aligned}
E_{\text{exp}}(0) &= (1 + \bar{\varphi}_{\text{left}})(c_0^h \bar{E}_0(0) + c_1^h \bar{E}_1(0)) \\
E_{\text{exp}}(1) &= c_0^h \bar{E}_0(1) + c_1^h \bar{E}_1(1) + c_2^h \bar{E}_2(1) \\
&\dots \\
E_{\text{exp}}(l) &= c_{l-1}^h \bar{E}_{l-1}(l) + c_l^h \bar{E}_l(l) + c_{l+1}^h \bar{E}_{l+1}(l) \\
&\dots \\
E_{\text{exp}}(13) &= (1 + \bar{\varphi}_{\text{right}})(c_{12}^h \bar{E}_{12}(13) + c_{13}^h \bar{E}_{13}(13))
\end{aligned} \tag{6.12}$$

The 6 m tagger was calibrated by multiplying these correction factors with the vertical correction factors and the original calibration constants, resulting in the

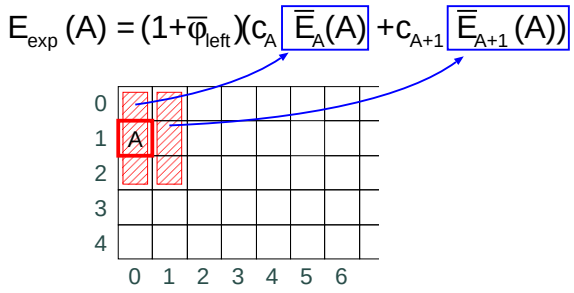

Figure 6.31: Determination of the equation used to calculate the horizontal correction factors for events in column 0. The factor $(1 + \bar{\varphi}_{\text{left}})$ compensated for the missing energy in the column not included in the 6 m tagger volume.

new calibration constants c_k^{new}. This procedure was iterated twice to obtain another correction on top of the first correction:

$$\begin{aligned} c_k^{\text{new},0} &= c_{n(k)}^{h,0} \cdot c_k^v \cdot c_k^{\text{orig}} \\ c_k^{\text{new},1} &= c_{n(k)}^{h,1} \cdot c_{n(k)}^{h,0} \cdot c_k^v \cdot c_k^{\text{orig}} \\ &\dots \end{aligned} \tag{6.13}$$

This was done in particular to account for changes in the values of $\bar{\varphi}$ when switching from a 5×5 to a 3×3 reconstruction volume. Moreover, owing to the aimed at improved calibration in the outer columns the selected events in these columns could change and thus affect the value of the mean energies measured in the cells of these columns.

6.2.2.2 Event selection for the horizontal correction

The selection of Bethe-Heitler events followed the details given before in Section 5.5 except for the last criterion (6.). Some events in column 1 exceeded the energy of 9.5 GeV after the change to the 3×3 reconstruction volume because the energy was fully reconstructed. It was important to keep these high energy events in order to calculate the correct mean energy, since the horizontal correction procedure was based on mean energies. The upper energy cut was therefore raised to 12.5 GeV

6'. $2.5 < E < 12.5$ GeV.

Further, events with

7. the hottest cell in row 1 or row 2

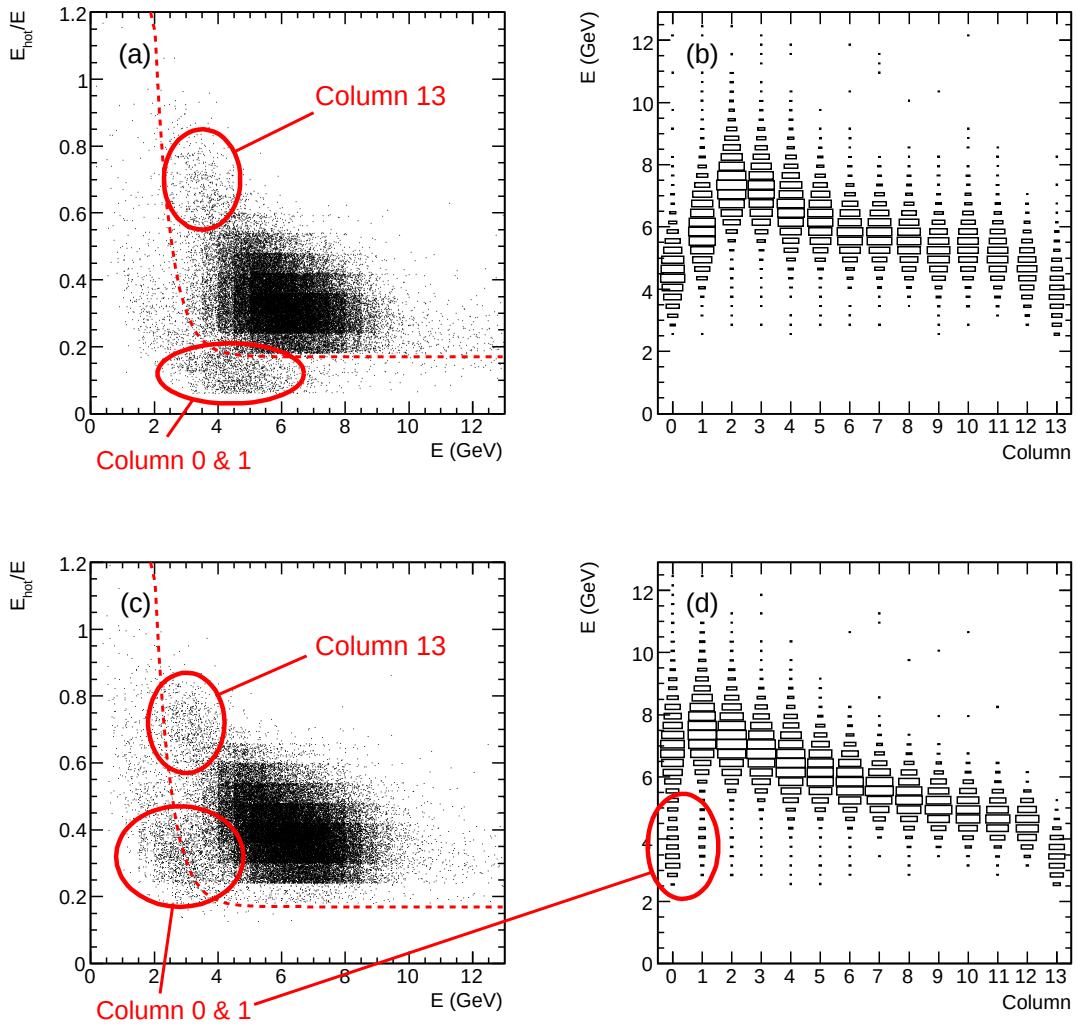

Figure 6.32: (a) Before the first horizontal correction, a bulk of events with not well confined showers in column 0 and 1 was located below the main bulk in the HER periods. (b) The energy of the events in column 0 and 1 was generally too low. (c) After correcting and switching to the 3×3 reconstruction volume, that bulk moved closer to the main bulk and was not properly rejected by the β cut (dashed line). (d) The events formed then an extra peak at low energies in column 0 and 1.

were selected, so that more than 95% of the whole sample was kept (comp. Fig. 6.13).

The ξ cut was removed i.e. events were taken independently of the x position of the shower center within the column. This was done because in this case the

correction procedure did not require the showers to be well centered in one column.

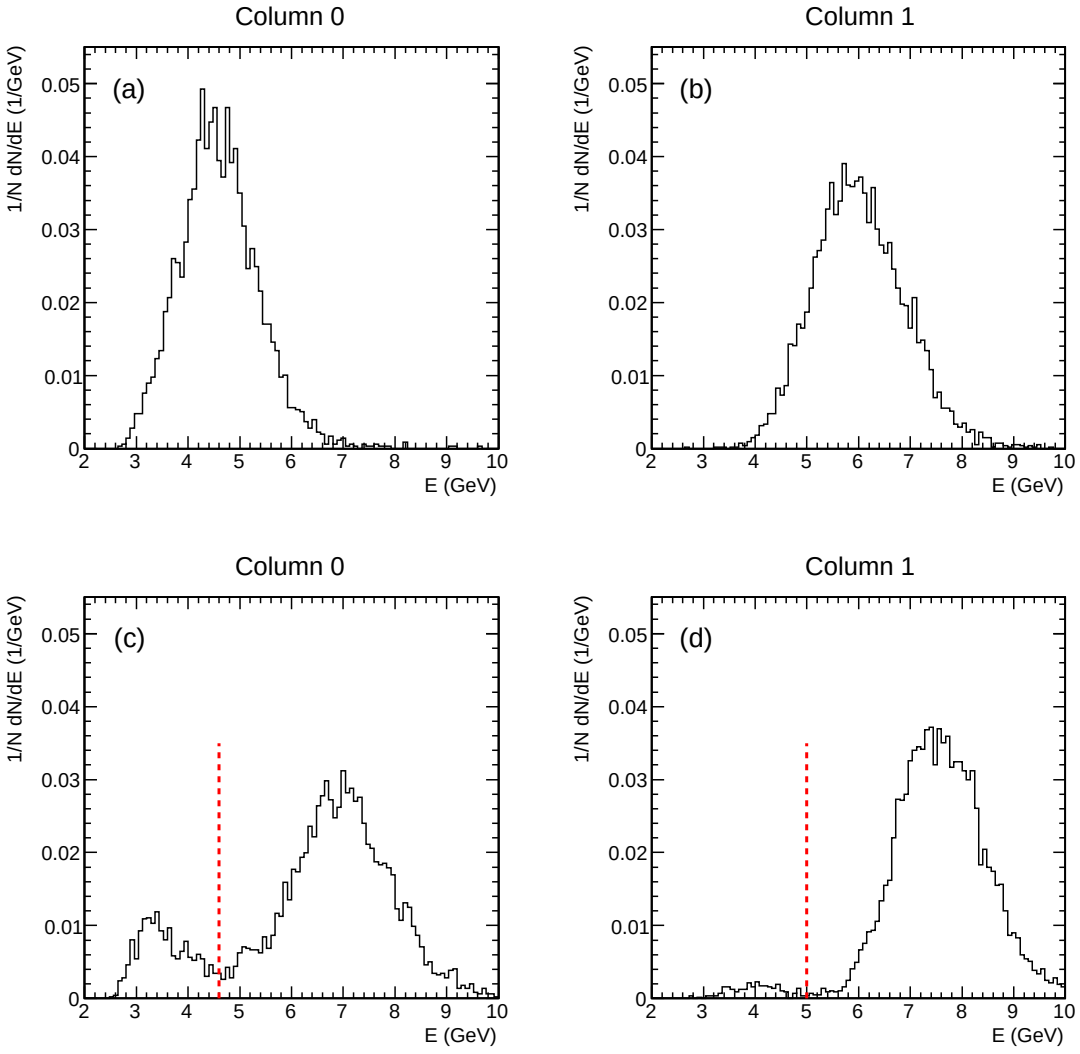

Figure 6.33: Before the first horizontal correction, the energy distributions in (a) column 0 and (b) column 1 had one peak but generally the mean was too low. (c), (d) After correcting and switching to the 3×3 reconstruction volume, the mean values improved but there were extra peaks at low energies in the HER periods. These were rejected by an energy cut indicated by the dashed lines.

Some events in the HER periods were found to be located in a separate bulk located below the main bulk in the $(E_{\mathrm{hot}}/E, E)$ plane. They were rejected by the β cut in the 0^{th} iteration, as shown for the HER1s period in Fig. 6.32 (a). After the

correction, in the 1st iteration, that bulk moved to lower energies and larger E_{hot}/E ratios (Fig. 6.32 (c)) as a result of switching to the 3×3 reconstruction volume. Some events were then passing the β cut; they were located predominantly in column 0 (84%) and also in column 1 (16%) and formed an extra peak in the energy spectrum at low energies (comp. Figs. 6.32 (d) and 6.33 (c), (d)). The origin of such events might have been due to high energy electrons which would kinematically not hit the surface of the 6 m tagger but entered it from the left side. Not all their energy was deposited in the 6 m tagger since some of the particles forming the shower were scattered outside the 6 m tagger or might have reached the end of the 6 m tagger before loosing all of their energy. One of these events is shown in Fig. 6.34. This

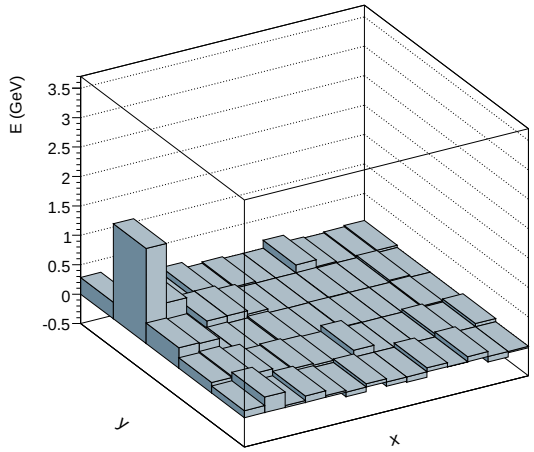

Figure 6.34: Example of an event (event 1692 in run 70201) reconstructed in column 0 with low energy ($E = 3.2$ GeV). It was presumably caused by electrons hitting the 6 m tagger from the left side.

hypothesis is compatible with the fact that the magnetic field configuration in front of the 6 m tagger as well as the position of the nominal interaction point changed when HERA was tuned for the LER and MER periods. It might be the reason why these events were only observed during the HER periods.

A second bulk at low energies but slightly larger E_{hot}/E ratios consisted of events in column 13 (Fig. 6.32 (a) and (c)). It was not possible to tighten the β cut to reject the low-energy events in column 0 and 1 since the events in column 13 would have been also rejected. Therefore an additional energy cut was introduced after the 0th iteration (Figs. 6.33 (c) and (d)). It was the same for all HER periods:

8.a) $E > 4.6$ GeV for events in column 0;

8.b) $E > 5$ GeV for events in column 1.

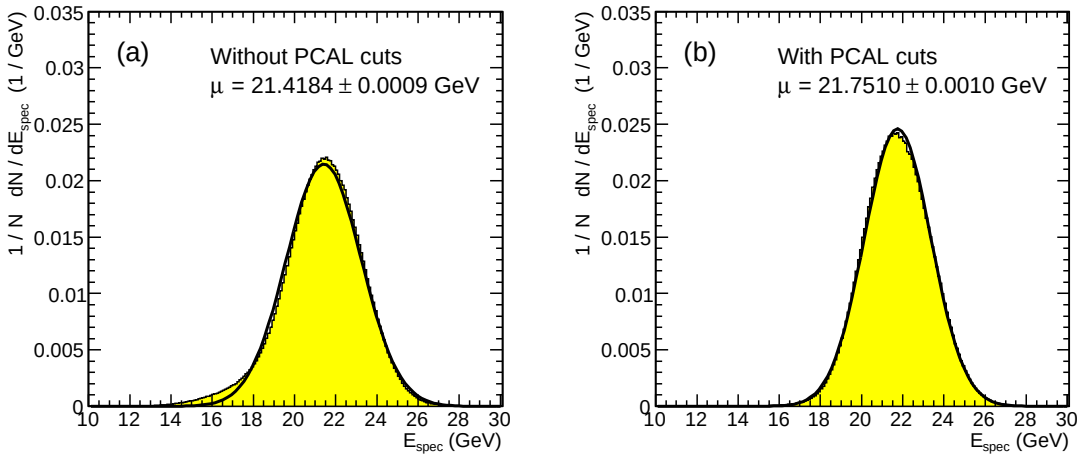

Figure 6.35: Energy distribution measured in the spectrometer (a) without and (b) with the cuts on the signal in the photon calorimeter. The low energy tail vanishes after the PCAL cuts resulting in a better agreement with a Gaussian shape and a larger mean value μ of a Gaussian fit.

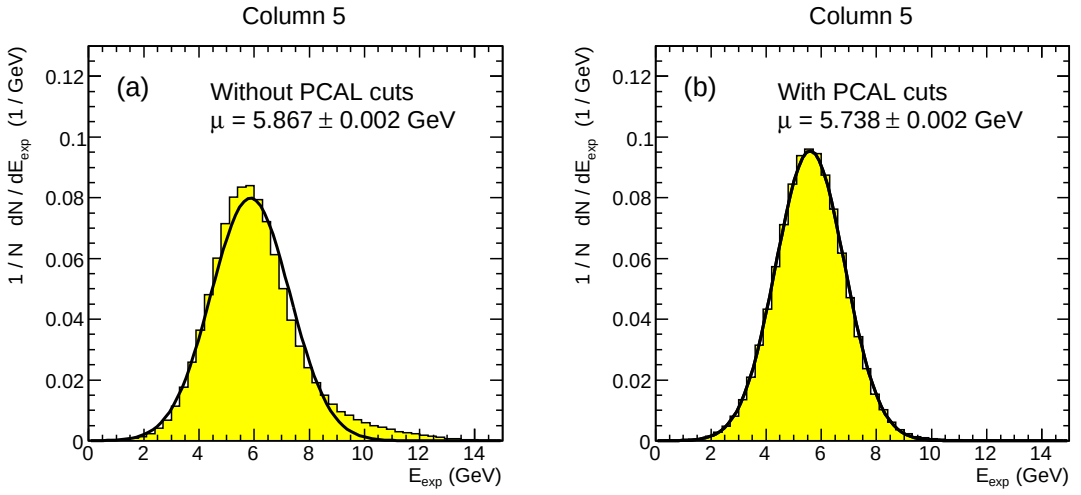

Figure 6.36: Distribution of the expected energy in column 5 (a) without and (b) with the cuts on the signal in the photon calorimeter. The high energy tail vanishes after the cuts resulting in a better agreement with a Gaussian shape and a smaller mean value μ of a Gaussian fit.

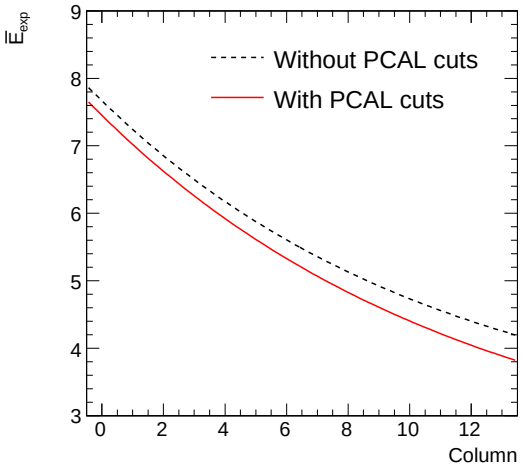

Figure 6.37: Relation E_{exp} between the expected energy and the column index n in the 6 m tagger for the LER period. The curves obtained with and without the cuts on the signal in the photon calorimeter are shown. The difference gets larger for larger n.

If in an event two Bethe-Heitler reactions took place at the vertex, if there was initial or final state radiation, or if one of the leptons from pair production radiated a photon in the exit window of the spectrometer, the energy measured in the spectrometer would have been too low. Thus the expected energy in that event would have been larger according to Eq. (6.9). This causes the low energy tail in the energy distribution of the spectrometer, shown in Fig. 6.35 (a), and likewise the high energy tail in the distribution of the expected energies, shown for column 5 in Fig. 6.36 (a). The latter shifts the mean of a Gaussian fit toward larger energies and thus shifts upward the fitted curve of the expected energy (Eq. (6.10)). This effect is shown in Fig 6.37.

The extra photon carrying the missing energy could be detected by the photon calorimeter. Therefore events were rejected if an energy deposition was found in the photon calorimeter. The photon calorimeter had two channels, in the following labeled "$\texttt{ADC}_0$" and "$\texttt{ADC}_1$". It was shielded by a filter system consisting of two absorber in series. Active material was placed behind each absorber, each representing one more channel labeled "$\texttt{AERO}_0$" and "$\texttt{AERO}_1$", respectively (comp. Section 3.2). The signals of the four channels are shown for the LER period in Fig. 6.38. Cuts were done on the ADC counts recorded in these channels:

9. an event was rejected if the number of ADC counts in one or more channels exceeded a limit.

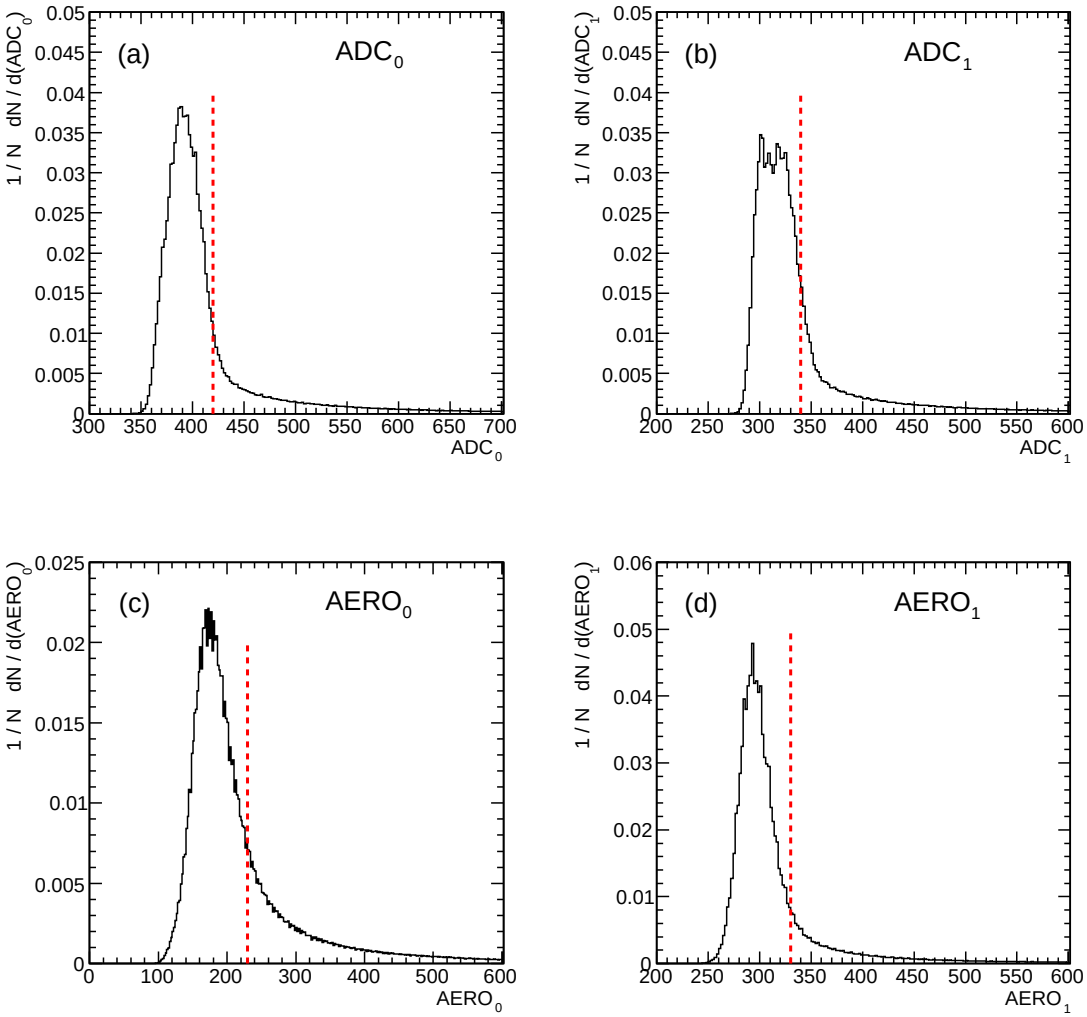

Figure 6.38: Signals in the different channels of the photon calorimeter in ADC counts for the LER period. (a), (b) show $\texttt{ADC}_0$ and $\texttt{ADC}_1$ i.e. the signals of the calorimeter itself and (c), (d) show $\texttt{AERO}_0$ and $\texttt{AERO}_1$ i.e. the signals of the detectors in the filter. The dashed lines illustrate the applied cuts.

Table 6.1 lists the limits for the different channels and run periods. They were determined empirically by requiring a sufficient rejection of the events forming the radiative tails. Their effects on the energy measured by the spectrometer and the derived expected energy are shown in Figs. 6.35 and 6.36. The tails vanish and the distributions have better agreement with Gaussian shapes. The mean expected

energies are consequently lower (comp. Fig. 6.37). The effect is of the order of 200 MeV but depends on the column.

The acceptance of the photon calorimeter was not considered when applying this cut. This appeared to be reasonable since the radiative tails in the energy distributions were shown to be sufficiently reduced.

Period	$\texttt{ADC}_0$	$\texttt{ADC}_1$	$\texttt{AERO}_0$	$\texttt{AERO}_1$
MER	400	325	200	320
LER	420	340	230	330
HER1s	445	375	240	325
HER2s	398	310	210	306
HER3	402	318	190	310

Table 6.1: Maximal ADC counts in the different channels of the photon calorimeter for the different run periods.

Finally, to reject events in which the spectrometer measured obviously wrong energies it was required

10. $E_{\text{spec}} > 5$ GeV.

In this way, few events with energies around 0 GeV were rejected (see Fig. 5.2 for the HER1s period).

6.2.2.3 Results and consistency test of the horizontal correction

The horizontal correction factors for the LER period for the three different steps of the iteration are shown in Fig. 6.39 (a). The factors of each step are a correction to the factors from the previous step (see Eq. (6.13)). The procedure converged because the values approached 1 monotonically with the steps of the iteration. After the third step, the deviations from 1 were less than 1%, in most columns in fact less than 0.1%.

Figure 6.39 (b) shows the absolute horizontal correction factors after the 2^{nd} iteration. They have to be multiplied with the vertical correction factors and the original calibration constants to obtain the new calibration constants (comp. Eq. (6.4)). The horizontal correction factors are generally larger than 1. This is due to the fact that the reconstruction volume was reduced from 25 to 9 cells. Therefore, the energy in each cell has to be larger than before. The factor in column 0 is about 2, thus significantly larger than the average. This compensates for the incorrect reconstruction of the energy of the events in this column, which was too low in the original calibration (comp. Section 4.6.3). Likewise the factor of about 0.6 provides a correct energy reconstruction in column 13. The factors in column 1 and 12 are also larger than the

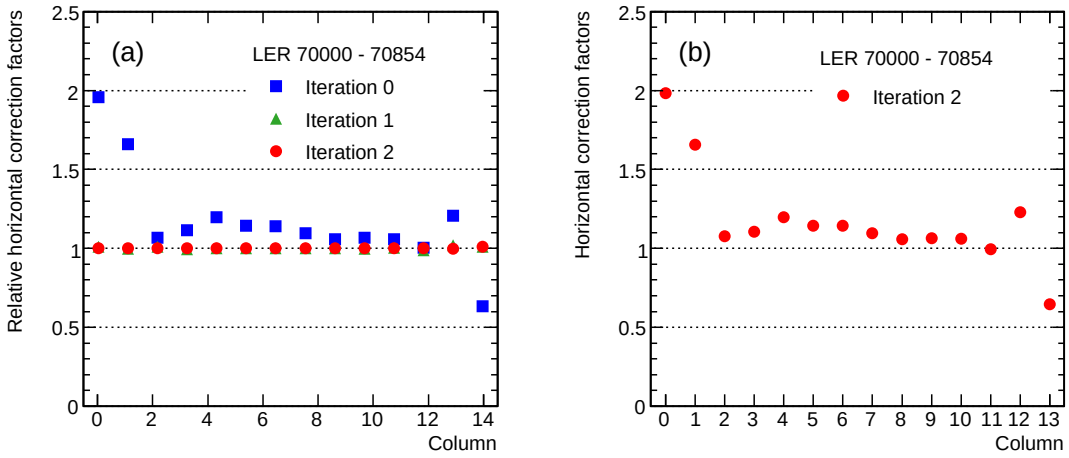

Figure 6.39: Horizontal correction factors for the LER period. (a) The factors in each step of the iteration relative to the factors of the previous step. (b) The absolute factors after the second step. They have to be multiplied with the vertical correction factors and the original calibration constants to obtain the new calibration constants.

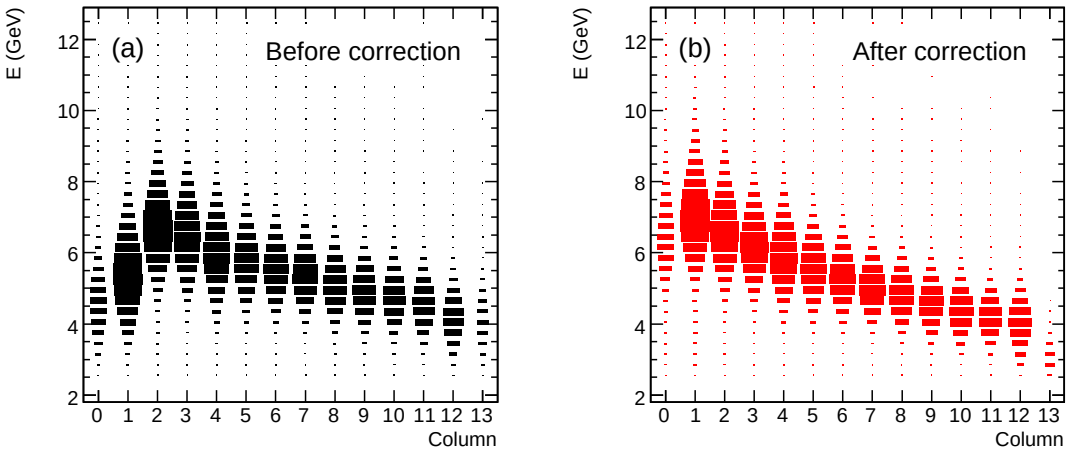

Figure 6.40: Distribution of the reconstructed energy versus column for the LER period (a) before and (b) after the horizontal correction. The vertical correction has been applied in both cases.

average. Owing to the reduced reconstruction volume, the energies of the events in these columns are now fully reconstructed while in the original 5×5 reconstruction scheme part of the energy was missing because the volume did not completely fit into the 6 m tagger.

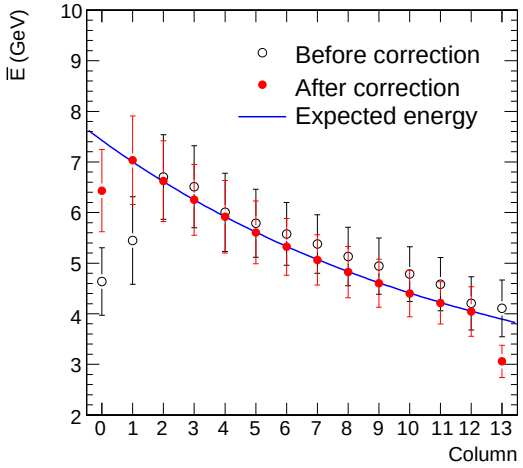

Figure 6.41: Mean energy versus column for the LER period before and after the horizontal correction. The vertical correction has been applied in both cases. The error bars are the standard deviations of the Gaussian fits of the corresponding energy distributions. The curve of the expected energy is superimposed.

The effect of the horizontal correction on the calibration and on the energy reconstruction was studied by analyzing the distribution of the reconstructed energy per column. It is shown in Fig. 6.40 (a) and (b) before and after the horizontal correction was applied, respectively. Figure 6.41 shows the mean energies per column before and after the correction, compared to the energy expected from Eq. (6.10). The mean values were derived in the aforementioned way, by filling an energy distribution for each column and fitting it with a Gaussian. The error bars give the standard deviation of these Gaussians.

The fiducial volume of the 6 m tagger, in which the energy was fully reconstructed, was increased to include columns 1 to 12 due to the smaller energy reconstruction volume. Within the fiducial volume, the corrected mean energies agree within 0.5% with the expected energy while before the correction the deviations were up to 10%. The drop of the mean reconstructed energy in column 0 w.r.t. the expected energy is of the order of 10% after the correction, as expected from the shower profile (Fig. 4.16 (a)), and from the value of $\bar{\varphi}_{\text{left}}$ (Fig. 6.30). Likewise the drop of the mean

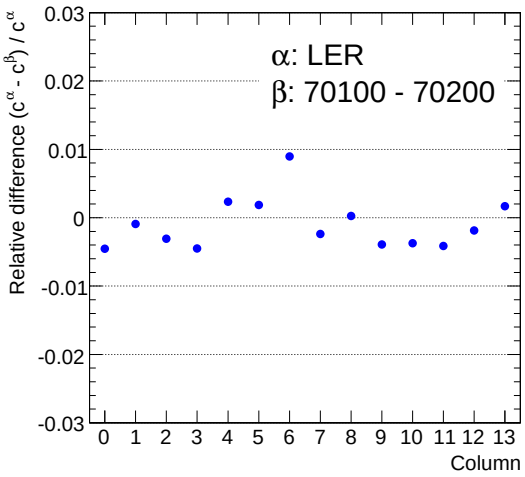

Figure 6.42: Relative difference $(c^\alpha - c^\beta)/c^\alpha$ between the horizontal correction factors c^α and c^β for two different LER periods α and β, respectively.

reconstructed energy in column 13 is of the expected order after the correction. The widths of the energy distributions in the individual columns are slightly reduced ($\approx 2\%$) as a result of the correction.

The agreement of the mean energies with the expectations is inherent to the correction procedure which shifts the mean energies according to the expected energies (comp. Eq. (6.12)). Figure 6.41 was generated using the same Bethe-Heitler events of the LER period which were also used to calculate the correction factors. Therefore, the study of the mean energies provides in this case only a consistency check of the correction procedure. An independent evaluation of its performance is done in Section 6.2.4.

The correction factors were meant to cure systematic miscalibration averaged over longer run periods (Section 4.7). The variation of the factors with time during the run periods was expected to be small. Figure 6.42 shows the relative differences between the correction factors obtained using the events of two different periods, runs 70100 to 70200 and the LER period, respectively. They are smaller than 1%. It can be concluded that the dependence of extracted correction factors on the chosen run range is weak.

6.2.3 Results of the combined vertical and horizontal correction

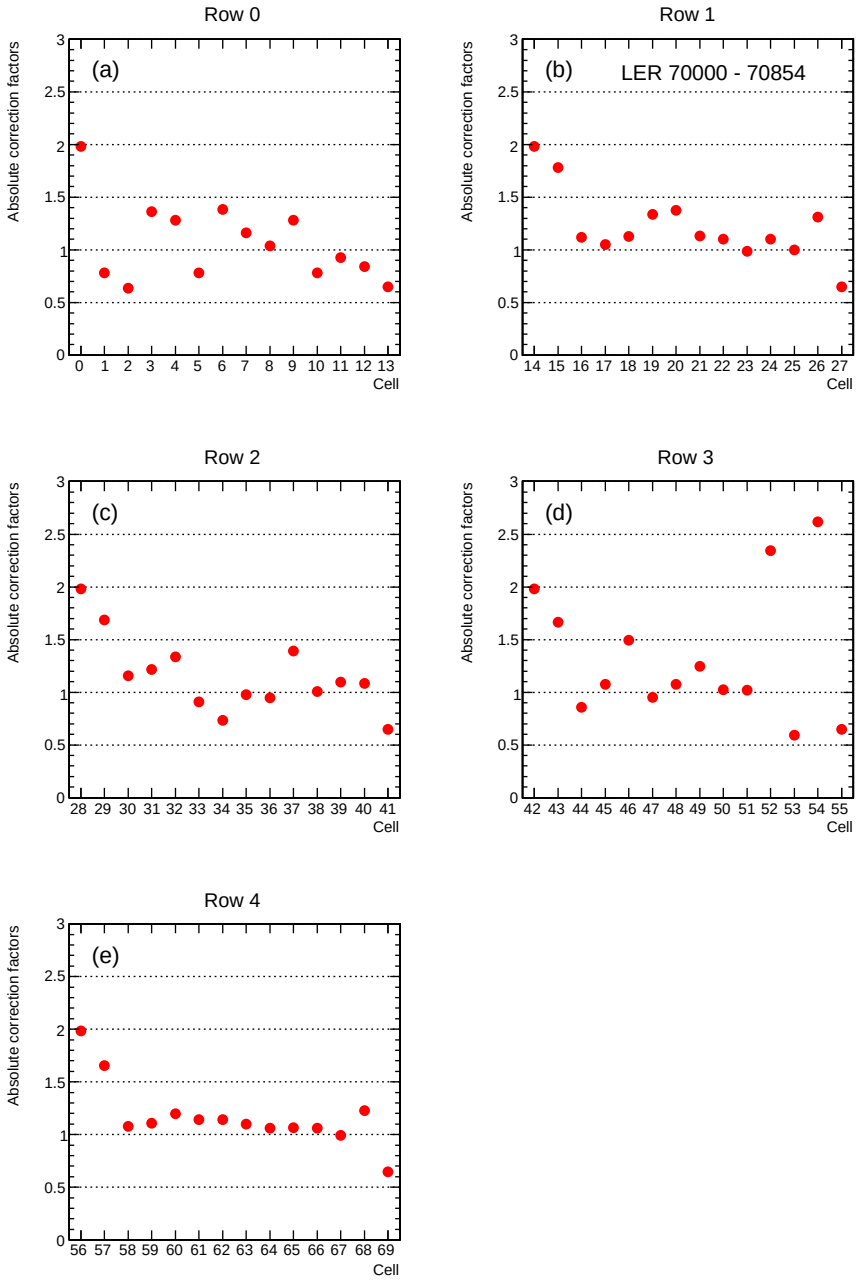

Figure 6.43: Final correction factors $c^h \cdot c^v$ for the LER period. They have to be multiplied by the original calibration constants to obtain the new calibration constants.

The vertical and the horizontal correction factors were multiplied to obtain the final correction factors which were then multiplied by the original calibration constants to obtain the new calibration constants, as stated in Eq. (6.4). The final correction factors for the LER period are shown in Fig. 6.43.

It was not possible to calculate vertical correction factors for the cells in column 0 and 13 as well as in row 4 owing to the event selection (Section 6.2.1.2). The given final factors for these cells come therefore exclusively from the horizontal correction. The correction factors for all the run periods are listed in Table C.1 in Appendix C.

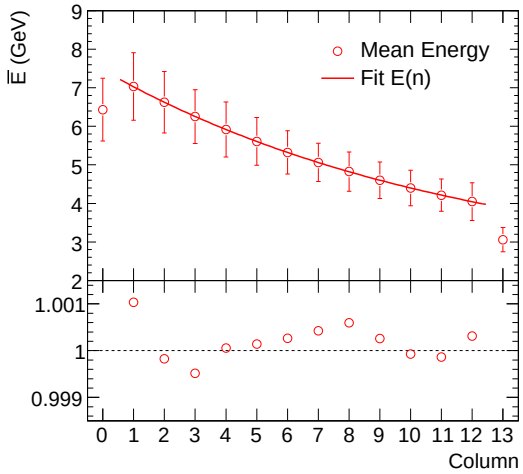

Figure 6.44: Mean energy per column for the LER period as obtained with the new calibration. The error bars show the standard deviations of Gaussian fits to the corresponding energy distributions. The superimposed curve $E(n)$ was fitted to the mean energies measured in the columns of the fiducial volume.

The mean energies of Bethe-Heitler events measured with the 6 m tagger (Fig. 6.41) were used to estimate the energy acceptance range corresponding to the fiducial volume of the 6 m tagger. Figure 6.44 shows the mean energies of the events in the different columns of the 6 m tagger obtained using the new calibration constants. As before, the mean energies are the mean values of Gaussian fits to the energy distributions per column and the errors are the standard deviations of the Gaussians. In order to obtain a relation $E(n)$ between the energy and the column n within the fiducial volume, an exponential function with offset was fitted to the mean energies in Fig. 6.44:

$$E(n) = p_0 + e^{p_1 + p_2 n}. \tag{6.14}$$

The parameters obtained from the fit are:

$$\begin{aligned} p_0 &= 2.17 \pm 0.01 \\ p_1 &= 1.668 \pm 0.002 \\ p_2 &= -0.0864 \pm 0.0003. \end{aligned} \tag{6.15}$$

For this fit, the actual errors on the mean values of the Gaussian fits were applied. $E(n)$ is superimposed in Fig. 6.44.

The values of $E(n)$ at the borders of the fiducial volume, i.e. at $n = 0.5$ and $n = 12.5$, were used as the minimum, E_{min}, and maximum, E_{max}, of the energy acceptance range. The obtained values are:

$$\begin{aligned} E_{\text{min}} &= 3.97 \pm 0.01 \text{ GeV} \\ E_{\text{max}} &= 7.24 \pm 0.01 \text{ GeV}. \end{aligned}$$

The errors on E_{min} and E_{max} were evaluated using Gaussian propagation of the errors on the parameters of $E(n)$ as given in Eq. (6.15).

The acceptance ranges for the different run periods are listed in Table A.1 in Appendix A.

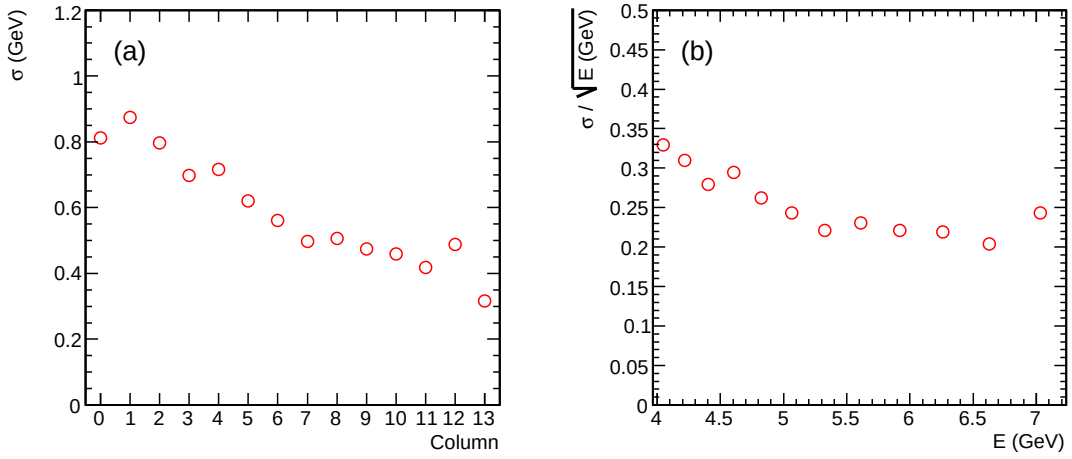

Figure 6.45: Energy resolution σ of the 6 m tagger. (a) The spread σ of the energy around the mean value $\bar{E}$ in one column as obtained from a Gaussian fit to the energy distribution of that column. (b) $\sigma/\sqrt{\bar{E}}$ as a function of the energy measured in the 6 m tagger.

The energy resolution σ of the 6 m tagger was evaluated using Fig. 6.44. σ was given by the spread of the measured energies around the mean values $\bar{E}$. It is shown

by the error bars in Fig. 6.44 and shown per column in Fig. 6.45 (a). The columns of the fiducial volume were roughly converted into bins of energy according to the relation $E(n)$ (Eq. (6.14)). This procedure is illustrated in Fig. 6.46.

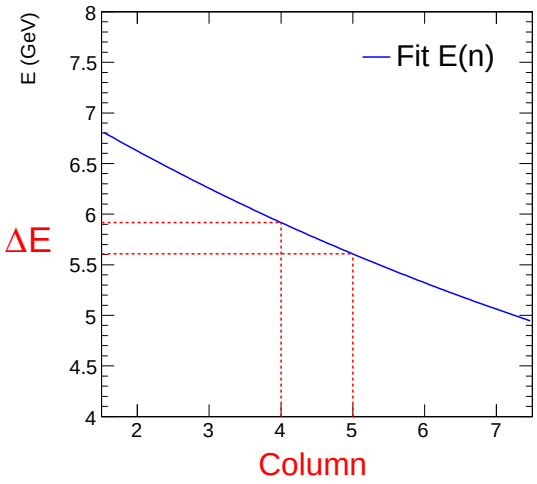

Figure 6.46: Determination of the range in electron energies ΔE corresponding to the width of one column of the 6 m tagger. The solid line represents the fitted relation $E(n)$ between the mean energy measured in the 6 m tagger and the column n (Eq. 6.14).

Hence, $\sigma/\sqrt{\bar{E}\,(\mathrm{GeV})}$ could be expressed as a function of the energy measured in the 6 m tagger (Fig. 6.45 (b)). The error shown in each bin considered statistical effects only and was obtained by Gaussian propagation of the errors on $\bar{E}$ and σ returned by the Gaussian fit on the energy distribution in that bin.

The values show significant fluctuations. The main uncertainty is introduced by the finite width of the columns of the 6 m tagger. The uncertainty of the energy associated with half of the width of a column is ≈ 0.2 GeV (comp. Fig. 6.46) and has to be considered as a systematic error on the determination of the resolution. The stochastic term a of the resolution (comp. Section 2.3) is of the order of 25%.

6.2.4 Evaluation of the performance of the vertical and horizontal correction

It is the objective to conclusively evaluate the performance of the improved calibration. This has been done before (Sections 6.2.1.3 and 6.2.2.3) by comparing certain control distributions obtained from Bethe-Heitler events which were either calibrated using the original constants or with the correction factors applied. The events which

were used to generate the control distributions were the same which were used before to calculate the correction factors, though. The investigation of these distributions provided an important consistency check of the presented techniques. However, it is questionable whether they allowed a verification of the applicability of the improved 6 m tagger calibration independently of the selected set of events. This is in particular the case for the evaluation of the performance of the energy reconstruction, as discussed in Section 6.2.2.3.

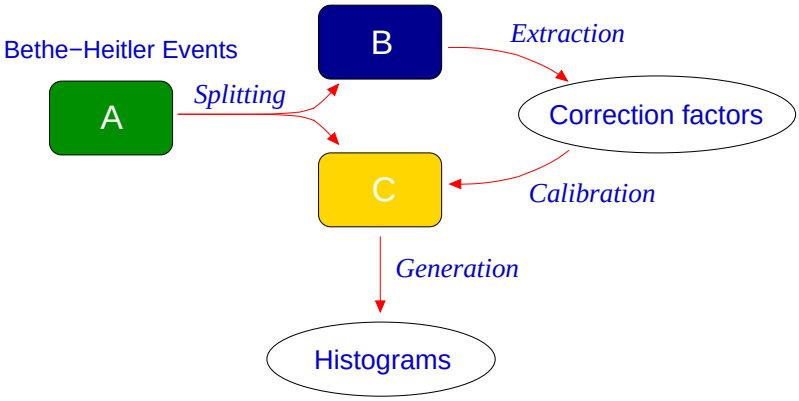

Figure 6.47: A sample A of Bethe-Heitler events was split into two independent samples B and C. B was used to calculate correction factors and C was used to generate histograms to evaluate the performance of the improved calibration.

The control distributions were therefore generated again using two independent sets of Bethe-Heitler events from the same run period, as illustrated in Fig. 6.47: the original sample A of Bethe-Heitler events was split into two samples, B and C, which did not overlap. This was done by assigning the events having an even entry in the data files to the set B and the events with an odd entry to the set C. The events in B were used for the calculation of a set correction factors. These correction factors were then used for the calibration of the events in C. The control distributions were generated with the events in C. The results discussed in the following were obtained taking A as the LER period. The discussions are mostly analogue to the ones in Sections 6.2.1.3 and 6.2.2.3 and therefore kept brief except for when differences occurred.

Figure 6.48 shows the distributions of the number of events per column within row 1 and 2 before and after the correction. It confirms the improvement of the relative calibration of the cells within one column as discussed in Section 6.2.1.3 for the analogue Fig. 6.22. In difference to Fig. 6.22, some miscalibration appear also in column 12, apparently due to the horizontal correction.

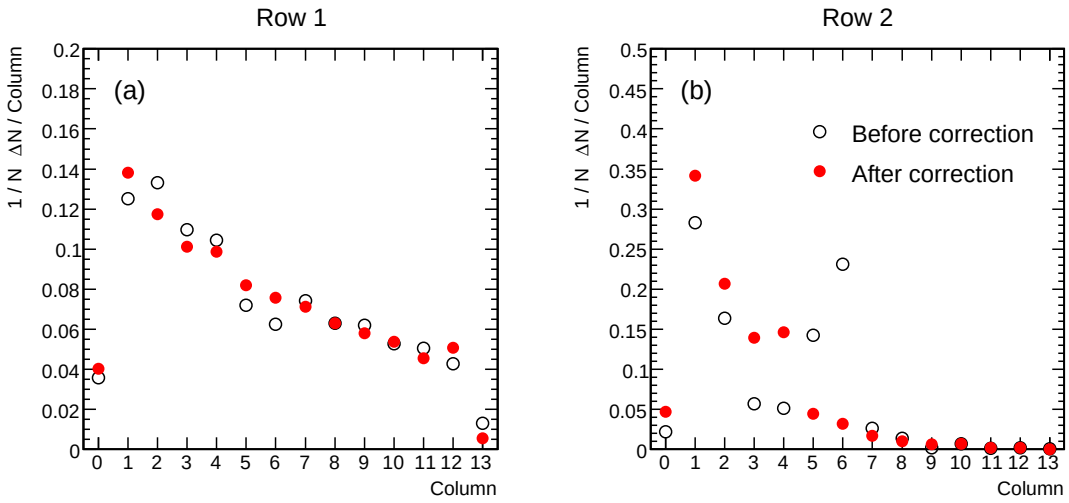

Figure 6.48: Number of events in a particular column. The distributions obtained before and after the correction factors were applied to the original calibration constants were compared. (a) Hottest cell in row 1, (b) hottest cell in row 2.

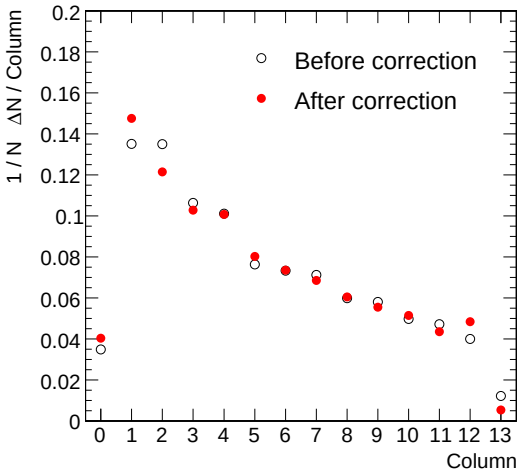

Figure 6.49: Number of events in the 6 m tagger columns. The distributions obtained before and after the correction factors have been applied are compared. All rows are included.

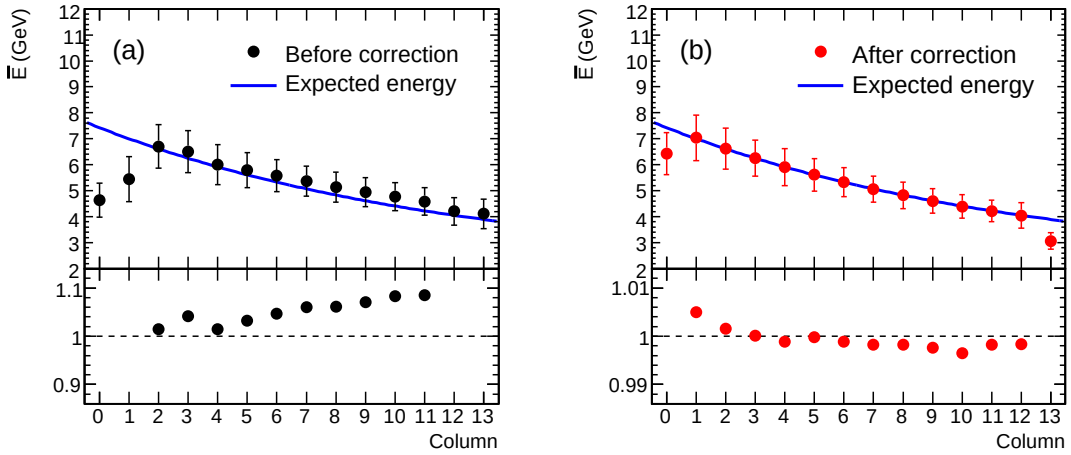

Figure 6.50: Mean energy per column before and after the correction. The energies are the mean values of Gaussian fits to the energy distributions of the events in the corresponding columns. The error bars are the standard deviations of the Gaussians. The bottom pad shows the ratio of the mean reconstructed and the expected energy.

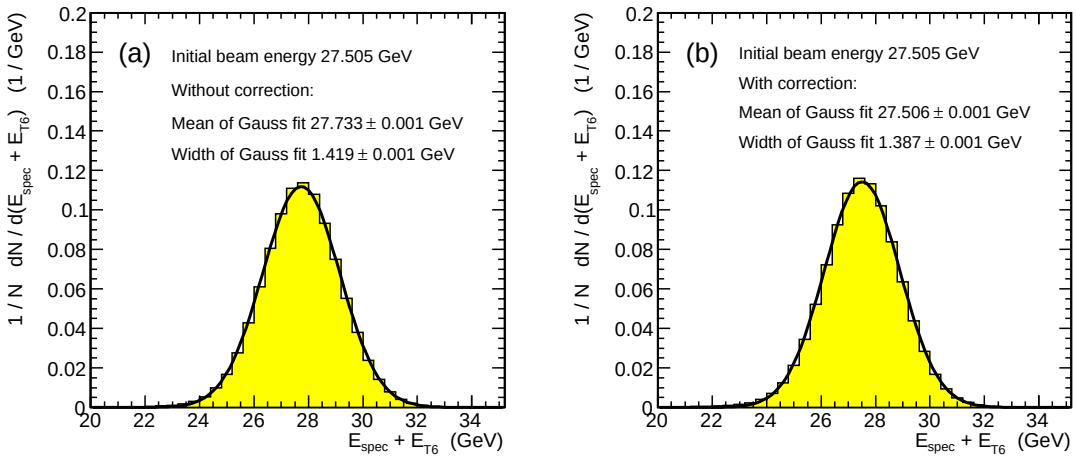

Figure 6.51: Sum of the energies measured in the spectrometer and in the 6 m tagger (a) before and (b) after the correction. All events having the hottest cell in the fiducial volumes were considered. The mean values and standard deviations of Gaussian fits are indicated.

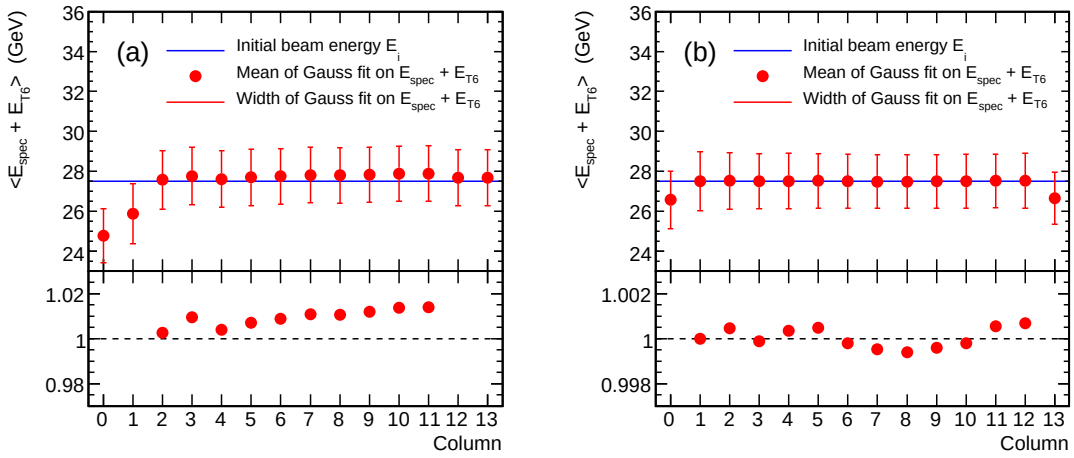

Figure 6.52: For each column of the 6 m tagger, the mean values of the sum of the energies measured in the spectrometer and in the 6 m tagger (a) before and (b) after the correction. They are the mean values of Gaussian fits to the distribution of the sum in the corresponding column. The error bars give the standard deviations of the Gaussians. The bottom pad shows the ratio between the measured mean value and the nominal beam energy (for the columns within the fiducial volumes).

The distribution of the number of events per column for all rows (Fig. 6.49) is likewise closer to the expected smoothly decreasing behavior after the correction. Some miscalibration remain in particular in columns 3, 4, and also in column 12.

The mean energies per column before and after the correction are compared to the expected energy (Fig. 6.50), analogue to Fig. 6.41 in Section 6.2.2.3. The deviations of the reconstructed mean energies from the expected energies are up to 10% within the fiducial volume for the original calibration. They are reduced to less than 0.5% as a result of the correction. The drop of the energies in column 0 and 13 is at the expected level after the correction.

The energies of an electron and a photon from a Bethe-Heitler process sum up to the initial electron energy. Thus, the sum of the energies measured in the 6 m tagger and measured in the spectrometer were expected on average to be equal to the nominal electron beam energy. The distributions of this sum before and after the correction are shown in Fig. 6.51. Only events with the hottest cell within the fiducial volume, i.e. from column 2 to 11 for the original calibration and from column 1 to 12 for the improved calibration, were included. The same sum was calculated for each column individually. The mean values of Gaussian fits to these distributions are shown in Fig. 6.52 and their standard deviations are given as the error bars.

The deviation of the mean values from the initial beam energy was reduced from $\approx 1\%$ to less than 0.01% as a result of the correction. The width of the Gaussians were slightly decreased by about 2%.

6.2.5 Conclusions

The presented method of a separated vertical and horizontal correction based on Bethe-Heitler events has been demonstrated to significantly improve the original calibration of the 6 m tagger. The cells within one column were calibrated in a consistent way relative to each other for the most part. The absolute calibration of the cells as well as the energy reconstruction were revised leading to a very good agreement between the reconstructed and the expected energies. Likewise the fiducial volume of the 6 m tagger was increased and the energy reconstruction in the outer columns was improved.

7 Shower selection and acceptance studies

In this Chapter, some applications of the improved calibration and energy reconstruction of the 6 m tagger are illustrated.

- In section 7.1, a set of cuts is developed for the selection of good showers in the 6 m tagger independent of the information coming from other devices (like for example the spectrometer). Some criteria to qualify an event depending on the reconstructed energy and the shape of the shower are determined.

- In section 7.2, the new event selection is then used to study the acceptance of the spectrometer to identify Bethe-Heitler photons.

- In section 7.3, the energy resolution of the spectrometer is measured.

All these studies are done using the data of the runs collected during the LER period which met the `6mtake` quality conditions '1' or '2'. Corrupted events were rejected using the cuts described in Section 5.4.

7.1 Criteria for the selection of showers in the 6 m tagger

A set of selection criteria was developed to evaluate the quality of an event measured in the 6 m tagger. The criteria were based on the reconstructed energy, the shape, and the isolation of the electromagnetic shower. Hence, the event selection was independent of the information coming from other devices, like for example a coincidence of a photon in the spectrometer for the selection of Bethe-Heitler events (Section 5.3). Identifying showers of different qualities allowed to select event samples having different purities. A sample of events of the highest possible quality would include a large fraction of signal events, like for example Bethe-Heitler or photoproduction events, and only a small fraction of background events. Thus, the purity would be very high while the efficiency would be lower since together with background events also signal events could be rejected. The opposite is true for events of a lower quality.

Events were selected using a random trigger in order to obtain a sample composed of signal, background, and noise events in the fractions observed in the data.

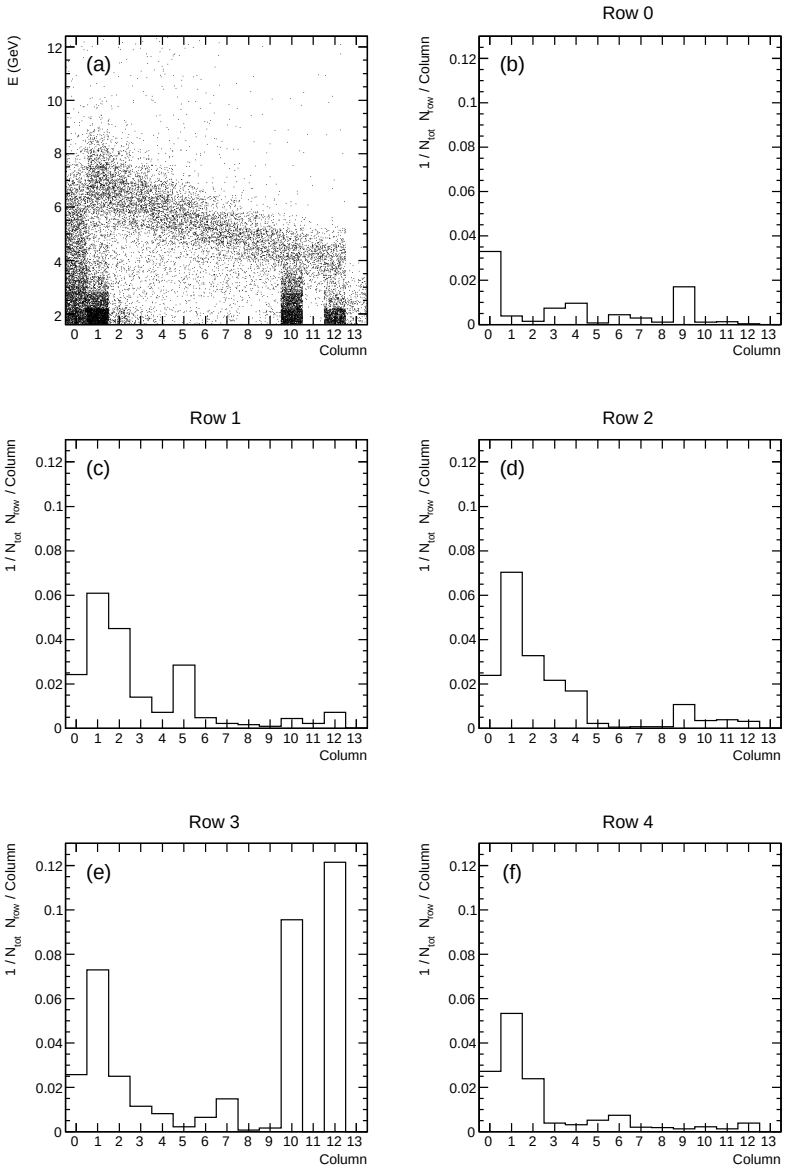

Figure 7.1: (a) Reconstructed energy per column. Columns 0, 1, 10, and 12 feature a large contribution of low energy events caused by noisy cells. Additionally, low energy background events are found in each column. (b) – (f) Distributions of the number of events per column for the different rows of the 6 m tagger. They are normalized to the total number of events in all rows. The noise in columns 10 and 12 of (a) is due to the excess observed in the same columns in row 3 (e).

7.1.1 Noisy cells

Figure 7.1 (a) shows the reconstructed energy per column of the 6 m tagger. A large amount of events with the hottest cell in columns 0, 1, 10, and 12 was located below the band populated by events in which the electrons were scattered with transverse momentum $p_T \approx 0$ GeV/c at the interaction point (Section 4.4). Figures 7.1 (b) to (f) show the distributions of the number of events per column in each row of the 6 m tagger. The distributions were normalized to the total number of events in all rows. As the events were selected by a random trigger, the distributions were expected to have a noise component coming from events in which no electron hit the 6 m tagger, and a component coming from signal. The noise component was expected to cause an equal amount of entries in all columns and rows while the signal component was expected to contribute predominantly in row 1 and 2. This is roughly observed.

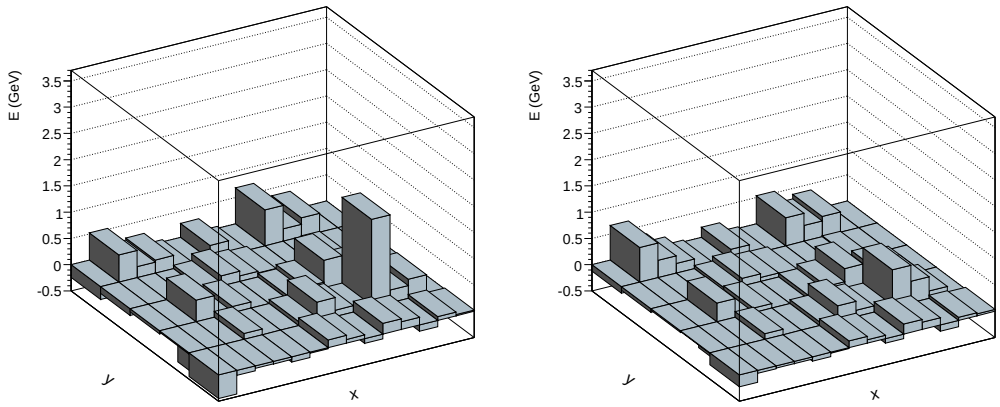

(a) (b)

Figure 7.2: Example of an event in which the hottest cell is number 52 (event 134 in run 70201). (a) Energy reconstruction using the improved calibration constants and (b) using the original calibration constants. The reconstructed energies were (a) 3.0 GeV and (b) 2.0 GeV.

As seen in Fig 7.1 (e), about 20% of the events had the hottest cell in columns 10 and 12 of row 3 i.e. in cells 52 and 54. Figure 7.2 (a) shows a display of one of these events. Since in this type of events the signal is very confined into a single cell and does not show a topology compatible with that of an electromagnetic shower, this signal was probably caused by electronic noise.

The correction factors (Fig. 6.43) for cells 52 and 54 are significantly larger than the average. This is the reason of the excess observed in Fig. 7.1 (e). Figures 7.3 (a) and (b) show the same distributions as in Fig. 7.1 (a) and (e), this time generated

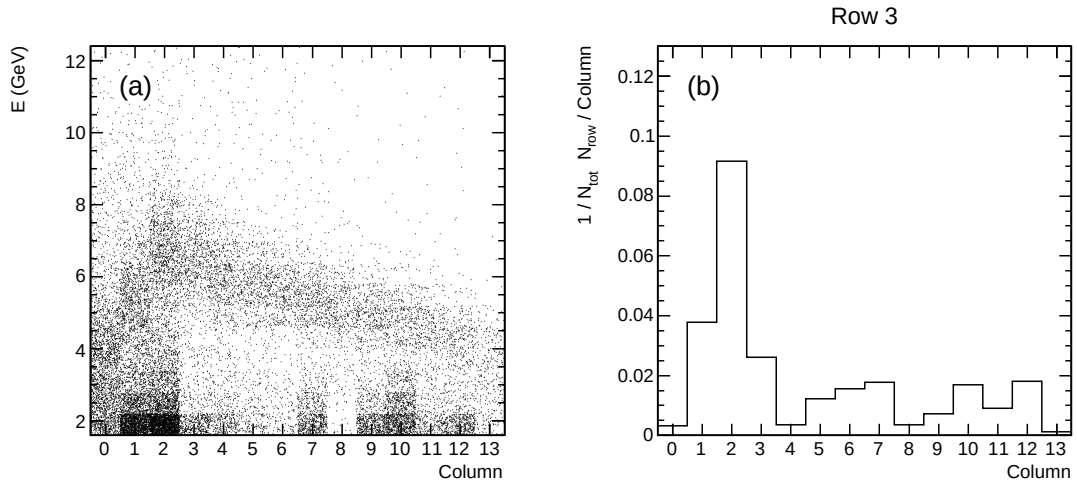

Figure 7.3: Distribution of (a) energy versus column and (b) number of events per column obtained using the original calibration. (b) was normalized to the total number of events in all rows.

using the original calibration constants. The excess is not as evident as before though the noise contribution is slightly larger than the average in columns 10 and 12. The correction increases the energy measured in one cell due to the smaller reconstruction volume. As a consequence, cells 52 and 54 are not only more often the hottest cells in the events but the reconstructed energy is also larger than before. This can be seen by comparing Figs. 7.1 (a) and (e) with the corresponding Figs. 7.3 (a) and (b).

Many other cells in Figs. 7.1 (b) – (f) also feature more entries than expected, in particular in columns 0 to 2, rows 3 and 4. The low energy entries in these columns observed in Fig. 7.1 (a) are attributed to the presence of these noisy cells.

The correction factors (Fig. 6.43) were obtained from events having the hottest cells in rows 1 and 2, but the cells in row 3 were also used for the energy reconstruction. If the signal in some of the cells in row 3 was distorted by noise, this might have influenced the correction procedure. In particular the vertical correction could have been spoiled, and this could have caused the miscalibration observed in column 12 in Fig. 6.49. The correction procedure was therefore repeated masking the cells 52 and 54 by artificially setting the energy measured in the cells to 0 GeV before searching for the hottest cell and reconstructing the energy. This is a reasonable assumption for the energy deposition in Bethe-Heitler events, since the shower maximum was located toward the center of row 1 if the electron hit the 6 m tagger in columns 10 or 12. Therefore the actual energy deposited in row 3 was expected to be negligible owing to the narrow transverse shower profile (Section 2.1). Equation (6.5) had to

be modified to

$$\alpha = \frac{\bar{E}_0 + \bar{E}_1 + \bar{E}_2}{f_{01} + 1 + f_{21}}$$

for these cells. Consequently, no correction factors could be obtained for cells 52 and 54.

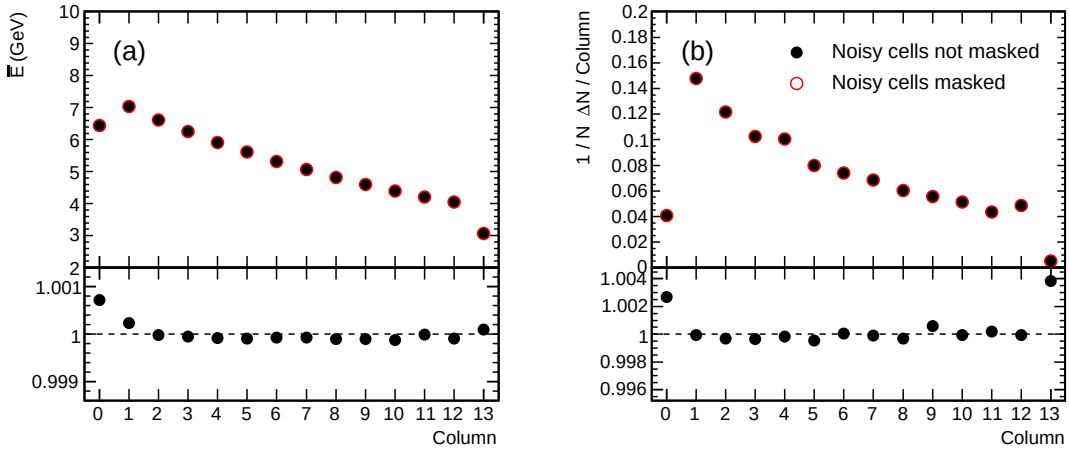

Figure 7.4: Comparison of (a) the mean energy per column and (b) the number of events per column using different correction factors. The correction factors were obtained as described in Section 6.2 and obtained by masking the noisy cells 52 and 54. The bottom part shows the ratio of the two distributions.

The control distributions of the number of events per column and the mean energy per column obtained with these new correction factors were compared to those obtained with the correction factors obtained as described in Section 6.2 (Fig. 7.4). The observed difference in the number of entries per column was below 0.5%. The noisy cells did not influence the correction procedure and in particular the aforementioned miscalibration was not recovered. The energy deposition in the noisy cells is apparently negligible as discussed before.

As a consequence, the correction factors were not recalculated. In the energy reconstruction, however, the noisy cells 52 and 54 were masked. Events in which the hottest cell was 52 or 54 were therefore discarded. Figure 7.5 shows the comparison of the distributions of the reconstructed energy per column before and after the masking. The excess of low energy events in columns 10 and 12 vanished. In the following, this masking was applied for the generation of all plots.

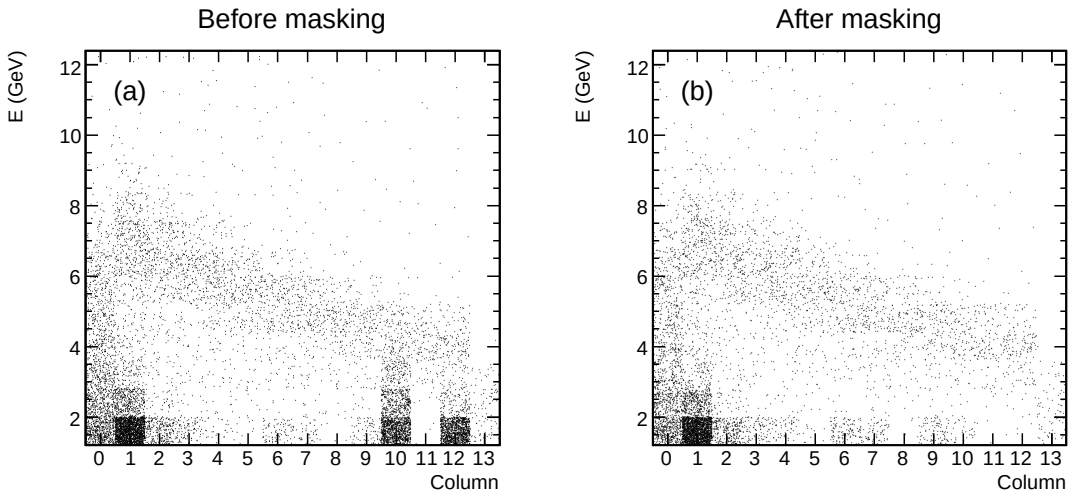

Figure 7.5: Comparison of the distribution of the reconstructed energy per column (a) before and (b) after masking the noisy cells 52 and 54. The low energy events in columns 10 and 12 vanished due to the masking.

7.1.2 Background events

Many events not coming from noisy cells were populating the region below the main band in Fig. 7.1 (a) and a few events the region at higher energies. An example of

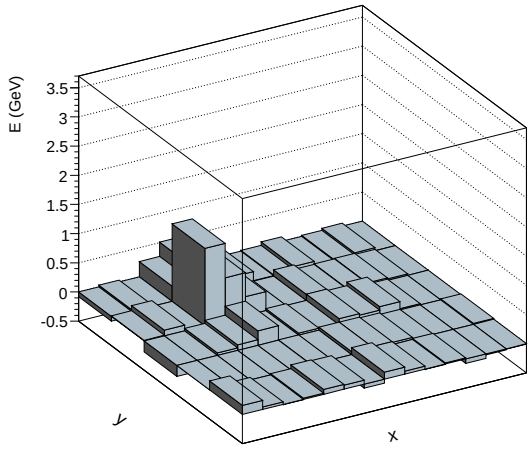

Figure 7.6: Example of a typical background event in column 3 with a reconstructed energy of 3.1 GeV (event 87023 in run 70211).

these events is shown in Fig. 7.6. It has the topology of an electromagnetic shower. The energy of these events was, however, lower or larger than the expectations for events with $p_T \approx 0$ GeV/c (the central band in Fig. 7.1 (a)). There were several possible reasons which could explain the origin of these events.

- Most of the electrons from the Bethe-Heitler processes occurring at the interaction point were emitted with $p_T \approx 0$ GeV/c (comp. Section 4.4). They were deflected by the magnetic dipole field in front of the 6 m tagger and hit the detector at a certain x position depending on their energy. If an electron was emitted with a non-zero momentum p_x in a collision with a proton, however, and traversed the dipole field, it hit the 6 m tagger at a different x position than a $p_T \approx 0$ GeV/c electron with the same energy. In turn, electrons with $p_x \neq 0$ GeV/c would have different energies than $p_T \approx 0$ GeV/c electrons at the same x position in the 6 m tagger [33].

- Interaction of electrons in satellite bunches, or of off-momentum electrons with the protons or with residual gas in the beam pipe could produce electrons not coming from the nominal interaction point. These would be deflected in a different way by the magnetic system, and therefore would not lie in the same E versus column band of the Bethe-Heitler events [33].

- It might also be possible that electrons hitting the beam pipe generated secondary particles which were scattered into the 6 m tagger.

In either case, an electron would most likely traverse the various magnetic fields in front of the 6 m tagger in a different way than if coming from the nominal interaction point and thus the correlation between energy and position would be affected.

The relative contribution of these background events was compared to the contribution from Bethe-Heitler events. Figure 7.7 (dashed line) shows the distributions of the reconstructed energy in columns 3 and 10 as an example. The rise at the low energy side of the distributions belongs to the pedestal peak at 0 GeV. The peaks at about 6 GeV and 4.5 GeV in columns 3 and 10, respectively, are the Bethe-Heitler signals while the peaks in between at 3.5 GeV and 3 GeV, respectively, are caused by the background events. The rate of higher energy events is much lower than that of lower energy events.

The same distributions were generated for a data sample enriched in non-Bethe-Heitler events (Fig. 7.7 (solid line)). This was achieved by rejecting the events in which the signal in one or more of the four channels of the photon calorimeter exceeded the limits listed in Table 6.1. Assuming a photon calorimeter acceptance of 100%, only the Bethe-Heitler events were accepted in which the photon converted in the exit window of the spectrometer (about 10%) and which were found in the acceptance range of the spectrometer (Section 3.2). The peaks of the Bethe-Heitler signal were reduced accordingly. The amount of background events was reduced by

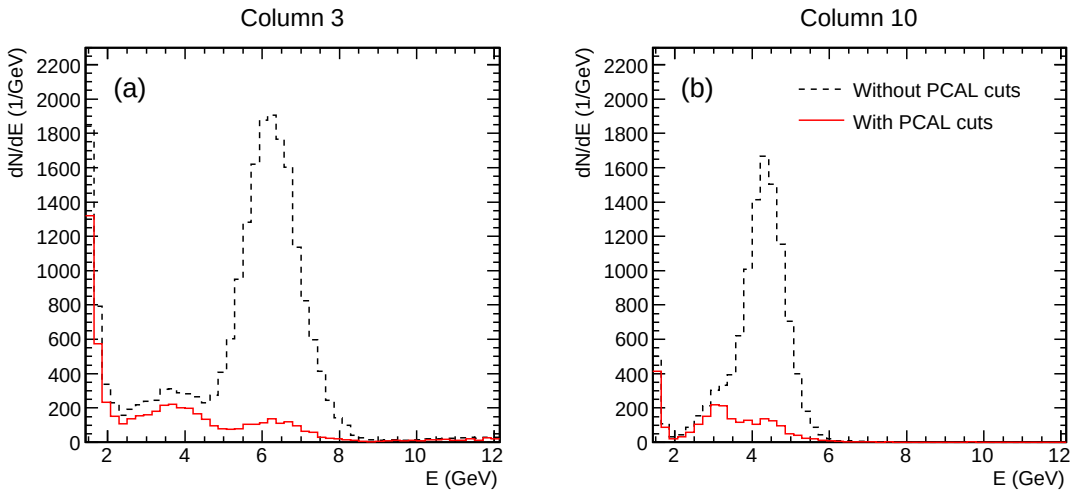

Figure 7.7: Energy distribution of the events with the hottest cell (a) in column 3 and (b) in column 10 without (dashed line) and with (solid line) the cuts on the energy measured by the photon calorimeter.

a much smaller factor. This supports the assumption that the background events were not produced by corrupted measurements of the Bethe-Heitler events but came from some independent physical process, like the ones listed above.

7.1.3 Selection criteria

Events were selected first of all by cutting on the energy. The cut was tuned to accept only events in which an electromagnetic shower was measured in the 6 m tagger and to reject background events. The distributions discussed in the following were generated using events having the hottest cell in columns 1 to 12 and in rows 1 to 3 to ensure full energy reconstruction.

The energy cut was defined depending on the mean, $\bar{E}$, and the width, σ_E, of the signal peak in each column. In order to avoid a possible influence of the background events on the determination of $\bar{E}$ and σ_E, both values were obtained from the good Bethe-Heitler events selected for the horizontal correction (Section 6.2.2.2). These values are shown in Fig. 6.50. The mean energies are also shown in Fig. 7.8 (a). Additionally, a lower and an upper cut on the energy are shown for each column. These were defined as:

$$E_{\text{low}} = \bar{E} - a\sigma_E$$
$$E_{\text{up}} = \bar{E} + b\sigma_E$$

An exponential curve was fitted through these limits, specifying the lower and the

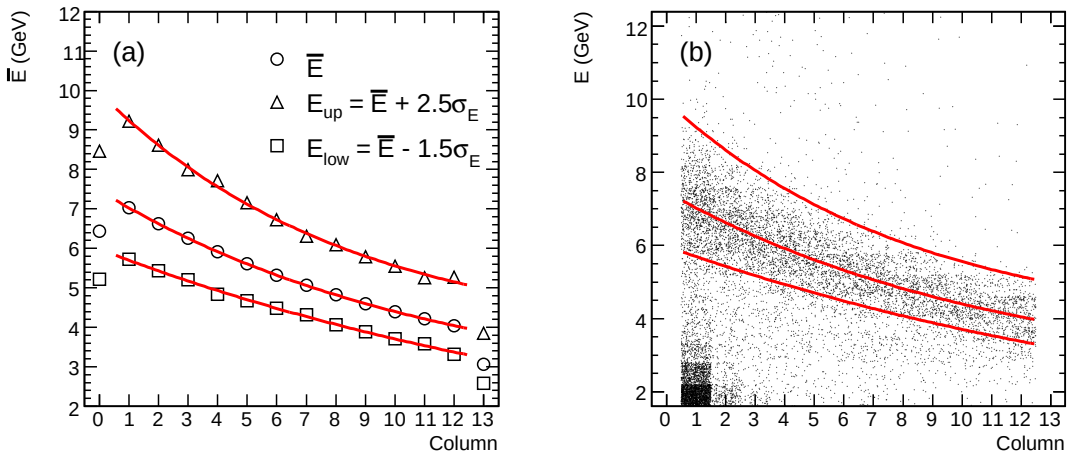

Figure 7.8: (a) Circles: Mean energies, $\bar{E}$, per column as obtained from the energy distributions of Bethe-Heitler events. Triangles and squares: $\bar{E} + 2.5\sigma_E$ and $\bar{E} - 1.5\sigma_E$, respectively, where σ_E is the standard deviation of the energy distribution of the Bethe-Heitler events in each column n. The solid lines are exponential fits with offset defining the mean energy as well as the final energy cuts $E_{\text{low}}(n)$ and $E_{\text{up}}(n)$. (b) Distribution of the energy per column as obtained with the random trigger. The bands from (a) are superimposed.

upper energy cut, $E_{\text{low}}(n)$ and $E_{\text{up}}(n)$, respectively, depending on the column n:

$$E(n) = p_0 + e^{p_1 + p_2 n}. \tag{7.1}$$

Figure 7.8 (b) shows the distribution of energy versus column with $E_{\text{low}}(n)$ and $E_{\text{up}}(n)$ superimposed for $a = 1.5$ and $b = 2.5$. The reason why those particular values have been chosen is explained below.

The parameters a and b were varied to define different quality classes for the shower. Figure 7.9 shows the distributions of the reconstructed energy in columns 3 and 10. They show the previously discussed tail from the pedestal peak, the peak caused by background events and the signal peak. The background and signal peak moved closer together in column 10. This was presumably due to the different correlation between their energy and position which lead to a different slope of their energy versus column distribution. Three different energy cuts were defined, indicated by the vertical lines. The corresponding sets of parameters a and b as well as p_0, p_1, and p_2 of the functions $E_{\text{low}}(n)$ and $E_{\text{up}}(n)$ (Eq. 7.1) are listed in Table 7.1. For the tightest cut, a was 1.5 and b was 2.5. With this cut about 92.7%

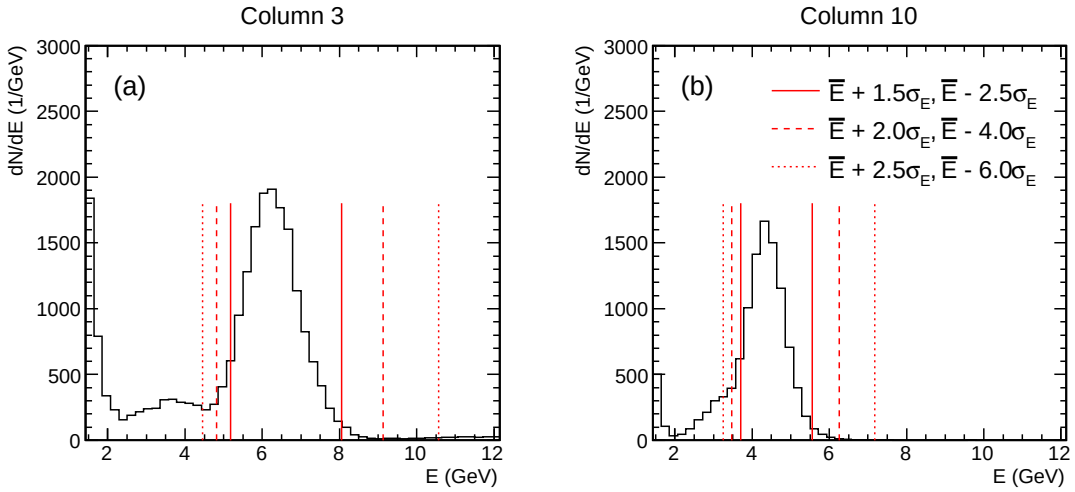

Figure 7.9: Energy distributions of the events (a) in column 3 and (b) in column 10. The pedestal peak at very low energies, a peak around 3 GeV caused by background events, the signal of Bethe-Heitler events around (a) 6 and (b) 4 GeV, and a small contribution from high energy background events are visible. The vertical lines indicate the three different sets of energy cuts.

of the Bethe-Heitler events were expected to be accepted. (This is the normalized integral of a Gaussian around $\bar{E}$ from $\bar{E} - 1.5\sigma_E$ to $\bar{E} + 2.5\sigma_E$.)

Set	Limits			$E_{\text{low}}(n)$			$E_{\text{up}}(n)$		
	a	b	I_b^a/I (%)	p_0	p_1	p_2	p_0	p_1	p_2
1	1.5	2.5	92.7	0.26	1.744	−0.0507	3.63	1.843	−0.1189
2	2.0	4.0	97.7	−1.6	1.96	−0.0331	4.33	1.961	−0.1309
3	2.5	6.0	99.4	−11.71	2.8157	−0.01105	5.19	2.109	−0.1423

Table 7.1: Sets of parameters for the different applied cuts. I_b^a/I is the fraction of the integral of a Gaussian around $\bar{E}$ from $\bar{E} - a\sigma_E$ to $\bar{E} + b\sigma_E$ compared to $1/(\sigma\sqrt{2\pi})$. It provides an estimation of the amount of accepted Bethe-Heitler events. The parameters p_0, p_1, and p_2 of the functions $E_{\text{low}}(n)$ and $E_{\text{up}}(n)$ are given to the accuracy of their fit.

The next criterion for the selection of good events in the 6 m tagger was based on the shape of the transverse profile of the electromagnetic showers. The shape was estimated by analyzing the fraction E_4/E, where E_4 is the energy contained in the

four adjacent cells with most energy, including the hottest cell, and E is the total energy of the shower. The fraction E_4/E was therefore related to the fraction of the energy within the central part of the shower: if the profile was very broad, less energy was expected to be deposited in the central part and E_4/E was expected to be small. This quantity is similar to E_{hot}/E used for the selection of Bethe-Heitler events (Section 5.3) but it is less dependent on the position of the actual shower maximum within the hottest cell.

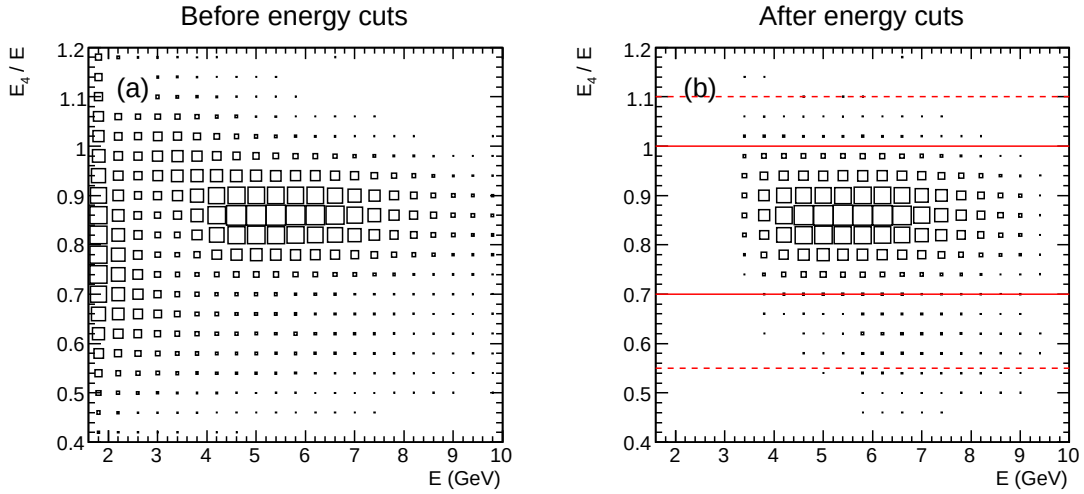

Figure 7.10: Distribution of the fraction of energy, E_4, contained in the four adjacent cells with most energy, including the hottest cell, compared to the total energy, E, of the shower. E_4/E is given as a function of E. (a) All events with the hottest cell between column 1 and 12 as well as row 1 and 3; (b) after additional energy cuts (set 1, $\bar{E} - 1.5\sigma_E < E < \bar{E} + 2.5\sigma_E$). The two different shape cuts on E_4/E are indicated by the horizontal lines.

The distribution of E_4/E is shown in Fig. 7.10 (a) as a function of E. The vast majority of the events passing the energy cuts of set 1 ($\bar{E} - 1.5\sigma_E < E < \bar{E} + 2.5\sigma_E$) is located in an ellipse having energies between 3 and 9 GeV and fractions E_4/E between 0.7 and 1 (Fig. 7.10 (b)). These are the events of good quality. If E_4/E was much smaller than 0.7, the shower was considered to be too broad. If in contrast E_4/E was much larger than 1, the energy reconstructed in the five cells of the 3×3 reconstruction volume, which were not contained in the four cells used to calculate E_4, was significantly lower than 0. The shower reconstruction was therefore also considered distorted.

The vertical spread of the ellipse was predominantly due to statistical fluctuations in the energy measured in each cell as well as local inhomogeneities of the fibers,

since the transverse shower profile is approximately constants for events with the same energy.

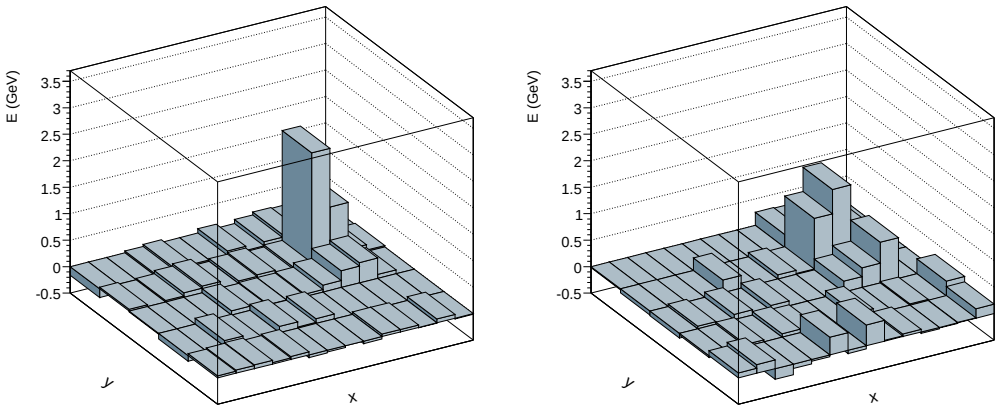

(a) (b)

Figure 7.11: Dependence of the quantity E_4/E on the shape of the transverse profile of an electromagnetic shower. The hottest cell of both events is cell 24. They have (a) $E_4/E = 0.86$, $E = 4.44$ GeV (event 497 in run 70201) and (b) $E_4/E = 0.60$, $E = 4.97$ GeV (event 877 in run 70281).

Two events with different values of E_4/E are compared in Fig. 7.11. Both events passed the tightest energy cut (set 1 of the parameters) and number 24 was the hottest cell in both cases. The energy in the event in Fig. 7.11 (a) is well confined within four cells with the maximum toward the center of row 1; E_4/E has a value of 0.86. In contrast, the energy is spread out over more cells in the event in Fig. 7.11 (b). Accordingly, E_4/E has a lower value of 0.60.

A lower and an upper limit on E_4/E were defined in order to reject the few events with a distorted shower shape. Two different sets of limits were chosen, associated to two different qualities of the events:

1. $0.7 < E_4/E < 1.0$;

2. $0.55 < E_4/E < 1.1$.

The limits are illustrated in Fig. 7.10 (b). The fraction of events with $E_4/E < 0.7$ or $E_4/E > 1.0$ was 1.3%.

Some events passing the energy and the shape cuts featured, on top of a well shaped electromagnetic shower, large energy depositions in many other cells of the 6 m tagger. Beside pile-up events, these were in particular events in which the cells at the left-hand side of the 6 m tagger measured energies larger than the average

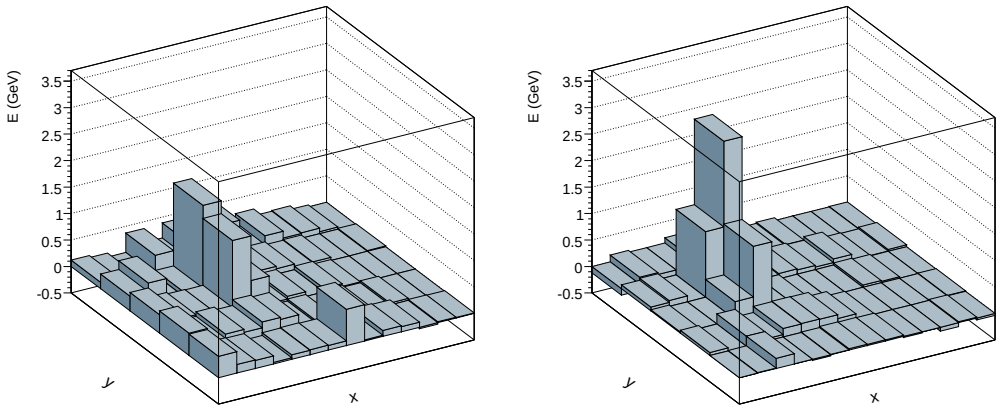

(a) (b)

Figure 7.12: Dependence of the quantity E_4/E_{70} on the isolation of an electromagnetic shower. The hottest cell of both events is number 18. They have (a) $E_4/E_{70} = 0.42$, $E_4/E = 0.82$, $E = 5.90$ GeV (event 3075 in run 70201) and (b) $E_4/E_{70} = 0.76$, $E_4/E = 0.90$, $E = 6.35$ GeV (event 88854 in run 70199).

noise level around 0 GeV. The distribution of the energy in the cells for one of such events is shown in Fig. 7.12 (a).

In order to evaluate which fraction of the total energy measured in all the cells of the 6 m tagger was reconstructed in the shower, the quantity E_4/E_{70} was investigated. E_4 was the previously introduced energy contained in the central part of the shower and E_{70} was the sum of the energies measured in all the cells. If the energy was spread out over many cells, E_4/E_{70} was expected to be small. The value of E_4/E_{70} for the event in Fig. 7.12 (a) is 0.42. Figure 7.12 (b) shows an event with a well isolated shower in comparison; here E_4/E_{70} is 0.76.

The distribution of E_4/E_{70} as a function of the energy E of the shower is shown in Fig. 7.13 (a) and (b) before and after the cuts on the energy and the shape of the shower, respectively. Most events are located in a region of energies between 3 and 9 GeV and fractions E_4/E_{70} larger than ≈ 0.5 (Fig. 7.13 (b)). Two different lower limits for E_4/E_{70} were chosen to define events of different qualities:

1. $E_4/E_{70} > 0.5$;

2. $E_4/E_{70} > 0.4$.

Showers in events having E_4/E_{70} larger than these limits were sufficiently well isolated. The limits are illustrated in Fig. 7.13 (b). The fraction of events with $E_4/E_{70} < 0.5$ was 1.2%.

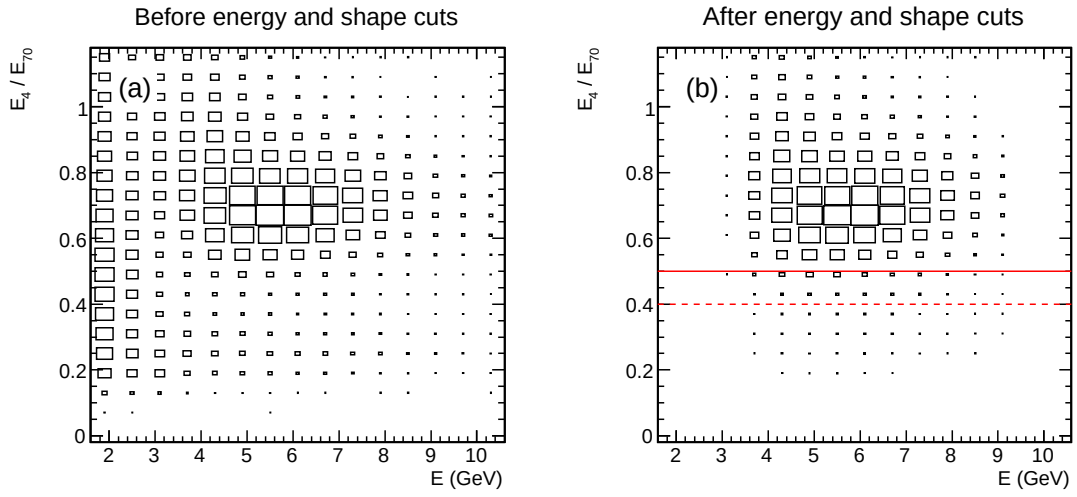

Figure 7.13: Distribution of the fraction of energy, E_4, contained in the four adjacent cells with most energy, including the hottest cell, and the total energy, E_{70}, measured in all the cells of the 6 m tagger for (a) all events with the hottest cell between column 1 and 12 and row 1 and 3, and (b) after the additional energy and shape cuts of set 1 ($\bar{E} - 1.5\sigma_E < E < \bar{E} + 2.5\sigma_E$, $0.7 < E_4/E < 1.0$). The two different isolation cuts on E_4/E_{70} are indicated by the horizontal lines.

This cut also removes pile-up events with two or more good showers in the 6 m tagger. These events were neglected at this point as their contribution was below the percentage level.

7.1.4 Summary

Events were selected by applying different sets of cuts. The cuts in the different sets were more and more stringent, thus allowing the definition of different qualities of the events. First, the noisy cells 52 and 54 were masked. Second, events with the hottest cell in a certain fiducial volume were selected: the hottest cell had not to be in the outer columns 0 and 13 or in the outer rows 0 and 4 in order to allow a complete reconstruction of the energy. For events of the highest quality, row 3 was also excluded since two cells in this row were masked. Third, an energy cut was applied, depending on the width of the energy distribution in the column containing the hottest cell, in order to select events with a real electromagnetic shower and to reject the background. Finally, cuts on the shape and the isolation of the shower were applied. All the cuts and the corresponding parameters are listed in Table 7.2. Three different quality flags were labeled ‘1’ for the highest to ‘3’ for the lowest

Quality	Cuts
1	$0 < \text{Hotx} < 13 \wedge 0 < \text{Hoty} < 3$ $\bar{E} - 1.5\sigma_E < E < \bar{E} + 2.5\sigma_E$ $0.7 < E_4/E_9 < 1.0$ $0.5 < E_4/E_{70}$
2	$0 < \text{Hotx} < 13 \wedge 0 < \text{Hoty} < 4$ $\bar{E} - 2.0\sigma_E < E < \bar{E} + 4.0\sigma_E$ $0.7 < E_4/E_9 < 1.0$ $0.5 < E_4/E_{70}$
3	$0 < \text{Hotx} < 13 \wedge 0 < \text{Hoty} < 4$ $\bar{E} - 2.5\sigma_E < E < \bar{E} + 6.0\sigma_E$ $0.55 < E_4/E_9 < 1.1$ $0.4 < E_4/E_{70}$

Table 7.2: Summary of the cuts to select events of different quality. The parameters of the functions associated with the lower and the upper limit for the energy are given in Table 7.1. The cells 52 and 54 were masked in all the cases.

quality of the reconstructed shower.

7.2 Acceptance of the photon spectrometer

The acceptance of the spectrometer was determined using the 6 m tagger. For the measurement, events were selected in which the 6 m tagger identified an electron. The electron was assumed to originate from a Bethe-Heitler process. Other processes, such as photoproduction, could be neglected owing to their much lower rate. The Bethe-Heitler cross section is of the order of 5 mb in the energy acceptance range of the 6 m tagger (see Tab. A.2 in Appendix A), whereas for example the photoproduction cross section in the same range is of the order of 300 nb [5, 34]. If an electron was detected by the 6 m tagger, it was checked whether the spectrometer also measured an event. Thus, the acceptance of the spectrometer, η_{spec}, was given by

$$\eta_{\text{spec}} = \frac{N_{\text{t6+spec}}}{N_{\text{t6}}}, \tag{7.2}$$

where N_{t6} and $N_{\text{t6+spec}}$ denote the number of events seen by the 6 m tagger and the number of events seen by both the 6 m tagger and the spectrometer, respectively. The acceptance was measured individually for each column of the 6 m tagger. The events were sorted by the column containing the hottest cell and N_{t6} and $N_{\text{t6+spec}}$ were determined independently for each column. The columns were then converted

into photon energies using the energy versus column relation in the 6 m tagger, and hence η_{spec} could be given as a function of the energy of the photon.

Events were selected by the aforementioned random trigger. Then the selection criteria described in Section 7.1 were used to decide whether the 6 m tagger detected an electron. As purity was of most importance, only events of quality '1' were selected.

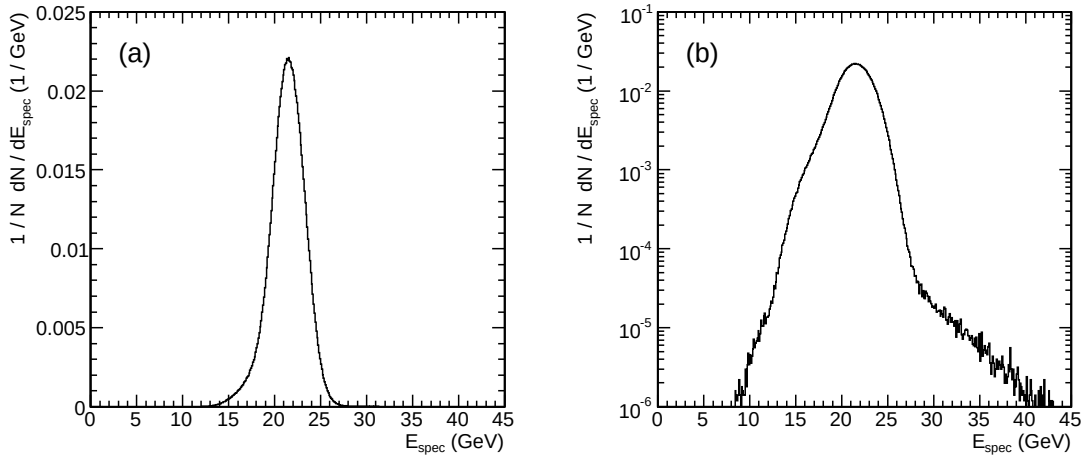

Figure 7.14: Energy spectrum of Bethe-Heitler photons measured by the spectrometer for events with an electron in the 6 m tagger. (a) Linear scale (b) logarithmic scale. The energy range exceeded the 20.5 to 23.5 GeV expected from the acceptance range of the 6 m tagger owing to effects from resolution, additional radiation, and pile-up.

In order to decide if an event was seen by the spectrometer, a simple energy cut was applied. Figure 7.14 shows the energy spectrum of photons from Bethe-Heitler events measured by the spectrometer for events with an electron in the 6 m tagger. The events were selected as described in Section 6.2.2.2 but without the cuts on the ADC counts of the photon calorimeter. Using this spectrum, an event was considered to be detected by the spectrometer if the measured energy was larger than 5 GeV. This condition was similar to that requested by the trigger of the spectrometer presented in Section 5.3. The spectrum in Fig. 7.14 exceeds the range of about 20.5 to 23.5 GeV expected from the acceptance range of the 6 m tagger. The reason was first of all the finite resolution of the spectrometer (comp. Section 7.3). The low energy part of the spectrum is due to events with initial or final state radiation of the electron at the vertex or to events in which a lepton coming from conversion of the photon in the exit window emitted a photon in a Bethe-Heitler process (comp. the discussion in Section 6.2.2.2). The high energy part is due to the presence of

pile-up events. Since these events had to be included into $N_{\mathrm{t6+spec}}$, no upper energy cut was introduced.

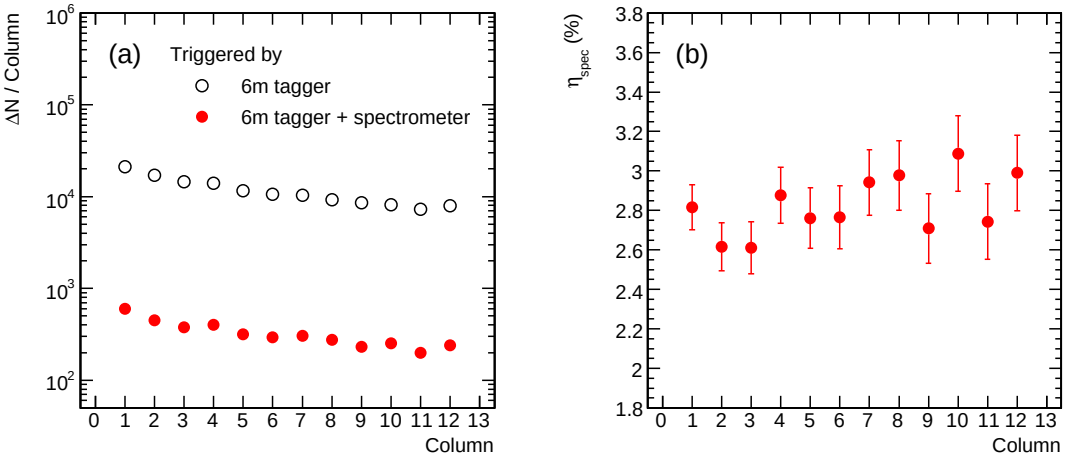

Figure 7.15: (a) The numbers N_{t6} and $N_{\mathrm{t6+spec}}$ of events accepted by the 6 m tagger and by both the 6 m tagger and the spectrometer, respectively, for each column of the 6 m tagger. (b) The resulting acceptance $\eta_{\mathrm{spec}} = N_{\mathrm{t6+spec}}/N_{\mathrm{t6}}$ of the spectrometer per column of the 6 m tagger.

The numbers N_{t6} and $N_{\mathrm{t6+spec}}$ of events accepted by the 6 m tagger and by both the 6 m tagger and the spectrometer, respectively, are shown in Fig. 7.15 (a) for each column of the 6 m tagger. The resulting acceptance η_{spec} is given per column in Fig. 7.15 (b). The errors were calculated taking into account the binomial distribution of $N_{\mathrm{t6+spec}}$ [35]. Figure 7.16 shows the same acceptance as a function of the photon energy; the columns were converted into photon energies as described in Section 7.3. The mean acceptance $\bar{\eta}_{\mathrm{spec}}$ in the range of photon energies from about 20 to 24 GeV was determined to be

$$\bar{\eta}_{\mathrm{spec}} = (2.80 \pm 0.04)\%$$

by fitting the plot in Fig. 7.16 with a horizontal line.

The measured acceptance was a product of the energy resolution of the spectrometer, the probability of the photon to convert into an e^+e^- pair in the exit window, and a factor taking into account the aperture due to mechanical obstacles between the vertex and the spectrometer as well as the magnetic field configuration in front of the spectrometer.

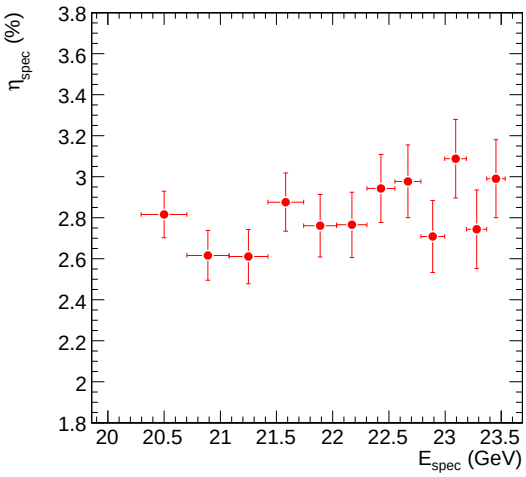

Figure 7.16: The acceptance η_{spec} of the spectrometer in bins of the photon energy, E_{spec}, corresponding to the columns of the 6 m tagger.

7.3 Energy resolution of the photon spectrometer

The 6 m tagger was also used to measure the energy resolution of the spectrometer. This was done analogue to the determination of the resolution of the 6 m tagger (Section 6.2.3).

For this study, the purity of the selection was of most importance. Therefore, Bethe-Heitler events were selected in the same way as for the horizontal correction procedure (Section 6.2.2.2). In particular, events were rejected if there was an energy deposition in the photon calorimeter in order to reduce the radiative tails at the low end of the energy spectrum of the spectrometer.

The true energy in the spectrometer was estimated by using the relation between the x position of the electron in the 6 m tagger and its energy (comp. Section 4.4). The x position of the shower maximum was approximated with the center of the column containing the hottest cell. Thus, it was determined to an accuracy equal to half of the width of the column (3 mm). As follows from Fig. 6.46, the corresponding spread in energies was of about 0.2 GeV. The events were sorted by the column in which the hottest cell was located. A distribution of the energy E_{spec} measured in the spectrometer was generated for each column. A relation $E_{\text{spec}}(n)$ between the mean energy in the spectrometer and the column n in the 6 m tagger was extracted in the previously described way by fitting the energy distribution in each column with a Gaussian and taking the mean value as the mean energy. The obtained mean energies per column are shown in Fig. 7.17; the error bar is the standard deviation of

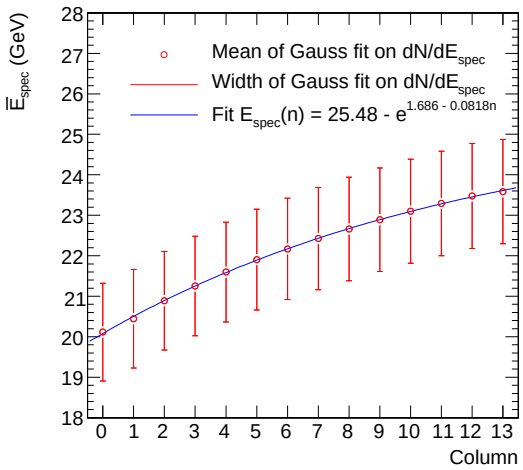

Figure 7.17: Mean energies $\bar{E}_{\text{spec}}$ of the photon from a Bethe-Heitler event measured in the spectrometer per column of the 6 m tagger hit by the corresponding electron. $\bar{E}_{\text{spec}}$ is the mean value of a Gaussian fit on the energy distribution in that column. The error bars represent the standard deviation of the Gaussian. The superimposed curve $E_{\text{spec}}(n)$ is a fitted relation between the mean energy and the column n.

the corresponding Gaussian. They were fitted with a negative exponential function with offset:

$$E_{\text{spec}}(n) = p_0 - e^{p_1 + p_2 n}. \tag{7.3}$$

The parameters obtained from the fit were

$$\begin{aligned} p_0 &= 25.43 \pm 0.02 \\ p_1 &= 1.683 \pm 0.004 \\ p_2 &= -0.0837 \pm 0.0005. \end{aligned}$$

For this fit, the actual errors on the mean values of the Gaussian fits were applied.

The energy resolution σ_{spec} of the spectrometer is given by the spread around the mean value $\bar{E}_{\text{spec}}$ of the energies measured in the spectrometer. It is shown by the error bars on the mean energies in Fig. 7.17 and in Fig. 7.18 (a). The value of σ_{spec} is of the order of 1.2 GeV.

The columns of the 6 m tagger were roughly converted into bins of photon energy according to the relation $E_{\text{spec}}(n)$ (Eq. (7.3)) and analogue to the procedure illustrated in Fig. 6.46. Thus, $\sigma_{\text{spec}}/\sqrt{\bar{E}_{\text{spec}}\,(\text{GeV})}$ could be displayed as a function of the energy E_{spec} measured in the spectrometer. This is shown in Fig. 7.18 (b). The error in each bin was obtained by Gaussian propagation of the errors on $\bar{E}_{\text{spec}}$

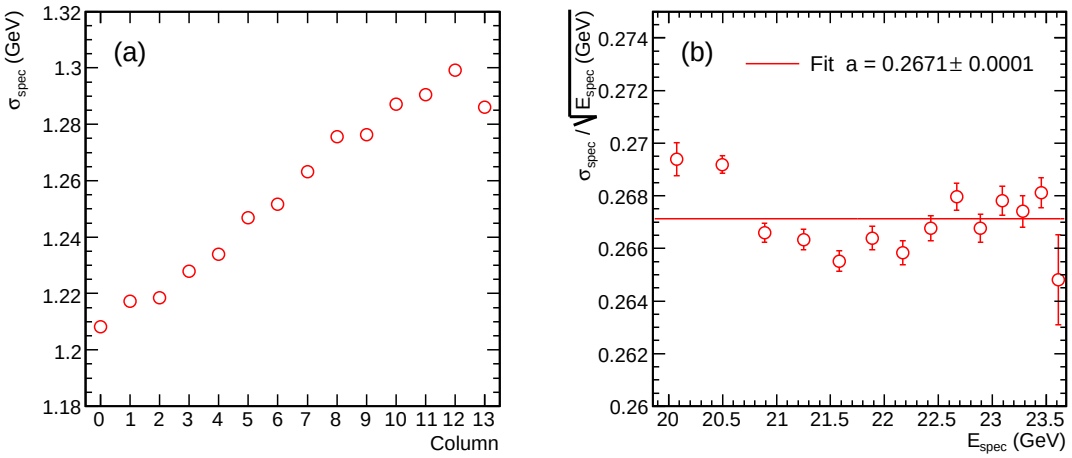

Figure 7.18: Energy resolution of the spectrometer. (a) The spread σ_{spec} of the energy around the mean value $\bar{E}_{\text{spec}}$ in one column as obtained from a Gaussian fit to the energy distribution of that column. (b) The same spread normalized to $\sqrt{\bar{E}_{\text{spec}}}$ as a function of the energy measured in the spectrometer.

and on σ_{spec} as returned by the Gaussian fit. The stochastic term a of the energy resolution (comp. Section 2.3) of the spectrometer was obtained from this plot by fitting a horizontal line:

$$a = (26.71 \pm 0.01)\%.$$

The main systematic uncertainty of the measurement comes from the energy spread of about 0.2 GeV associated with the column width.

8 Summary

In the last months of its physics program, HERA was operated at different center of mass energies in order to allow the direct measurement of the longitudinal structure function of the proton, F_L. The data taken with a small electromagnetic calorimeter is used for the evaluation of the photoproduction background in the current determination of F_L [4] as well as for determination of the total photoproduction cross section [8]. This calorimeter, the 6 m tagger, was located near the beam pipe at ≈ 6 m from the ep interaction point and could detect electrons scattered at small angles.

The calibration and the reconstruction of the electromagnetic showers in the 6 m tagger was found to be not optimal. In particular, the relative calibration of the channels and the energy reconstruction, mainly at the edges of the detector, needed to be improved.

Two different methods were studied to improve the calibration and the energy reconstruction. Both approaches used the original calibration constants as a starting point and were aimed to determine multiplicative correction factors. A sample of Bethe-Heitler events with a coincidence of an electron in the 6 m tagger and a photon in the spectrometer was used in both the cases. In these events, the energy of the electron hitting the 6 m tagger was expected to be the difference between the energy of the electron beam and the energy of the photon measured by the spectrometer.

As a first attempt, the original calibration constants were weighted with a correction factor and the reconstructed shower energy was compared to the expected energy. The correction factors were varied in order to achieve the best agreement. The optimization was done by minimizing a χ^2 function built using the residuals of the measured and the expected energies. The results of this method did not have the desired performance.

As a second attempt, the correction procedure was separated into a vertical and a horizontal correction. The vertical correction took care of a consistent relative calibration of the cells within one column using the expected transverse profile of the electromagnetic showers in the 6 m tagger. The horizontal correction optimized the energy reconstruction by comparing the reconstructed energy with the expected energy. The vertical correction introduced one correction factor per cell and the horizontal correction one factor per column, which were multiplied by the original calibration constants to obtain the final calibration constants for each cell.

The method based on the separation of the vertical and the horizontal correction significantly improved the performance of the 6 m tagger. The cells within one

column were calibrated in a consistent way relative to each other. The fiducial volume of the 6 m tagger was increased to include the columns 1 to 12 owing to a smaller energy reconstruction volume of 3×3 cells. The absolute calibration of the cells in combination with the new energy reconstruction algorithm provided a very good agreement between the reconstructed and the expected energy.

The energy acceptance range and the resolution of the newly calibrated 6 m tagger were evaluated. Furthermore, a set of cuts was developed for the selection of good electromagnetic showers in the 6 m tagger. The cuts made use of the reconstructed energy and shape of the showers. By variation of the strictness of the cuts, different qualities of the reconstructed events were defined. Applying these selection cuts, the 6 m tagger was used to measure the acceptance and the energy resolution of the photon spectrometer.

A Energy acceptance range of the 6 m tagger and rate of Bethe-Heitler events

Period	$E_{\min}$ (GeV)	$E_{\max}$ (GeV)
MER	3.99 ± 0.02	7.40 ± 0.02
LER	3.97 ± 0.01	7.24 ± 0.01
HER1s	4.40 ± 0.04	7.84 ± 0.04
HER2s	4.40 ± 0.04	7.87 ± 0.04
HER3	4.40 ± 0.06	7.80 ± 0.06

Table A.1: Limits of the energy acceptance range of the 6 m tagger for the different run periods.

k interval (GeV)	σ_{BH} (mb)	Rate (MHz)	Acceptance range
$0.1 - 27.5$	331.1	23.2	Overall
$20.3 - 23.5$	5.33	0.40	6 m tagger
$19.7 - 23.1$	5.80	0.44	

Table A.2: Integrated Bethe-Heitler cross sections and rates for different intervals of the photon energy k. An initial electron energy of 27.5 GeV, a proton energy of 920 GeV, and a luminosity of $7.5 \cdot 10^{31}\,\mathrm{cm}^{-2}s^{-1}$ were assumed [2].

B Parameters of the analysis

Cell	MER	LER	HER1s	HER2s	HER3
0	3.29751	3.24446	3.09944	3.21977	3.23101
1	3.42031	3.53479	3.46204	3.75725	3.81052
2	3.47732	3.4412	3.39707	3.35462	3.33973
3	3.27032	3.29498	3.26119	3.22984	3.21407
4	3.3686	3.31698	3.16327	3.29216	3.3585
5	3.10157	3.13531	3.14385	3.06697	3.06228
6	3.24458	3.23594	3.17595	3.08609	3.10483
7	3.28762	3.31072	3.13073	3.20845	3.21866
8	3.05687	3.05566	3.05327	2.732	2.98527
9	4.13536	3.67877	3.53789	3.47647	3.57105
10	3.24004	3.24715	3.14956	2.942	3.05287
11	3.03246	3.02031	2.98781	2.94395	2.798
12	2.76873	2.8281	2.82545	2.82106	2.79861
13	2.76146	2.80259	2.89972	2.7434	2.79794
14	2.74067	2.67733	2.73504	2.78221	2.78404
15	2.67797	2.68316	2.71964	2.8851	2.92329
16	2.91243	2.99562	2.96934	3.07876	3.09719
17	3.09514	3.14701	3.07771	3.1618	3.06539
18	3.0652	3.11145	3.05669	3.00763	3.03358
19	2.81735	2.82447	2.8357	2.87543	2.86212
20	2.88758	2.896	2.85517	2.90681	2.93588
21	2.81864	2.84304	2.88425	2.89645	2.84397
22	2.72567	2.74518	2.82841	2.73734	2.74281
23	2.7163	2.72913	2.73625	3.01739	3.02538
24	2.70639	2.73532	2.69166	2.70717	2.67785
25	2.68636	2.71225	2.7002	2.66059	2.66487
26	2.61348	2.71861	2.61909	2.7958	2.67551
27	2.63934	2.76501	2.74601	2.7323	2.728
28	2.82927	2.83057	2.77105	2.91206	2.92987
29	3.02934	3.0378	3.07231	3.25651	3.26809
30	2.97935	3.0195	3.02144	3.40266	3.38163
31	3.06424	3.11918	3.05331	3.11465	3.13403
32	3.00336	3.07263	3.03933	3.05498	3.01585
33	2.89217	2.99148	2.93722	2.97281	2.94517

Cell	MER	LER	HER1s	HER2s	HER3
34	3.07786	3.04718	3.19098	3.08318	3.11753
35	2.8896	2.92714	2.94501	3.0969	3.13728
36	2.95682	3.00851	3.02485	2.8798	2.87522
37	3.01216	3.06007	3.07517	2.97692	2.97967
38	3.09722	3.05887	2.90069	2.9632	2.94162
39	2.80488	2.8042	2.79813	2.78161	2.86891
40	2.77773	2.78673	2.73149	2.71321	2.72037
41	2.75301	2.77987	2.77877	2.73421	2.72587
42	2.85441	2.84971	3.02311	3.21593	3.20194
43	3.25318	3.25789	3.23633	3.39582	3.34063
44	3.16578	3.18795	3.22936	3.20922	3.32717
45	3.4435	3.27431	3.37382	3.26921	3.2539
46	3.17394	3.20722	3.22072	3.15971	3.11363
47	2.90415	2.96735	2.98223	2.92997	2.96082
48	3.00928	3.02853	3.10225	2.883	2.87288
49	3.38057	3.6045	3.3768	3.27699	3.24278
50	2.89344	2.94049	2.91453	2.86269	2.87822
51	3.0032	2.84903	2.81054	2.85697	2.80982
52	2.9826	2.93865	3.00246	2.89275	2.8946
53	2.85795	2.81257	2.79838	2.7856	2.78409
54	3.20531	3.22567	2.98468	2.93198	2.87411
55	2.72062	2.66926	2.71277	2.71934	2.79259
56	2.86089	2.85283	2.9268	3.05362	3.00064
57	2.7865	2.81097	2.88313	2.8923	2.88124
58	2.79577	2.84613	2.96758	2.90462	3.01926
59	2.95297	2.99055	3.04322	3.00631	3.02751
60	3.00823	2.98891	3.11694	3.07435	3.00729
61	2.79063	2.79333	2.94605	2.82975	2.82561
62	2.81108	2.88748	2.89338	2.85005	2.8456
63	3.17221	3.17607	3.22737	3.21048	3.23811
64	2.92664	2.94784	2.96114	2.89403	2.85029
65	2.85381	2.86688	2.89253	2.84389	2.80983
66	2.63774	2.66967	2.70706	2.73515	2.66746
67	2.6541	2.67137	2.69469	2.72099	2.70125
68	2.63505	2.69317	2.68396	2.67218	2.65896
69	2.6346	2.63246	2.61048	2.62183	2.57529

Table B.1: Width $\sigma_{\mathcal{P}}$ of the pedestal peak in ADC counts per cell and run period.

MER			
Iteration	$f_{01} = \bar{E}_0/\bar{E}_1$	$f_{21} = \bar{E}_2/\bar{E}_1$	$f_{31} = \bar{E}_3/\bar{E}_1$
0	$0.0681 + 0.00389n$	$0.5858 - 0.03637n$	$0.0802 - 0.00527n$
1	$0.0679 + 0.00391n$	$0.5921 - 0.03656n$	$0.08097 - 0.00531n$
2	$0.0678 + 0.00392n$	$0.5908 - 0.03635n$	$0.08087 - 0.00529n$
LER			
Iteration	$f_{01} = \bar{E}_0/\bar{E}_1$	$f_{21} = \bar{E}_2/\bar{E}_1$	$f_{31} = \bar{E}_3/\bar{E}_1$
0	$0.06716 + 0.00388n$	$0.5665 - 0.03484n$	$0.07839 - 0.00509n$
1	$0.06694 + 0.00390n$	$0.5727 - 0.03505n$	$0.07896 - 0.005110n$
2	$0.06688 + 0.00391n$	$0.5716 - 0.03488n$	$0.07885 - 0.005093n$
HER1s			
Iteration	$f_{01} = \bar{E}_0/\bar{E}_1$	$f_{21} = \bar{E}_2/\bar{E}_1$	$f_{31} = \bar{E}_3/\bar{E}_1$
0	$0.0826 + 0.00055n$	$0.7726 - 0.0401n$	$0.0959 - 0.00570n$
1	$0.0824 + 0.00062n$	$0.7797 - 0.0392n$	$0.0967 - 0.00568n$
2	$0.0822 + 0.00067n$	$0.7789 - 0.0385n$	$0.0967 - 0.00564n$
3	$0.0821 + 0.00069n$	$0.7764 - 0.0380n$	$0.0965 - 0.00560n$
HER2s			
Iteration	$f_{01} = \bar{E}_0/\bar{E}_1$	$f_{21} = \bar{E}_2/\bar{E}_1$	$f_{31} = \bar{E}_3/\bar{E}_1$
0	$0.0795 + 0.00083n$	$0.7561 - 0.03751n$	$0.0964 - 0.00601n$
1	$0.0792 + 0.00093n$	$0.7594 - 0.03605n$	$0.0970 - 0.00600n$
2	$0.0789 + 0.00098n$	$0.7584 - 0.0353n$	$0.0971 - 0.00597n$
3	$0.0788 + 0.00101n$	$0.7562 - 0.0348n$	$0.0970 - 0.00594n$
HER3			
Iteration	$f_{01} = \bar{E}_0/\bar{E}_1$	$f_{21} = \bar{E}_2/\bar{E}_1$	$f_{31} = \bar{E}_3/\bar{E}_1$
0	$0.0746 + 0.00143n$	$0.7296 - 0.03950n$	$0.0909 - 0.00579n$
1	$0.0744 + 0.00151n$	$0.7331 - 0.0384n$	$0.0915 - 0.00579n$
2	$0.0741 + 0.00156n$	$0.7306 - 0.0376n$	$0.0915 - 0.00575n$
3	$0.0740 + 0.00158n$	$0.7285 - 0.0372n$	$0.0913 - 0.00572n$

Table B.2: Linear parameterizations $f(n)$ of the dependencies of the ratios f of mean energy in different rows on the column index n. The mean energies were calculated using the calibration constants of the previous iteration. The coefficients are given to the accuracy of the error on the fits.

MER			
Iteration	p_0	p_1	p_2
0	2.16	1.701	−0.0876
1	2.07	1.713	−0.0850
2	2.07	1.713	−0.0850
LER			
Iteration	p_0	p_1	p_2
0	2.16	1.670	−0.0862
1	2.08	1.682	−0.0838
2	2.08	1.682	−0.0838
HER1s			
Iteration	p_0	p_1	p_2
0	2.64	1.705	−0.090
1	2.54	1.716	−0.087
2	2.54	1.716	−0.087
3	2.50	1.722	−0.086
HER2s			
Iteration	p_0	p_1	p_2
0	2.69	1.704	−0.093
1	2.60	1.712	−0.090
2	2.60	1.713	−0.090
3	2.60	1.713	−0.090
HER3			
Iteration	p_0	p_1	p_2
0	2.52	1.72	−0.087
1	2.43	1.73	−0.084
2	2.43	1.73	−0.084
3	2.43	1.73	−0.084

Table B.3: Parameters of the exponential parameterization $E_{\text{exp}}(n) = p_0 + e^{p_1+p_2 n}$ of the dependence of the expected energy in the 6 m tagger on the column n for the different run periods and iterations. The parameters are given to the accuracy of the error on the fits.

MER		
Iteration	$\bar{\varphi}_{\text{left}}$	$\bar{\varphi}_{\text{right}}$
0	0.1565	0.2567
1	0.1610	0.2590
2	0.1610	0.2587
LER		
Iteration	$\bar{\varphi}_{\text{left}}$	$\bar{\varphi}_{\text{right}}$
0	0.1558	0.2577
1	0.1602	0.2599
2	0.1602	0.2596
HER1s		
Iteration	$\bar{\varphi}_{\text{left}}$	$\bar{\varphi}_{\text{right}}$
0	0.1611	0.2572
1	0.1643	0.2583
2	0.1644	0.2584
3	0.1643	0.2583
HER2s		
Iteration	$\bar{\varphi}_{\text{left}}$	$\bar{\varphi}_{\text{right}}$
0	0.1601	0.2529
1	0.1628	0.2544
2	0.1629	0.2546
3	0.1629	0.2546
HER3		
Iteration	$\bar{\varphi}_{\text{left}}$	$\bar{\varphi}_{\text{right}}$
0	0.1565	0.2529
1	0.1594	0.2542
2	0.1595	0.2543
3	0.1595	0.2543

Table B.4: Mean values $\bar{\varphi}_{\text{left}}$ and $\bar{\varphi}_{\text{right}}$ of the fraction of the energy deposited in the left and in the right column of the reconstruction volume, respectively, over the energy in the other columns for the different run periods and iterations. The parameters are given to the accuracy of the error on the fits.

MER	LER	HER1s	HER2s	HER3
27.5215	27.505	27.610	27.6475	27.6475

Table B.5: Initial electron beam energies E_i in GeV in the different run periods. The values represent mean values of the energies per run, which were taken from the HERA database. The variation of the energy between the runs within one period were smaller than 2 MeV i.e. $7 \cdot 10^{-5}$, except for a few runs after changing the beam polarization and after the start of the LER period.

C Final correction factors

Cell	MER	LER	HER1s	HER2s	HER3
0	1.9597	1.98199	2.16116	2.16511	2.13833
1	0.791437	0.78257	0.820579	0.842872	0.822523
2	0.631976	0.635786	0.67419	0.681077	0.688701
3	1.34105	1.36416	1.37757	1.39225	1.39894
4	1.25841	1.27938	1.14269	1.15866	1.1786
5	0.773029	0.780094	0.814909	0.839351	0.860928
6	1.38844	1.38548	1.45213	1.47162	1.46466
7	1.19228	1.16047	1.14996	1.18565	1.19805
8	1.03033	1.03637	1.04645	1.06171	1.06236
9	1.29488	1.28306	1.29753	1.24871	1.26924
10	0.779267	0.783208	0.834423	0.820858	0.820642
11	0.927441	0.928408	1.10086	1.10139	1.09009
12	0.847125	0.840457	0.962008	0.951304	0.927589
13	0.664165	0.647323	0.908664	0.936384	0.934246
14	1.9597	1.98199	2.16116	2.16511	2.13833
15	1.79349	1.78028	1.58384	1.58197	1.58169
16	1.10795	1.1172	1.08523	1.07254	1.07892
17	1.0365	1.04877	1.04304	1.04534	1.05138
18	1.11252	1.12797	1.08176	1.0837	1.10411
19	1.32409	1.33863	1.34733	1.33996	1.35445
20	1.36188	1.37437	1.56342	1.55453	1.51666
21	1.11839	1.13086	1.19979	1.1944	1.18259
22	1.08908	1.10033	1.16444	1.16721	1.15444
23	0.983506	0.988217	1.00759	1.02141	1.03173
24	1.09067	1.10028	1.13906	1.11789	1.1178
25	0.994176	0.998819	1.01776	0.996486	1.01273
26	1.30435	1.31302	1.16864	1.14178	1.18173
27	0.664165	0.647323	0.908664	0.936384	0.934246
28	1.9597	1.98199	2.16116	2.16511	2.13833
29	1.70763	1.68769	1.69384	1.61186	1.59791
30	1.14952	1.15605	1.21345	1.21982	1.22946
31	1.20179	1.21563	1.16392	1.13919	1.14211
32	1.31422	1.33356	1.30689	1.27298	1.28499
33	0.897485	0.908005	0.94954	0.933696	0.932946

Cell	MER	LER	HER1s	HER2s	HER3
34	0.731247	0.731229	0.794559	0.789232	0.780369
35	0.978125	0.977182	0.999411	0.99769	1.01696
36	0.945854	0.946366	0.974362	0.971688	0.983431
37	1.37498	1.3891	1.42675	1.36993	1.39393
38	1.01383	1.00436	1.01911	1.04854	1.05879
39	1.08332	1.09631	1.22734	1.29313	1.28205
40	1.07722	1.08527	1.18554	1.26281	1.23636
41	0.664165	0.647323	0.908664	0.936384	0.934246
42	1.9597	1.98199	2.16116	2.16511	2.13833
43	1.66493	1.66544	1.56303	1.62674	1.6248
44	0.850481	0.856747	0.85952	0.884071	0.892552
45	1.08297	1.07315	1.06167	1.06648	1.07036
46	1.46335	1.49319	1.40373	1.39977	1.42765
47	0.932026	0.953007	1.00886	1.0385	1.04968
48	1.05974	1.07643	1.19608	1.17754	1.15833
49	1.21276	1.24608	1.22153	1.21282	1.20621
50	1.02524	1.02184	1.06506	1.03506	1.03042
51	1.05124	1.02068	1.03318	0.972041	0.976009
52	2.32805	2.34309	2.69319	2.778	2.79993
53	0.584604	0.590591	0.66022	0.605713	0.605209
54	2.63057	2.61632	3.29543	3.06246	2.91284
55	0.664165	0.647323	0.908664	0.936384	0.934246
56	1.9597	1.98199	2.16116	2.16511	2.13833
57	1.67027	1.65643	1.5596	1.53792	1.53141
58	1.06975	1.07755	1.08681	1.08459	1.09216
59	1.09571	1.10677	1.09818	1.09123	1.09494
60	1.18193	1.19765	1.16883	1.15985	1.17509
61	1.12722	1.14232	1.14488	1.13958	1.15394
62	1.13273	1.14208	1.22102	1.21426	1.20259
63	1.08984	1.09729	1.13065	1.12818	1.1318
64	1.05029	1.0587	1.09421	1.09442	1.09445
65	1.06103	1.06395	1.11554	1.11267	1.11875
66	1.05564	1.06158	1.09992	1.09243	1.09482
67	0.988059	0.993246	1.05282	1.04872	1.05268
68	1.22237	1.22898	1.17196	1.1663	1.1821
69	0.664165	0.647323	0.908664	0.936384	0.934246

Table C.1: Final correction factors per cell and run period.

Bibliography

[1] U. Schneekloth, *The HERA Luminosity Upgrade*, DESY-HERA-98-05 (1998).

[2] M. Seidel, *The Upgraded Interaction Regions of HERA*, DESY-HERA-00-01 (2000).

[3] S. Bentvelsen, J. Engelen and P. Kooijman, *Proc. Workshop on Physics at HERA, Oct. 1991*, Volume 1, W. Buchmüller and G. Ingelman (eds.), DESY (1991).

[4] D. Kollár, *Measurement of the longitudinal structure function F_L at ZEUS*, XVI International Workshop on Deep-Inelastic Scattering and Related Subjects, London, UK (2008).

[5] ZEUS Collaboration, Chekanov, S. et al., *Measurement of the photon proton total cross section at a center-of-mass energy of 209-GeV at HERA*, Nucl. Phys. B627,3 (2002).

[6] ZEUS Collaboration, *The Upgraded Luminosity System for the ZEUS Experiment*, PRC-99-09 (1999).

[7] A. Levy, *Measurement of the energy dependence of the total photoproduction cross section at HERA*, XVI International Workshop on Deep-Inelastic Scattering and Related Subjects, London, UK (2008).

[8] W. Schmidke, σ_{tot} *progress report*, talk given at the ZEUS Collaboration Meeting, Feb. 13 (2008).

[9] W.-M. Yao et al. (Particle Data Group), J. Phys. G 33, 1 (2006) and 2007 partial update for the 2008 edition.

[10] W. Fabjan and F. Gianotti, *Calorimetry for particle physics*, Reviews of Modern Physics, Volume 75 (2003).

[11] ZEUS Collaboration, U. Holm (ed.), *The ZEUS Detector*, Status Report (unpublished), DESY (1993).
Available at: `http://www-zeus.desy.de/bluebook/bluebook.html`.

[12] J.D. Jackson, *Classical Electrodynamics*, John Wiley and Sons, Inc., 2nd edition (1975).

[13] W. Heitler, *The Quantum Theory of Radiation*, Oxford University Press, 3rd edition (1957).

[14] ZEUS Luminosity Monitor Group, *First Measurement of HERA Luminosity by ZEUS Lumi Monitor*, DESY 92-066 (1992).

[15] M. Helbich et al., *The Spectrometer System for Measuring ZEUS Luminosity at HERA*, ZEUS Note (unpublished) ZEUS-06-002 (2006).

[16] T. Gosau, *Measurement of Multijet Events at Low x_{BJ} and Low Q^2 with the ZEUS Detector at HERA*, Dissertation, DESY-THESIS-2007-028 (2007).

[17] T. Theedt, T. Gosau, and T. Schörner-Sadenius, *The 6 m tagger*, talk given at the F_L Review Meeting, Aug. 25 (2006).

[18] N. Krumnack, *Testbeam Experiments and Monte Carlo Simulation of the ZEUS 6 m tagger*, Diploma Thesis, Universität Hamburg (2001).

[19] Personal web page of T. Theedt:
`http://www-zeus.desy.de/~theedt/otherpages/Research/6m_Tagger.html`

[20] U. Schneekloth, private communication.

[21] T. Theedt, private communication.

[22] W. Schmidke, private communication.

[23] M. Turcato, *6 m tagger in MOZART: status report*, talk given at the F_L Monthly Meeting, Jan. 22 (2008).

[24] ZEUS CDAQ Group, S. Bhadra et al., *The ZEUS Third Level Trigger System*, Zeus-Note (unpublished) ZEUS-89-051 (1989).

[25] J. Grebenyuk, private communication.

[26] J. Grebenyuk, M. Turcato, *6m tagger update*, talk given at the F_L Monthly Meeting, November 11, (2007).

[27] M. Turcato, *6 m tagger: take routine and calibration*, talk given at the F_L Weekly Meeting, Oct 26 (2007).

[28] ZEUS integrated luminosity:
`http://www-zeus.desy.de/physics/lumi/lumi07p/lumi_0607.html`.

[29] T. Gosau, private communication.

[30] V. Blobel, E. Lohrmann, *Statistische und numerische Methoden der Datenanalyse*, Teubner (1998).

[31] `TFitterMinuit` class for minimization:
`http://root.cern.ch/root/html/TFitterMinuit.html`.

[32] Minuit2 package: `http://project-mathlibs.web.cern.ch`
`/project-mathlibs/sw/Minuit2/html/index.html`.

[33] W. Schmidke, σ_{tot} *progress report*, talk at the F_L Weekly Meeting, Feb. 21 (2008).

[34] W. Schmidke, σ_{tot} *progress report*, talk at the F_L Monthly Meeting, Mar. 27 (2008).

[35] G. D'Agostini, *Bayesian reasoning in high-energy physics : principles and applications*, CERN 99-03, July (1999).

Danke

Abschließend möchte ich mich bei all denjenigen bedanken, die zu dieser Arbeit auf direkte oder indirekte Weise beigetragen haben.

Zuerst möchte ich mich bei Prof. Dr. Robert Klanner und Prof. Dr. Peter Schleper für die Aufnahme in ihre Arbeitsgruppe sowie die Möglichkeit bedanken, in einer sehr angenehmen Arbeitsatmosphäre diese Diplomarbeit anfertigen zu können. Ich möchte außerdem Prof. Dr. Robert Klanner, der bei Problemen stets die richtige Lösung parat hatte, für die intensive Betreuung meiner Arbeit danken. Ich habe sehr viel gelernt.

Des Weiteren gilt mein Dank Prof. Dr. Caren Hagner für das Erstellen des Zweitgutachtens.

Very special thanks go to Dr. Monica Turcato for her great supervision of my work. You always had new ideas and solutions and were never tired to correct the various drafts of this thesis. I have learned a lot from you during this year and it was a pleasure working together with you — Grazie, Monica!

I would also like to thank Dr. William Schmidke for his continuous help regarding the LUMI system.

Darüber hinaus möchte ich mich bei allen Mitgliedern der Arbeitsgruppe für die Hilfsbereitschaft und die tolle Stimmung bedanken, aufgrund derer ich mich am Institut immer wohl gefühlt habe. Insbesondere danke ich Thorben Theedt für die Beantwortung meiner Fragen zum 6 *m tagger, Hanno Perrey und Jörg Behr für ihre Hilfe beim Programmieren, Christian Blohm für unsere interessanten Gespräche und Holger Enderle für das gemeinsame Ertragen der Diplomandenzeit sowie Antje Hüttmann und Friederike Januschek für die tolle Stimmung in unserem Büro.*

Ich möchte auch meinen Freunden danken, mit denen ich während meines ganzen Studiums viel erlebt habe. Insbesondere danke ich Barbara, Fran, Gunther, Pierre und Stefan für ein unvergessliches Jahr in Uppsala, Wiebke, die mir die Augen geöffnet hat und stets über meine Vergesslichkeit hinweg sieht, Julika und Jörn für die unzähligen gemeinsam verbrachten Stunden und leckeren Abendessen, Bente und meiner Schwester Bettina, die sich während der ganzen Zeit um mich gekümmert haben, sowie meinem besten Freund Stefan, der immer an meiner Seite gestanden hat.

Vor allen aber danke ich meinen Eltern, Marion und Horst, sowie meinen Großeltern, Anneliese, Herbert, Inge und Rolf für ihre Großzügigkeit und bedingungslose Unterstützung.

Erklärung

Hiermit versichere ich, Matthias Schröder, die vorliegende Arbeit selbstständig verfasst und nur die angegebenen Quellen als Hilfsmittel verwendet zu haben. Des Weiteren erkläre ich mich mit der Veröffentlichung dieser Arbeit einverstanden.

Hamburg, den 27.04.2008

Matthias Schröder